



POLYTECHNIC UNIVERSITY OF TURIN
TECHNICAL UNIVERSITY OF MUNICH

Master in Aerospace Engineering

**Performance and Emission Imaging of a Coaxial Single
Element GO₂/GCH₄ Rocket Combustion Chamber**

Supervisor

Prof. Dario Giuseppe Pastrone

Co-Supervisor

M.Sc. Fernanda Maia

Author

Pasquale Difficile

Academic Year 2017/2018

Declaration of Authorship

Name: **Difficile Pasquale**

I hereby declare that this thesis is my own work prepared without the help of a third party. No other than the listed literature and resources have been used. All sources transferred literally or analogously to this work have been labeled accordingly.

Additionally, I hereby certify that this thesis has not been underlain in any other examination procedure up to the present.

.....

Date, Sign

To my father, my mother and my sister.

Acknowledgments

Prima di tutto, vorrei ringraziare il professore Dario Giuseppe Pastrone per avermi dato l'opportunità di trascorrere sei mesi in una delle più prestigiose università in ambito aerospaziale in Europa, come l'Università Tecnica di Monaco.

Ringrazio la mia supervisor, Fernanda Maia Winter, che ha contribuito alla realizzazione di questa esperienza accettandomi come collega per parte del suo percorso verso la sua tesi di dottorato. In questi sei mesi ha condiviso con me le sue conoscenze che hanno certamente riempito il mio bagaglio culturale dandomi la possibilità di aspirare a qualcosa di migliore per il mio futuro.

Voglio ringraziare i miei compagni di avventura Antonio e Alessandro. Vivere insieme ha reso questa esperienza meno difficile, sia professionalmente che umanamente. Ringrazio loro per l'aiuto e tutte le parole di conforto perché Monaco, senza di loro, sarebbe stata sicuramente più fredda. Auguro loro tanta fortuna quanto i litri di birra bevuti insieme.

Un ringraziamento speciale va ai miei amici Giuseppe, Riccardo, Francesco, Vincenzo, Iole e Rosy, al mio amico di infanzia Pasquale e al mio barbiere di fiducia Pasquale. Ognuno, con un messaggio o una chiamata, si è mostrato vicino nonostante la distanza mitigando tutte le difficoltà incontrate in questo percorso.

Ringrazio, inoltre, tutta la mia famiglia e gli amici di famiglia, perché ognuno a modo suo mi ha trasmesso la forza e la determinazione di credere in ciò che stavo facendo senza mollare mai la presa. Sento il dovere di citare due persone in particolare: mia zia Nicoletta, che con le sue forniture di cibo mi ha sempre fatto sentire a casa in qualsiasi posto, e mio zio Gianni, che con la sua arte dello sdrammatizzare mi ha sempre fatto vedere il bicchiere mezzo pieno.

Ringrazio di cuore mia sorella per il suo quotidiano supporto morale e i mille consigli, le voglio un mondo di bene e spero che la nostra complicitá sia sempre un punto di forza per entrambi.

Ad ogni modo, il mio ringraziamento piú grande va ai miei genitori. Li ringrazio per il continuo supporto economico e mi scuso se qualche volta il mio egoismo li ha portati in situazioni economiche difficili, davvero spero un giorno di ripagare ogni sacrificio fatto per me. Tutte le parole di questo mondo, comunque, non sarebbero abbastanza per descrivere il mio senso di gratitudine nei loro riguardi, al momento riesco soltanto a dire che sono cosí fiero di essere loro figlio che rinascerei mille altre volte da loro.

Abstract

The present work aims to study a rectangular single-element combustion chamber performances by using methane and oxygen as propellants. Sensors were applied to the combustion chamber to measure temperature, pressure, parameters necessary to calculate performance indices of rocket through a MATLAB code. Furthermore, an optical window is present to allow an ICCD Camera to take pictures of the flame to investigate the flame emissions: this is a non-intrusive optical diagnostic technique which takes the name of *Chemiluminescence Imaging*. The camera sensor used is covered by an optical filter which makes radicals OH^* visible. From the data collected by camera, it is possible to deduce how OH^* concentration affects changes in brightness and hence how the mixing evolves in different cases. In particular, eight cases have been performed: four tests with 10 *bar* pressure in the combustion chamber, letting the mixture ratio to vary from 2.2 to 3.4, with 0.4 steps, and other four tests with the same ROFs but with 20 *bar* pressure. Every picture captured is processed to improve its quality by eliminating errors and noise due to acquisition, in order to facilitate the extraction of experimental data. Finally, results obtained from the performance study and emission imaging will be compared and discussed.

Contents

1	Introduction	1
1.1	Propellant combination Methane/Oxygen	1
1.2	Optical system for combustion diagnostic	3
1.3	Chemiluminescence	7
1.3.1	Flame Spectrum	8
2	Experimental Setup and Hardware description	11
2.1	Hardware Description	11
2.1.1	Temperature and Pressure Measurement	16
2.2	Experimental Setup	17
2.2.1	Optical Setup	17
2.2.1.1	ICCD Camera	18
2.3	Operating Conditions and Sequence	21
2.3.1	Load Points	22
3	Digital Image Processing	24
3.1	Overview	24
3.2	Image Pre-processing	25
3.2.1	Shading Correction	25
3.2.2	Angle Correction	26
3.3	Image Post-processing	28
3.3.1	Average Image	28
3.3.2	Image Framing	33
3.4	Workflow of MATLAB code	36
4	Test Results	39
4.1	Rocket Performance Results	39
4.1.1	Assumptions	39
4.1.1.1	Assumptions on the fluid	39

4.1.1.2	Assumptions concerning transformation	40
4.1.2	Performance Indices Overview	41
4.1.2.1	The thrust coefficient	41
4.1.2.2	The characteristic velocity	42
4.1.2.3	The effective exhaust velocity	42
4.1.2.4	Total and specific impulse	43
4.1.2.5	The volumetric specific impulse	43
4.1.3	Combustion Chamber Processes Overview	45
4.1.4	Results	47
4.2	Image Processing Results	54
5	Conclusions	63
6	Appendix	66
6.1	Appendix A	66
6.1.1	Performance Matlab code	66
6.1.2	Emission Imaging Matlab code	78
6.2	Appendix B	83
6.2.1	Data Tables	83

List of Figures

1.1	Typical chemiluminescence spectrum of an atmospheric methane-air flame.	8
2.1	Combustion chamber section	12
2.2	Combustion chamber configuration	13
2.3	Injector geometry	13
2.4	Combustion Chamber and Optical Window	14
2.5	Transmission Spectrum of the Quartz[15]	15
2.6	Soot	15
2.7	Optical setup	17
2.8	Cross section through the optical part of an Intensified CCD camera (with frame transfer CCD)	19
2.9	FlameStar II System	19
2.10	Main Control System (LabView)	21
2.11	Test and Nominal Load Points	22
3.1	Flame without Shading Correction, Methane, 20 bar, ROF 3.4	25
3.2	Flame with Shading Correction, Methane, 20 bar, ROF 3.4	25
3.3	Case <i>hydrogen/oxygen</i> , 10 bar, ROF 4.4, no angle correction	27
3.4	Case <i>hydrogen/oxygen</i> , 10 bar, ROF 4.4, angle correction (1.5°)	27
3.5	Example of a Three-dimensional Matrix	28
3.6	Case <i>methane/oxygen</i> , 20 bar, ROF 2.2, First Instantaneous Image	30
3.7	Case <i>methane/oxygen</i> , 20 bar, ROF 2.2, Second Instantaneous Image	30
3.8	Case <i>methane/oxygen</i> , 20 bar, ROF 2.2, Third Instantaneous Image	31
3.9	Case <i>methane/oxygen</i> , 20 bar, ROF 2.2, Fourth Instantaneous Image	31
3.10	Case <i>methane/oxygen</i> , 20 bar, ROF 2.2, Fifth Instantaneous Image	32
3.11	Case <i>methane/oxygen</i> , 20 bar, ROF 2.2, Average Image	32
3.12	Image Captured by ICCD Camera	33
3.13	Image Framed	33
3.14	Case <i>methane/oxygen</i> , 20 bar, ROF 2.2, Average of the Entire Image	34

3.15	Case <i>methane/oxygen</i> , 20 bar, <i>ROF</i> 2.2, Image Framed	34
3.16	Emission Intensities	36
3.17	Emission Intensities Normalized	36
4.1	Combustion Chamber Temperature for Oxygen/Methane	40
4.2	Theoretical Characteristic Velocity	47
4.3	Experimental Characteristic Velocity	47
4.4	Experimental Exhaust Velocity c	48
4.5	Experimental Specific Impulse I_{sp}	48
4.6	Experimental Volumetric Specific Impulse I_ρ	49
4.7	Volumetric Specific Impulse I_ρ and Exhaust Velocity c for Hydrogen/Oxygen	49
4.8	Volumetric Specific Impulse I_ρ and Exhaust Velocity c for Methane/Oxygen	50
4.9	Combustion efficiency η_c	51
4.10	Velocity ratio VR	52
4.11	Momentum flux ratio J	53
4.12	Maximum pixel intensity value captured by ICCD camera	54
4.13	Case 10 bar, <i>ROF</i> 2.2	55
4.14	Case 10 bar, <i>ROF</i> 2.6	55
4.15	Case 10 bar, <i>ROF</i> 3.0	55
4.16	Case 10 bar, <i>ROF</i> 3.4	55
4.17	Case 20 bar, <i>ROF</i> 2.2	56
4.18	Case 20 bar, <i>ROF</i> 2.6	56
4.19	Case 20 bar, <i>ROF</i> 3.0	56
4.20	Case 20 bar, <i>ROF</i> 3.4	56
4.21	Mean Emission Intensity along axial direction as a function of P_{CC} for <i>ROF</i> 2.2	57
4.22	Mean Emission Intensity along axial direction as a function of P_{CC} for <i>ROF</i> 2.6	57
4.23	Mean Emission Intensity along axial direction as a function of P_{CC} for <i>ROF</i> 3.0	58
4.24	Mean Emission Intensity along axial direction as a function of P_{CC} for <i>ROF</i> 3.4	58
4.25	Mean Emission Intensity along axial direction as a function for <i>ROF</i> 2.2, 2.6, 3.0 and 3.4 at 10 bar	59
4.26	Mean Emission Intensity along axial direction as a function for <i>ROF</i> 2.2, 2.6, 3.0 and 3.4 at 20 bar	59
4.27	Radial Profile of Flame at 20 bar [23]	60

List of Tables

1.1	Measuring techniques for combustion and flame characterization[3]	4
2.1	Combustion chamber geometry	11
2.2	Injector geometry	13
6.1	Hardware Input Data	83
6.2	Thermodynamic and Chemical Input Data	83
6.3	$P_C = 9.707 \text{ bar}$. $ROF = 2.257$	84
6.4	$P_C = 9.184 \text{ bar}$. $ROF = 2.605$	85
6.5	$P_C = 9.337 \text{ bar}$. $ROF = 3.040$	86
6.6	$P_C = 9.434 \text{ bar}$. $ROF = 3.549$	87
6.7	$P_C = 18.759 \text{ bar}$. $ROF = 2.158$	88
6.8	$P_C = 18.624 \text{ bar}$. $ROF = 2.545$	89
6.9	$P_C = 18.333 \text{ bar}$. $ROF = 3.036$	90
6.10	$P_C = 19.147 \text{ bar}$. $ROF = 3.341$	91

Nomenclature

List of Symbols and Variables

P	[bar]	Pressure
γ	[-]	Specific Heat Ratio
T	[K]	Temperature
A	[m^2]	Cross Section Area
\dot{m}	[$\frac{kg}{s}$]	Mass Flow Rate
u	[$\frac{m}{s}$]	Axial Velocity
F	[N]	Thrust
F_0	[N]	Thrust in Vacuum. No Nozzle Contribution
C_F	[-]	Thrust Coefficient
h^o	[J]	Total Enthalpy
M	[$\frac{kg}{mol}$]	Molar Mass
R	[$\frac{J}{Kmol}$]	Gas Constant
c^*	[$\frac{m}{s}$]	Characteristic Velocity
c	[$\frac{m}{s}$]	Effective Exhaust Velocity
I_{sp}	[s]	Specific Impulse
I_ρ	[$\frac{kg \cdot s}{m^3}$]	Volumetric Specific Impulse
g_0	[$\frac{m}{s^2}$]	Gravity Acceleration
ρ	[$\frac{kg}{m^3}$]	Density
J	[-]	Momentum Flux Ratio
VR	[-]	Velocity Ratio

List of Indices

c	Combustion Chamber
t	Nozzle Throat
0	Ambient
e	Nozzle Outlet

Abbreviations

ROF	Oxygen to Fuel Ratio
O/F	Oxygen to Fuel
GO_2	Gaseous Oxygen
GCH_4	Gaseous Methane
CMOS	Complementary Metal-Oxide Semiconductor
ICCD	Intensified Charge-Coupled Device
OH^*	Hydroxyl Radicals Excited
OH	Hydroxyl Radicals Ground State
CEA	Chemical Equilibrium Applications

Chapter 1

Introduction

1.1 Propellant combination Methane/Oxygen

Liquid propulsion is widely used because it has several advantages: the energy density of this type of propellants tends to be higher than solid fuels and hence higher combustion temperature is reached. In addition, this kind of propulsion has a wide range of specific impulse, the thrust can be controlled (throttled) and moreover, since centrifugal turbopumps can be used to pump the propellant from tanks to combustion chamber, liquid propellant can be stored under low pressure. Contrarily, the need of pumps, piping and separate storage for fuel and oxidizer brings a disadvantage in terms of mass.

The most common propellant combination is hydrogen/oxygen. Hydrogen is a light and extremely powerful rocket propellant and it has the lowest molecular weight of any known substance. In combination with an oxidizer, such as oxygen, hydrogen yields the highest specific impulse, or efficiency in relation to the amount of propellant consumed, of any known rocket propellant. Because liquid oxygen and liquid hydrogen are both cryogenic, they can be liquefied only at extremely low temperatures. Liquid hydrogen has to be stored at about 20 K and handled with extreme care. To avoid that it could evaporate or boil, rockets fuelled with liquid hydrogen has to be carefully insulated from all sources of heat, such as rocket engine exhaust and air friction during flight through the atmosphere. Furthermore, once the vehicle reaches space, it has to be protected from radiant heat of Sun because, when liquid hydrogen absorbs heat, it expands rapidly; thus, venting is necessary to prevent the tank from exploding[1]. A relevant problem for the hydrogen propellant utilization consists of size of tank which contains hydrogen itself: as mentioned before, because the hydrogen density is low, the tank volume has considerable influential

dimensions. In addition, for hydrogen/oxygen propulsion, the associated system is costly for production also because the H_2 -storage requires expensive cooling technologies[2]. One of the candidate propellants for replacing hydrogen is methane. Unlike hydrogen, methane is defined as "Green Propellant". This family of propellants has many advantages: low toxicity (reduced risks for operation and safety precautions during handling and storage), low environmental impact (reduced pollution of environment on ground, atmosphere and space), low costs and good performances. Therefore, the combination of methane/oxygen propulsion is a convenient propulsive alternative to current hydrogen/oxygen engines due to higher methane density, the provided good performance, the good cooling capacity, the low soot production, the low cost management and the valid compatibility of the expected materials[2]. Hence, the methane utilization as propellant provides a lot of benefits over traditional hydrogen launch systems: indeed, because methane requires smaller tanks than hydrogen, the overall design becomes lighter. Methane is more stable than hydrogen in space over long periods of time, and it does not need such highly insulated cryogenic tanks. It also has a boiling point closer to oxygen boiling point, allowing a simple bulkhead design. Moreover, since methane and oxygen density are closer, a simpler turbopump can be built and, therefore, an advantage in terms of mass is gained. For these benefits mentioned, methane is a good candidate to replace hydrogen in future space programs, hence currently many test campaigns are being performed on the methane/oxygen propellants combination to calculate performance, and mainly to understand more about advantages and disadvantages.

The purpose of this work aims to show results obtained from the calculation of performance and emission imaging of a test campaign performed by using methane/oxygen.

1.2 Optical system for combustion diagnostic

Optical systems are appropriate for combustion diagnostics because the non-invasive nature of these systems allows data to be taken without inserting a probe into measurement region which, in current case, is critical because of hot environment. Despite the intrusive techniques have the advantage of taking direct information of the system under examination, they also have the disadvantage to be sensitive to system perturbation, especially in hostile environments like the combustion chamber. Hence, the correct way is to choose a non-intrusive technique which provides the advantage of accessibility and security along with accurate results.

The advantages of optical technique are numerous:

- Non-intrusive
- Instantaneous
- Excellent spatial and temporal resolution
- In-situ and real-time recording
- Expandable from 1D to 2D or 3D: from single point to planar
- Modular and flexible system setups to expand capability by adding hardware for multi-parameter measurements

At same time they also have some disadvantages:

- The need of an optical access because the radiation coming from the object may go through a complex path (windows, intermediate fluids, environmental air, and so on), with optical properties not well known or controllable
- Complex experiments because of experimental setup and hardware
- Sometimes complex models for the interpretation
- High cost
- The need of a good post-processing work
- The measurements will be performed at different times, they may not be carried out under the same conditions as the previous measurements.

This last disadvantage is due to the fact that optical measurements are always subject to positioning errors and they are also influenced by external factors. It will therefore be necessary to calibrate the equipment in the best possible way and with same conditions as the previous tests. Several measuring techniques exist and the diversity of these techniques depends on what one wants to measure and the results that one wants to achieve:

Table 1.1: Measuring techniques for combustion and flame characterization[3]

Measuring technique	Characteristics	Measurement results
PIV	Flame velocity and mixing	Velocity field in flame
LII	Soot analysis in flame	Concentration profile of soot
LRS	Flame temperature	Profile of temperature
PDPA	Flame velocity and propagation	Velocity and size of particulates
PLIF	Flame radicals in reaction zone	Concentration of OH and CH
PLIF	Flame pollutant analysis	Concentration of NO , CO and SO_2
CI	Flame radicals in reaction zone	Concentration of OH and CH

Particle Image Velocimetry (PIV) is a laser-based optical technique for the characterization of flow and turbulence dynamics in combustion processes. Typical PIV measurements use dual laser pulses to probe the flow field and determine the two velocity components of features of interest in a single plane simultaneously[4].

Laser-Induced Incandescence (LII) is a technology that offers a reliable means for spatially and temporally measuring the soot (black carbon, elemental carbon) concentration and primary particle size in engine exhausts and in ambient air. It is an extremely sensitive measurement technique that offers unparalleled measured dynamic range and requires no sampling systems, diluting systems, or consumables such as filters. It also provides real-time measurement (order of $10Hz$) and is suitable for dynamic measurements. The LII method involves rapidly heating soot residing or passing within a laser beam path using a high energy ($100 mJ$) pulsed laser source with duration typically less than $20ns$. Elemental carbon particles (soot) interact with the laser beam absorbing light which is converted into heat and increases the particle temperature. Thermal radiation or incandescence emitted from the soot particles is measured using collection optics and photodetectors. With appropriate calibration and analysis of the incandescence signal, information on the soot volume fraction, primary soot particle size, and specific surface area may be obtained[5].

Laser-Induced Rayleigh Scattering (LRS) is an important diagnostic tool for the measurement of flame structure as well as density and mixture fraction. If the pressure is known

on the flame, the density measurement can be converted to temperature. The technique provides the global image of the temperature distribution across the flame illuminated by the laser light. The LRS signal is linearly dependent on the gas number density and excitation laser power. It is also unaffected by quenching and saturation. However the elastic nature or Rayleigh scattering is difficult to be decoupled from the spurious elastic background like Mie scattering from particles and multi-scattering from optical windows. Hence an atomic or molecular filter, made of an optical cell filled with atomic or molecular gas, is generally required to provide the narrow absorption line to be detected. The typical configuration of system for LRS is made up of an injection seeded single mode Nd:YAG laser, ICCD camera, light sheet optics, synchronization unit, atomic or molecular filter, and control software[3].

Phase Doppler Particle Analyzer (PDPA) is a technique based on the Doppler shift of the scattered light signal from the particle, and it provides simultaneous velocity and size information. The technique is a single point measurement with extremely high spatial resolution of less than 100 microns. It also provides very high temporal resolution to track the concentration of particles going through the measuring volume[3].

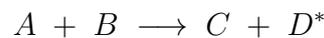
Planar Laser-Induced Fluorescence (PLIF) imaging of the combustion radicals provides a means of studying the combustion reaction zones. CH is difficult to measure (high-cost, low signal) while OH has a much stronger signal; hence, OH radical it is an important intermediate species in the oxidation of fuels and because it is formed in the flame front, OH is a commonly used marker for this region. A typical system consists of a Tunable Dye laser, Intensified CCD camera, laser light sheet generator, synchronization unit, control software and filters. The Tunable Dye laser is preferred because the desired wavelength can be obtained to excite the species of interest. The fluorescent signal is then collected by the ICCD camera with the appropriate filter and the analysis performed by the software gives the results of the concentration of the species. Furthermore, the amount of light detected by pixels in the camera depends on the concentration of the species being studied within the measurement zone of the flame and the local flow field conditions, i.e., temperature, pressure and mixture composition. PLIF is a useful technique for flame front studies in reacting flows. The application areas vary from laboratory burners to commercial internal combustion engines and gas turbine burners. PLIF is therefore ideally used for the measurement of concentration/mole fraction of species such as Na , OH , NO , O_2 , CH , CO or acetone, localised temperature, velocity, and pressure.

Flame shapes can be passively estimated from natural chemiluminescence without using a laser. *Chemiluminescence Imaging* (CI) is a simpler technique also used for flame studies, in which the chemical excitation of species is provided without using the laser light. The camera records the light emitted from chemically excited species such as OH , which are then denoted OH^* because they are in an excited state prior to emission of a photon as they return to the ground state. CI is useful in situations where it is technically difficult or too costly to apply PLIF such as optical engine diagnostics, where to follow single-cycle events it is preferred to acquire image data with high repetition rates[4].

Our studies will be based on *Chemiluminescence* phenomenon. The experimental setup and the hardware description will be explained in the next chapter.

1.3 Chemiluminescence

Chemiluminescence is the production of light by a chemical reaction in which two chemical species react to form an excited intermediate (at high energy) that releases part of its energy in the form of light photons. The light emitted by the flame may be used to monitor and control combustion. Referring to [6]: "Discrete emission spectra in the UV visible range correspond to electronically excited species produced in the chemical reactions in the flame:



This chemically excited radicals or molecule D^* may be destroyed by spontaneous emission ($D^* \longrightarrow D + h\nu$) or collisional quenching ($D^* + M \longrightarrow D + M$). Chemiluminescence corresponds to the spontaneous emission of photons ($h\nu = E_2 - E_1$ with E_2 the energy of the excited state and E_1 the energy of the final state). This emission generally takes place in the UV or visible range. Each molecule or radical produced in an excited state is responsible for a particular spectrum, which is related to its quantum properties, and can be identified". *Chemiluminescence* can be found in many processes which involve unstable and energetic intermediate species, such as combustion processes. It is important to note that although the chemiluminescence light investigated in this study is generated by combustion processes, the origin of chemiluminescence lies not only in the temperature rise caused by combustion. Thus, a direct proportionality between chemiluminescence and heat release cannot be expected a priori[7].

1.3.1 Flame Spectrum

In the most common type of flame, hydrocarbon flames, the most important factor determining the color is the supply of oxygen and the extension of fuel-oxygen premixture, which determines the combustion speed and, therefore, temperature and reaction paths, thus producing different shades of color[8]. The color and temperature of a flame depend on the type of fuel involved in combustion. The high temperature of flame causes the decomposing of vaporized fuel molecules, forming various incomplete combustion products and free radicals like the radicals OH^* , CH^* , C_2^* , and the molecule carbon dioxide CO_2^* . The spectrum of a flame is a superposition of emissions from these four electronically excited species. Hence, flames can be characterized by their emission spectrum. These are defined by emitted radiance distributions as a function of wavelength λ :

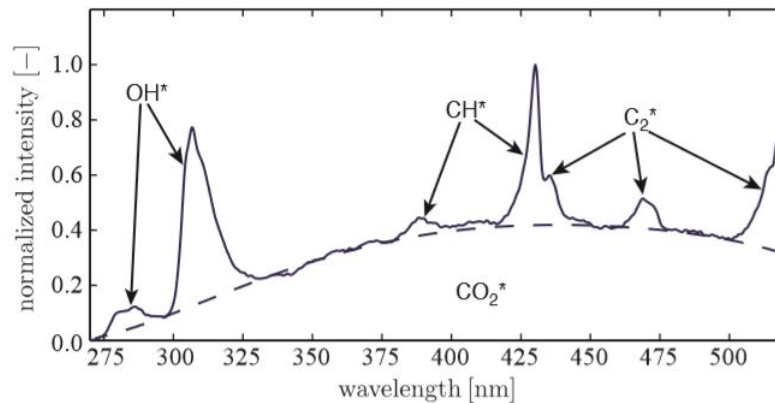


Figure 1.1: Typical chemiluminescence spectrum of an atmospheric methane-air flame.

A typical *Chemiluminescence* spectrum of a methane/air flame at atmospheric pressure is showed in Fig.1.1. The spectrum extends from below 300 nm to 600 nm and gives the flame the well known blue color. Therefore, chemiluminescence of excited radicals as CH^* , C_2^* and OH^* created inside of the reaction zone, constitutes a signature of burning conditions([9],[10]). These three types of chemical species are the most plentiful excited radicals produced within flame front, emitting as narrow bands in the visible region of electromagnetic spectrum (Fig.1.1), centered around the wavelengths 310 nm (OH^*), 430 nm (CH^*) and 515 nm (C_2^*)[11]. It is interesting to note that the radiation from the excited hydroxyl radical OH^* is found in the combustion of all fuels containing hydrogen, such as in hydrogen and hydrocarbon flames. Hydrogen flames, by including nitrous oxide-hydrogen flames, have the characteristic of a weak background emission. The spectra always shows the marked OH^* bands with band heads at 281 nm, 306 nm (strong) and 343 nm. Unlike the hydrogen flame spectra, the hydrocarbon flame spectra is more

complex because it does not only produce bands and the continua observed in hydrogen flames, but also emit radiation of hydrocarbon radicals, as showed is Figure 1.1. In addition, every type of flame also can be characterized by their absorption spectrum which is qualitatively similar to emission spectrum. Hence, the overall observable spectrum of a flame generally is a function of both emission and absorption. To deepen this subject more details are expressed in the A.Brockhinke, J.Kruger, M.Heusing and M.Letzgus's article[12] and T.Fiala's PhD thesis[13]. However, the current study will focus on OH^* *Chemiluminescence*. For this purpose, a OH^* filter was used in front of the sensor of an *Intensified* CCD camera during the test campaign. The advantage of filtered measurements is that the measurement effort is drastically reduced: a spectrograph to solve the wavelength is not necessary and the camera does not have to sacrifice a spatial dimension for the wavelength, besides the fact that an optical filter has a much lower cost than a spectrograph[13]. By installing this filter, it is possible to obtain an idea how the OH^* concentration in the flame changes by varying combustion conditions (*Load Points*), such as pressure in combustion chamber and mixture ratio: indeed, in current test campaign, it will be possible to note that, by changing the pressure and the mixture ratio, the OH^* concentration will undergo considerable variations(*Chapter 4*).

Chapter 2

Experimental Setup and Hardware description

2.1 Hardware Description

The current test campaign is performed with a modular single-element combustion chamber. It consists of two chamber segments, one with 174 *mm* and another with 145 *mm*, and one nozzle segment with length 20 *mm*. The nozzle has an usual configuration, a 4.8 *mm* × 12 *mm* rectangular cross section, while internal combustion chamber dimensions are presented in Table 2.1.

Table 2.1: Combustion chamber geometry

Length	290	[mm]
Width	12	[mm]
Height	12	[mm]
Throat height	4.8	[mm]
Contraction Ratio	2.5	[-]

The combustion chamber used for the tests is capacitively cooled and it has a 12 *mm* × 12 *mm* square cross section (Figure 2.1). As mentioned in the previous chapter, it operates with gaseous oxygen and methane as propellants. The material selected for the combustion chamber and nozzle segments is oxygen-free copper (Cu-HCP) and it has several advantages: good electrical and thermal conductivity, excellent corrosion resistance and formability, good weld ability and recyclable. Anyway, the combustion temperature

can not exceed a certain value, otherwise a reduction of the nozzle throat is caused by melting of the material: for this reason, the pressure, the mixture ratio and the burning times have to be contained.

The combustion chamber is provided with equally spaced pressure transducers and thermocouples type T mounted in the wall along the chamber axis to characterize the combustion process and to monitor heat release (Figure 2.2). In order to protect the quartz window from the heat loads of combustion, a film cooling system using gaseous nitrogen as coolant is adopted. It is assumed that the film cooling mass flow does not influence the near-injector flame stabilization in a significant way for two reasons:

1. The film cooling mass flow rate is only a small percentage of the total mass flow rate
2. A non-reactant coolant is used

The hardware system with which tests were performed is the same explained in F. Winter et al's paper, so as mentioned in [14]: "The flat window and the rectangular cross section of the hardware allow optical access to the flame interaction in the near injector area. This setup avoids certain disadvantageous effects, which occur when a flat window is mounted in a round combustion chamber, such as flow disturbances caused by the presence of window corners".

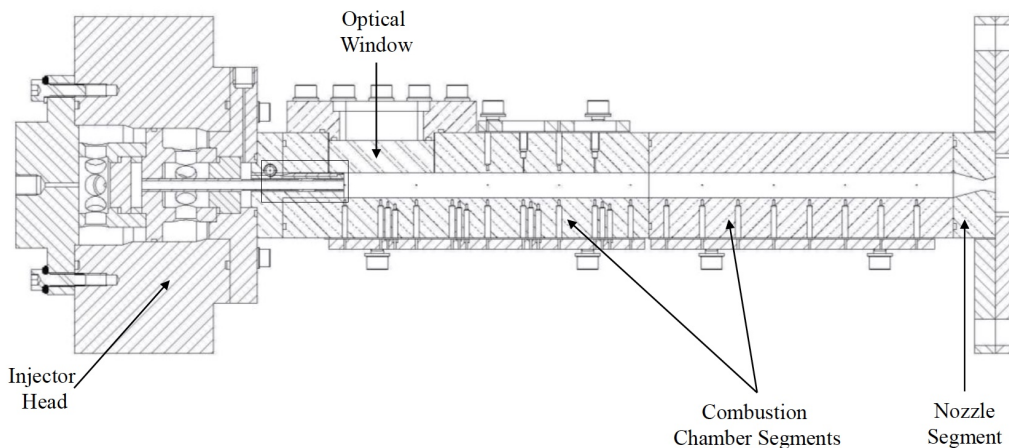


Figure 2.1: Combustion chamber section

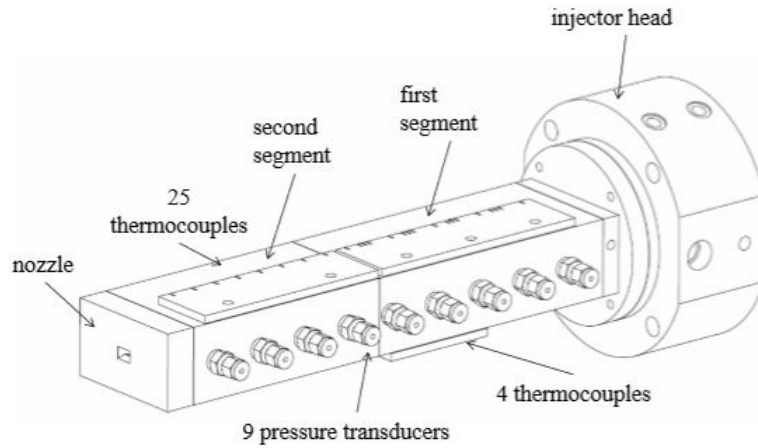


Figure 2.2: Combustion chamber configuration

A shear coaxial injector element is integrated as shown in Figure 2.3 with dimensions presented in the Table 2.2. For simplicity, no tapering or recess is applied.

Table 2.2: Injector geometry

GO_2 inner diameter	4	[mm]
GO_2 post wall thickness	0.5	[mm]
GCH_4 external diameter	6	[mm]
Injector area Ratio	0.7	[-]

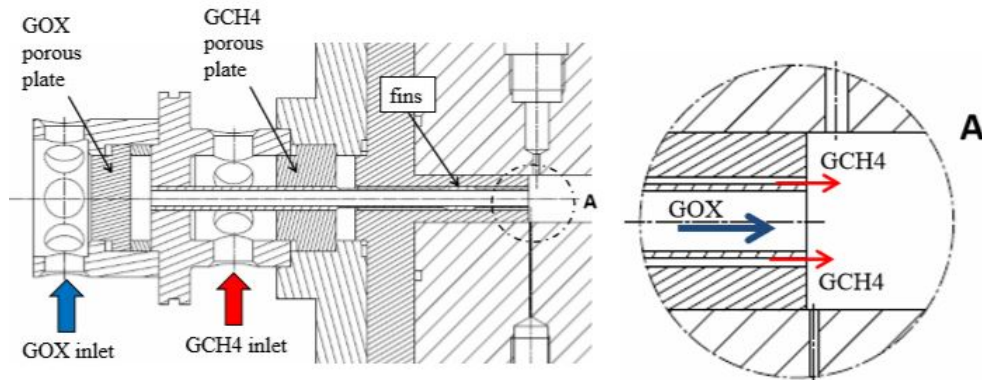


Figure 2.3: Injector geometry

Furthermore, to ensure homogeneous injection conditions in terms of temperature, pressure and velocity profile and to reduce the upstream feed lines, two porous plates are placed in the oxidizer and fuel manifolds respectively (Figure 2.3).

As previously mentioned, a quartz optical window is inserted into the combustion chamber wall (Figure 2.4) to monitor the flame. The choice of this material is due to the fact that the quartz is characterized by a low coefficient of thermal expansion and an exceptional thermal stability. In addition, the quartz resistance to thermal shocks is equally excellent: if heated to a temperature of 1100°C and then instantly cooled to 20°C for three times, the quartz shows no signs of breakage. However, despite it has good thermal properties, at high temperatures the material can expand. For this reason the quartz window size is slightly smaller than its insert area to avoid that, in case of material expansion, some internal cracks can arise. To amortize shocks on four sides of the insert area of the combustion chamber wall, very thin sheets of graphite have been placed: the graphite sheets have the task of filling the spaces of tolerance and keeping the window firmly in position, and therefore to soften shocks.

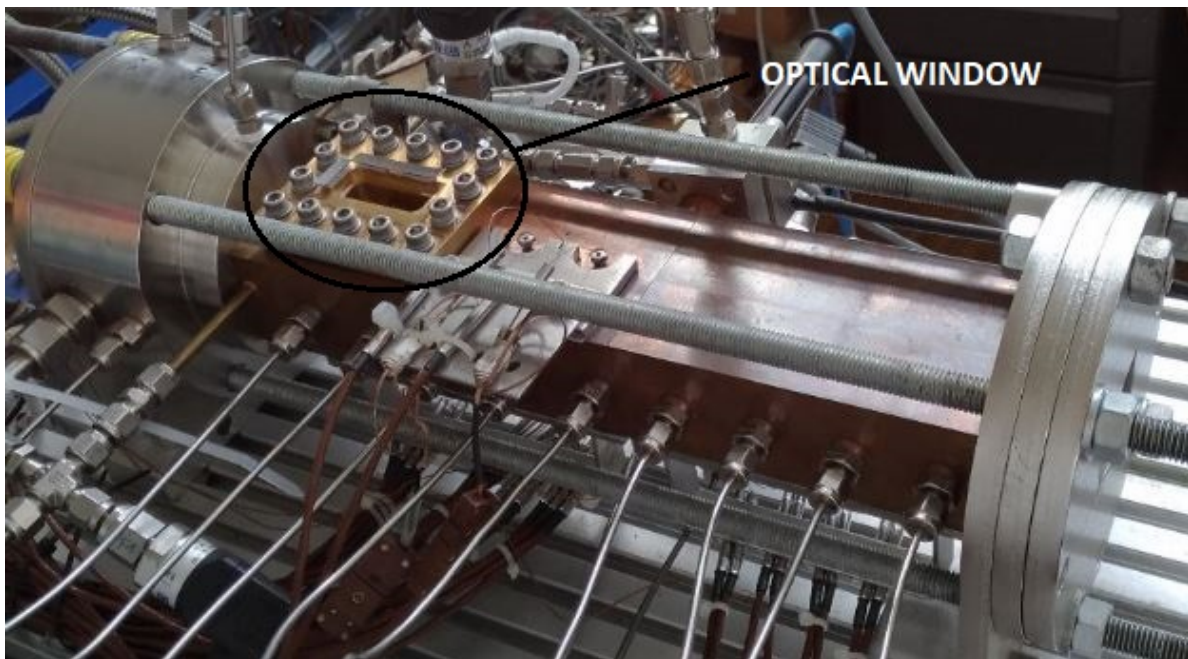


Figure 2.4: Combustion Chamber and Optical Window

Due to its high degree of purity, the quartz has also optical properties better than a traditional glass. It is possible to observe the quartz transmission spectrum as a function of the wavelength (Figure 2.5):

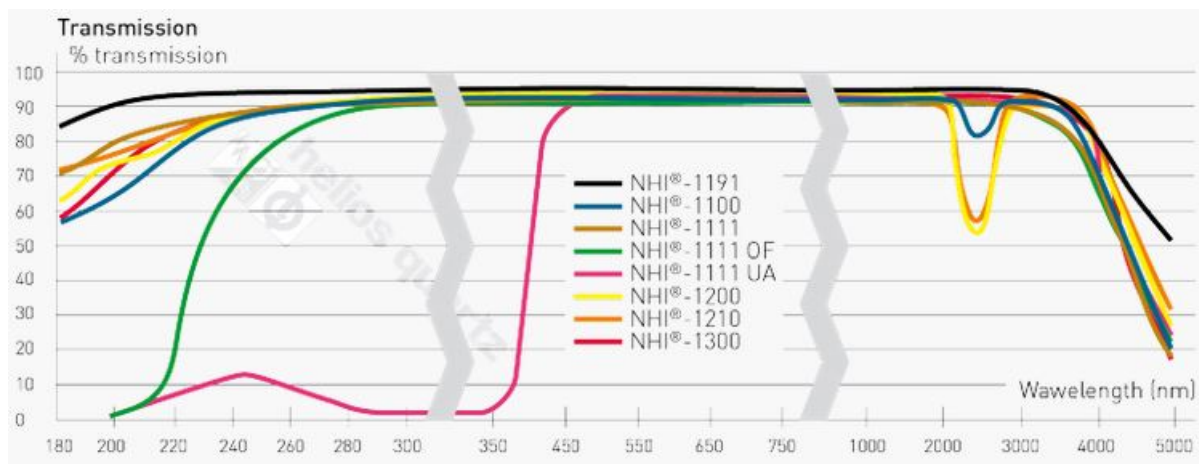


Figure 2.5: Transmission Spectrum of the Quartz[15]

From the graph it is possible to see that the transmission spectrum has a yield of 90–95% for the wavelengths of our interest. However, this transmission capacity decreases during the test campaign if the same quartz window is always used. This problem is mainly related to the recirculation zone of flame which causes a deposition on quartz window of unburnt carbon particles (*soot*, Figure 2.6) generated by a hydrocarbon incomplete combustion, such as methane.



Figure 2.6: Soot

2.1.1 Temperature and Pressure Measurement

As also described in [16], in Figure 2.2 a combustion chamber schematic and the associated sensor locations is given. For a better understanding of complex heat transport processes, equally spaced pressure transducers on the side wall provide a well resolved measurement of the wall pressure distribution along the chamber axis. Then, for injection conditions, thermocouples of Type *K*, with 0.5 mm diameter, and pressure transducers are installed in the chamber manifolds, prior the porous plates. To determine the temperature field within the chamber material, clusters of Type *T* thermocouples of 0.5 mm diameter are located at different distances (1, 2 and 3 mm) from the hot gas wall. The Type *T* thermocouples are mounted with a regular path of 17 mm in the upper surface of first and second segment, along the combustion chamber center plane. A spring loaded system is present to ensures a continuous contact between the thermocouples tip and the base of hole, providing a constant force of about 2 N: this setup aims to minimize the chance of potential loss of contact as the material undergoes expansion and contraction due to changes in temperature or vibrations during the hot run. Furthermore, two coaxial Type *T* thermocouples (*Medtherm*) are flush mounted with the hot wall. These *Medtherm* thermocouples are press-fitted into the chamber wall, in corresponding axial positions in the lower surface of the first segment. In order to ensure better contact, the tip has been polished to match the flat surface of the chamber. The thermocouple location pattern is shown in Figure 2.1.

2.2 Experimental Setup

2.2.1 Optical Setup

Through the optical window of combustion chamber photos are taken with an ICCD (*Intensified Charge Coupled Device*) camera to detect the spontaneous emission of intermittently existing hydroxyl (OH^*) radicals by using a OH^* filter in front of camera lens. In Figure 2.7 the optical setup is represented:

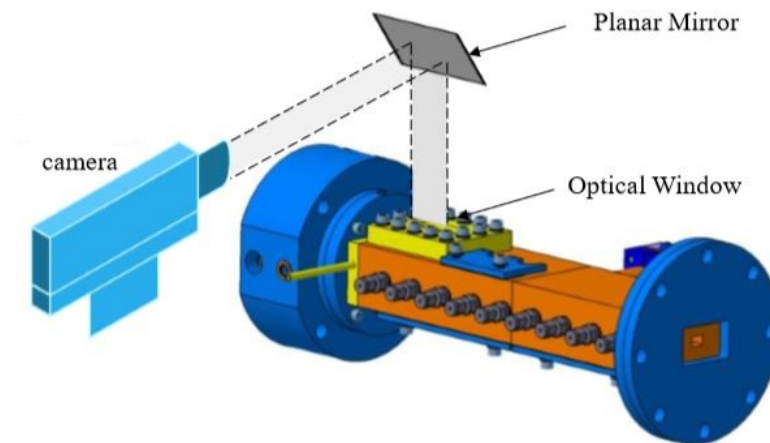


Figure 2.7: Optical setup

The camera was fixed on an optical bench next to the test bench and the image of the combustion chamber was reflected into the camera sensor with a planar mirror, which was positioned above the optical window with a 45° angle. This setup was chosen to protect this sensitive camera from possible damage. Furthermore, the camera was set up at the same distance from the combustion chamber to obtain a similar optical resolution for all test cases. The reason why each test is preceded by a calibration resides in the fact that a small perturbation can move the planar mirror or the optical bench: this phenomenon can lead to a different resolution of the captured images or even the non-focalization of the flame.

2.2.1.1 ICCD Camera

The *Intensified* CCD Camera adopts a CCD sensor, similar to a CMOS sensor. These sensors represents the heart of a camera, or the instrument by which it can possible to capture the image converting it into digital format. They consist of a silicon device with a photosensitive surface, based on a matrix of photodiodes able to transform and convert a light signal, composed of photons, into an electrical signal, composed of electrons, following the same principle of the simplest solar cells (panels photovoltaic systems) for the production of electricity. In particular, for the *Complementary Metal-Oxide Semiconductor* (*CMOS*) sensor, the conversion of the light level into digital data takes place directly inside the sensor through the amplifier and the *A/D* (*Analog-Digital*) converter of each photodiode, while for the Charge-Coupled Device (*CCD*) sensor, the conversion of the light level to digital data takes place outside the sensor using a dedicated chip. ICCD cameras can exploit gain to overcome the read noise limit but also have the added feature of being able to achieve very fast gate times. The gating and amplification occurs in the image intensifier tube (Figure 2.8). The Image intensifier tube is an evacuated tube which comprises the *Photocathode*, *Microchannel plate* (MCP) and a *Phosphor* screen, and the properties of these determine the performance of the device. The photocathode is coated on the inside surface of the input window and it captures the incident image. When a photon of the image strikes the photocathode, a photoelectron is emitted, which is then drawn towards the MCP by an electric field. The MCP is a thin disc (about 1 mm thick) which is a honeycomb of glass channels typically 6-10 μm , each with a resistive coating. A high potential is applied across the MCP, enabling the photoelectron to accelerate down one of the channels in the disc. When the photoelectron has sufficient energy, it dislodges secondary electrons from the channel walls. These electrons in turn undergo acceleration which results in a cloud of electrons exiting the MCP. The degree of electron multiplication depends on the gain voltage applied across the MCP which can be controlled in the camera. The output of the image intensifier is coupled to the CCD typically by a fiber optic coupler. With a suitably high quality image intensifier, the lens coupled arrangement can also produce a better quality image as the fiber-to-fiber variations and blemishes are removed from the system. Disadvantages of lens coupled systems are larger physical size, lower coupling efficiencies and increased scatter. Specialist power supplies are needed to operate the *Image intensifier*.

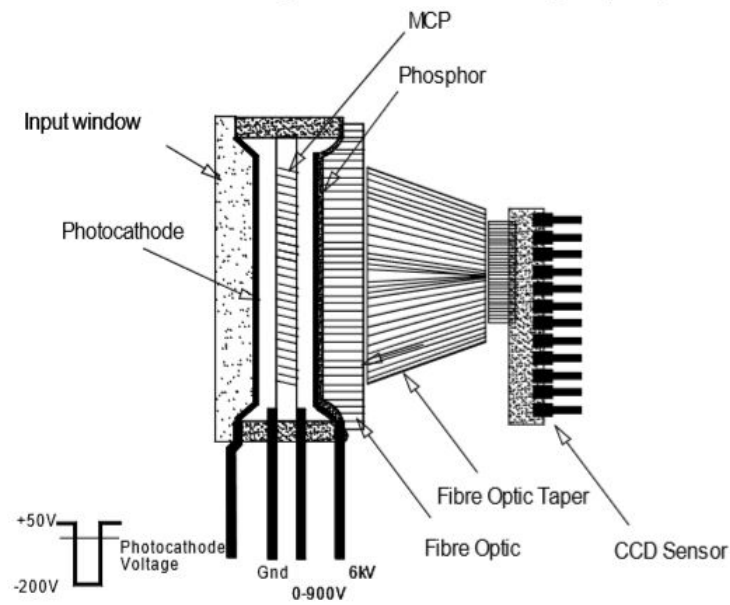


Figure 2.8: Cross section through the optical part of an Intensified CCD camera (with frame transfer CCD)

In particular, the ICCD camera of the current study is a *FlameStar 2(F)* (by *LaVision* manufacturer) and the whole system is shown in Figure 2.9:

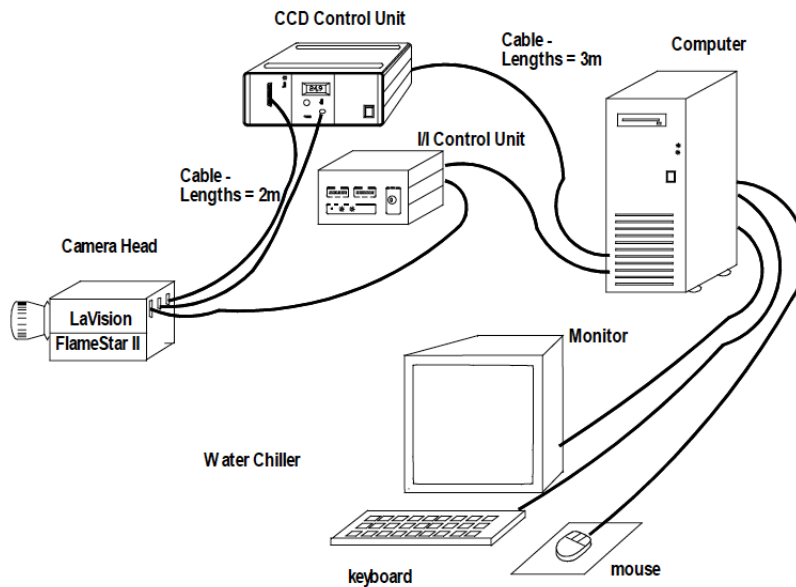


Figure 2.9: FlameStar II System

The heart of the *FlameStar 2(F)* system is the camera head. Hence it consists of an image intensifier that is fiber optically coupled to the CCD sensor. The *Image Intensifier* (I/I) is operated by the I/I control unit. It contains electronics to set the intensifier gain and the opening time (gate width) of the *Image Intensifier*. The CCD is operated by the *CCD Control Unit* (CCU). It contains the CCD electronics and the Thermoelectric Rtabilization (TE). The whole system is under control of a *Personal Computer* (PC). Image acquisition as well as image processing is performed under control of LaVision's DaVis software[17]. This camera is used to capture the spontaneous emission of intermittently existing hydroxyl (OH*) radicals. For the current test campaign a 10 gain and a 50 μs exposure time are set. It is important to underline that a camera's shutter determines when the camera sensor will be open or closed to incoming light from the camera lens. The shutter speed specifically refers to how long this light is permitted to enter the camera. Hence "*Shutter speed*" and "*Exposure time*" refer to the same concept, where a faster shutter speed means a shorter exposure time. However, for each test the camera setting is the same, in order to guarantee a useful comparison between cases under examination.

2.3 Operating Conditions and Sequence

To ignite the propellant mixture a torch igniter is used. The igniter works with methane gas and oxygen and it is located in the middle of the combustion chamber respect to the axial direction with zero recess length. Through pressure regulators it is possible to control the propellant, purge gas and film cooling mass flow rate. To start the combustion, a test sequence is programmed into the main control system using a software called LabView (Figure 2.10). The sequence is divided into three main periods:

1. transient start-up with ignition
2. main combustion chamber operation
3. shut down

The transient start-up with ignition and the shut down will be shown briefly in the last chapter. However, the igniter works for 300 ms to ensure ignition of the combustion chamber for a total combustion time of 3 s. After successful ignition of the main combustion chamber the igniter is switched off. The same sequence is applied to all tests performed.

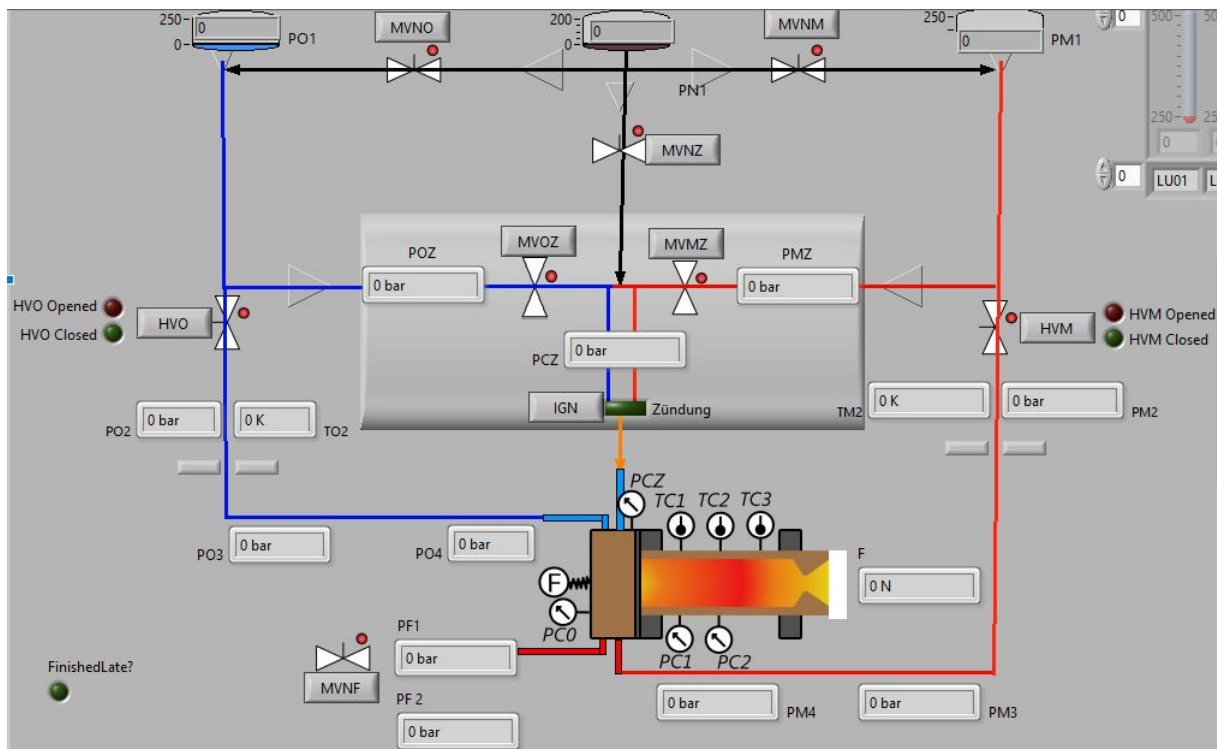
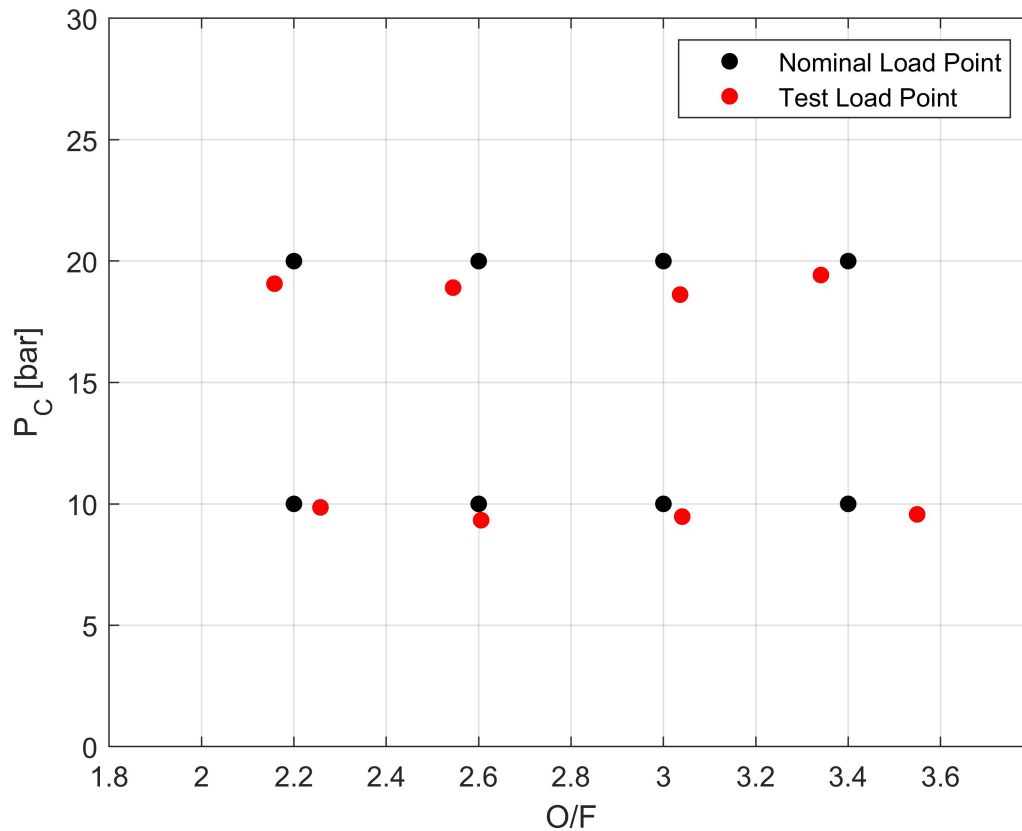


Figure 2.10: Main Control System (LabView)

2.3.1 Load Points

The test campaign was performed for two different pressure cases in the combustion chamber: 10 *bar* and 20 *bar*. At each pressure, different *ROF* are considered (*Load Points*, Figure 2.11) with 10% of film cooling percentage. For all cases, pictures were taken with the ICCD camera with spectral filter to capture the spontaneous emission of intermittently existing hydroxyl (OH^*) radicals. For the determination of the load points, the characteristic velocity is calculated with *NASA CEA2 software* tool by considering standard pressure and temperature values. Anyway, test load points do not always coincide with the nominal load points(Figure 2.11): this problem could be linked to three main reasons: during test campaign the atmospheric conditions were not always the standard ones, the regulation of the pressure regulators was not very precise and, finally, the influence of combustion efficiency

Figure 2.11: Test and Nominal Load Points



Chapter 3

Digital Image Processing

3.1 Overview

In the current study an image processing is used to prepare the flame images for the data analysis. Indeed, optical analysis is often a principal method for acquiring scientific data and generally it requires that its features are well defined, either by edges, brightness, shadows, colors, or some combination of these factors. The image processing basically includes the following three steps:

1. Importing the image
2. Analysing the image
3. Output

The type of method used for image processing is the *Digital Image Processing*. Digital image processing techniques help in treatment of digital images by using computers. The three general phases that all types of data have to undergo are pre-processing, post-processing and data extraction. The pre-processing and post-processing will be discussed in detail in the next paragraphs, while the data extraction will be carried out in *Chapter 4* to discuss on results obtained.

3.2 Image Pre-processing

The aim of pre-processing is an improvement of image data that suppresses unwanted distortions or enhances some image features important for further processing[18]. Some of these improvements used in current study are the pixel brightness corrections or *shading correction* and the *angle correction* caused by calibration problems during the image acquisition.

3.2.1 Shading Correction

When an image is acquired many factors exist which can affect the brightness of the image, mainly lights and shadows caused by the external environment and the different detection of light along a certain direction by camera sensor. The influence of external brightness was resolved considering an image acquisition of only the area where the flame is generated and by applying a shading correction to that image. Subsequently, this correction was applied to the flame image. The influence of the camera sensor was solved by acquiring an image with covered sensor (black image) and by extracting its the brightness gradient. More details are present in the G. Laera's Master thesis. A case of shading correction is shown to demonstrate that pixels intensities values had not significant variations:

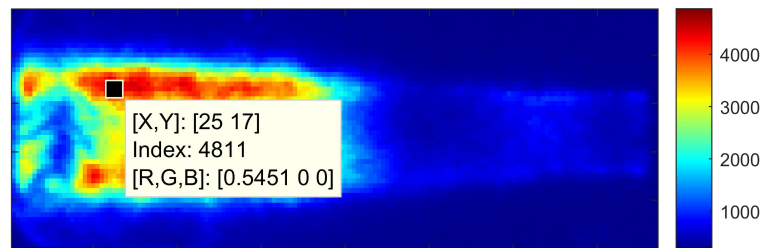


Figure 3.1: Flame without Shading Correction, Methane, 20 bar, ROF 3.4

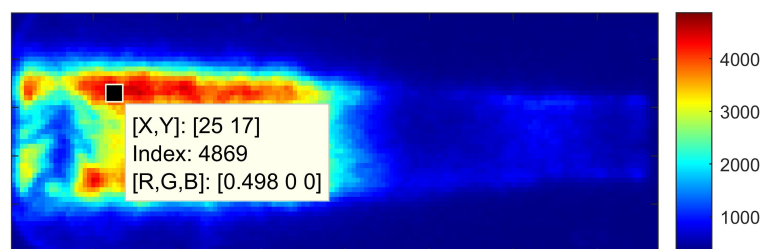


Figure 3.2: Flame with Shading Correction, Methane, 20 bar, ROF 3.4

- Maximum pixel intensity value without *shading correction* = 4811.0
- Maximum pixel intensity value with *shading correction* = 4869.3

By calculating the percentage error, it is possible to state that corrections applied to images due to shading correction are negligible, indeed:

$$\%error = \frac{4869.2736 - 4811.0}{4869.2736} \times 100 \simeq 1.2 \%$$

From the Figure 3.1 and 3.2 it is possible to notice that there is a flame zone in which an anomalous flame shape is present. This shape is not due to the flame itself, but to the presence of a crack inside the optically accesable quartz window. This local break could be caused most likely by thermal fatigue, or by pick pressure in the combustion chamber.

3.2.2 Angle Correction

Before each test an image calibration is performed because there are several factors which can affect the relative position between the mirror, on which the flame image is projected, and the camera sensor: for example, a sudden movement of the optical bench on which the camera is fixed or an inclination of the mirror caused by hardware maintenance between one test and another. To overcome this problem MATLAB tools (see Appendix) was used to correct the inclination of image in order to improve the extraction of experimental data without altering them. For a better understanding of the applied corrections, the hydrogen and oxygen combustion case of an other test campaign is used (G.Laera's test campaign), in particular by considering a 10 *bar* pressure in the combustion chamber and a 4.4 mixture ratio (*ROF*). The result is shown in the following figures where a counter-clockwise rotation of 1.5° was applied to the image (Figure 3.4):

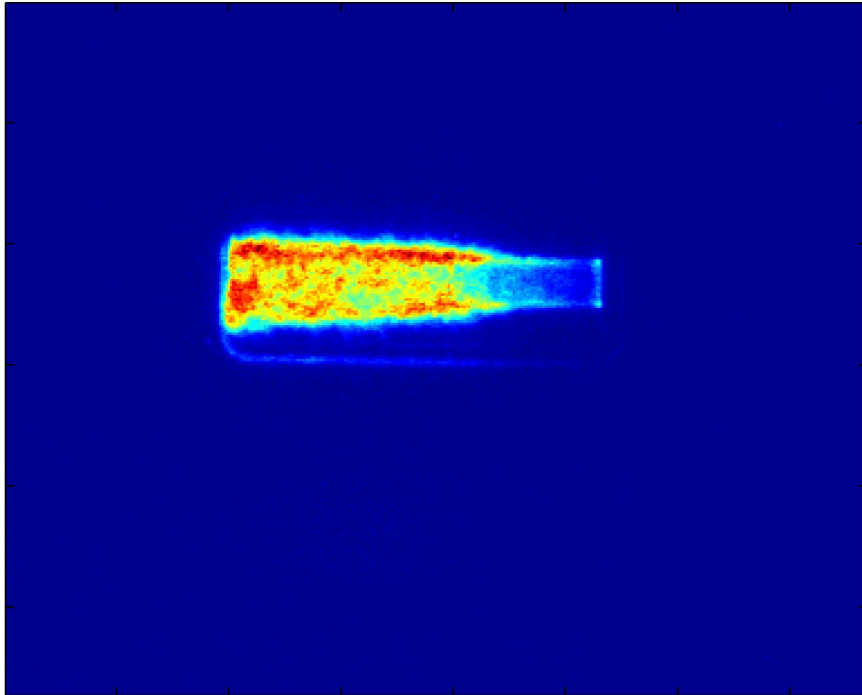


Figure 3.3: Case *hydrogen/oxygen*, 10 bar, ROF 4.4, no angle correction

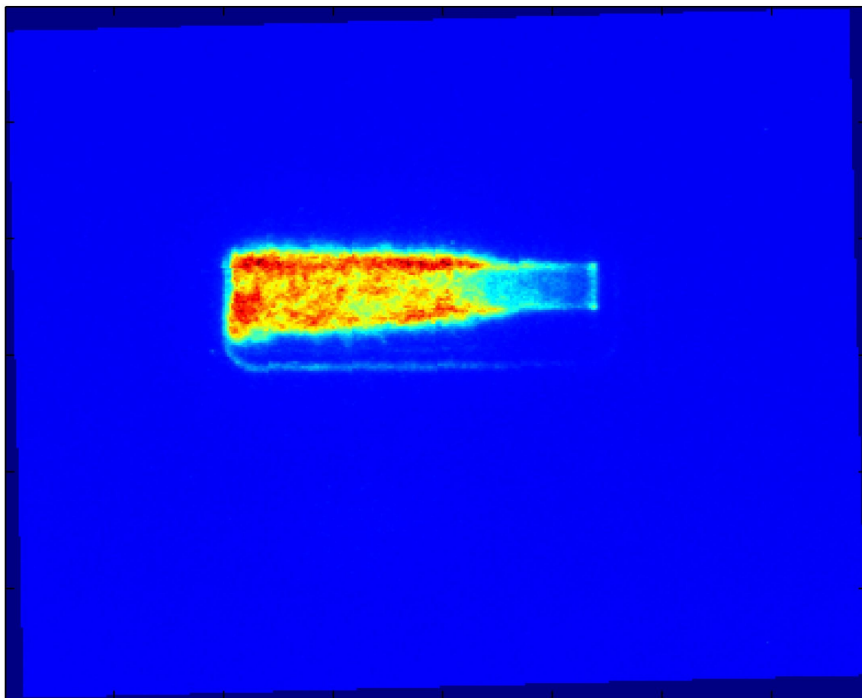


Figure 3.4: Case *hydrogen/oxygen*, 10 bar, ROF 4.4, angle correction (1.5°)

3.3 Image Post-processing

In the previous paragraph corrections were applied to images to remedy problems during the acquisition of an image. In this paragraph, however, some modifications to images will be made to facilitate the extraction of experimental data: the average image and the image framing.

3.3.1 Average Image

Photos taken by the ICCD camera were saved in the form of *.txt* files, hence directly as a two-dimensional array. The camera captures a series of instantaneous images in number proportional to the frame rate. From these instantaneous images the average image is created, mainly for three reasons:

1. the average image does not take in account the fluctuations of the flame
2. with the average image a noise damping is generated
3. the average image allows one to have a better overview of the overall flame shape during burning time.

Each image taken is imported into MATLAB in a two-dimensional array form, $A(i,j)$, where the index i takes into account the number of rows and the index j the number of columns. Anyway, the dimensions of matrix depends on the image resolution that, in the case of ICCD camera adopted, is 384×286 . All two-dimensional matrices associated with instantaneous images of three seconds of burning time were used to create a single three-dimensional matrix, $B(i,j,k)$, where the k index takes into account the number of photos used for the average. An example is shown in Figure 3.5, where at each value of k corresponds a single photo of flame.

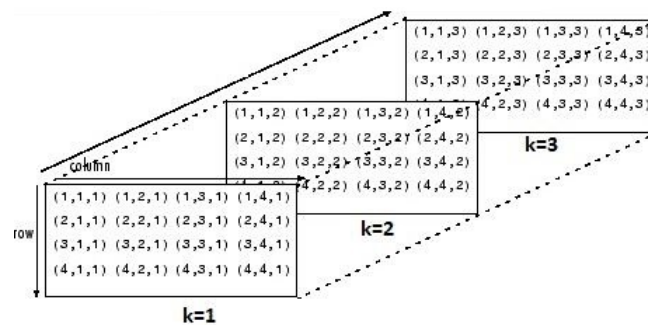


Figure 3.5: Example of a Three-dimensional Matrix

The calculation of the image average takes place through a for loop in MATLAB: a generic element of three-dimensional matrix $B(i,j,k)$ is considered, indices i and j are fixed and the index k is left to vary between 1 and N , where N indicates the number of photos captured by camera. Due to its frame rate, the camera has taken five photos during three seconds of burning time and, therefore, five matrices can be indicated as follows: $A_N(i,j)$ with $N = 1 \dots 5$, $i = 1 \dots 384$ and $j = 1 \dots 286$.

The $B(i,j,k)$ matrix is the three-dimensional matrix in which for:

- $k=1$, $B(i,j,1) = A_1(i,j)$ (Figure 3.6)
- $k=2$, $B(i,j,2) = A_2(i,j)$ (Figure 3.7)
- $k=3$, $B(i,j,3) = A_3(i,j)$ (Figure 3.8)
- $k=4$, $B(i,j,4) = A_4(i,j)$ (Figure 3.9)
- $k=5$, $B(i,j,5) = A_5(i,j)$ (Figure 3.10)

The two-dimensional matrix of average image $C(i,j)$ (Figure 3.11) is created by averaging single elements of three-dimensional matrix $B(i,j,k)$, by fixing indices i and j each time and by letting to vary the k index. For example:

$$C(1,1) = \frac{B(1,1,1) + B(1,1,2) + B(1,1,3) + B(1,1,4) + B(1,1,5)}{5}$$

$$C(1,2) = \frac{B(1,2,1) + B(1,2,2) + B(1,2,3) + B(1,2,4) + B(1,2,5)}{5}$$

.

.

.

$$C(384,286) = \frac{B(384,286,1) + B(384,286,2) + B(384,286,3) + B(384,286,4) + B(384,286,5)}{5}$$

The case of flame generated by combustion process between methane and oxygen with 20 *bar* pressure and 2.2 *ROF* is considered for a better representation of current method.

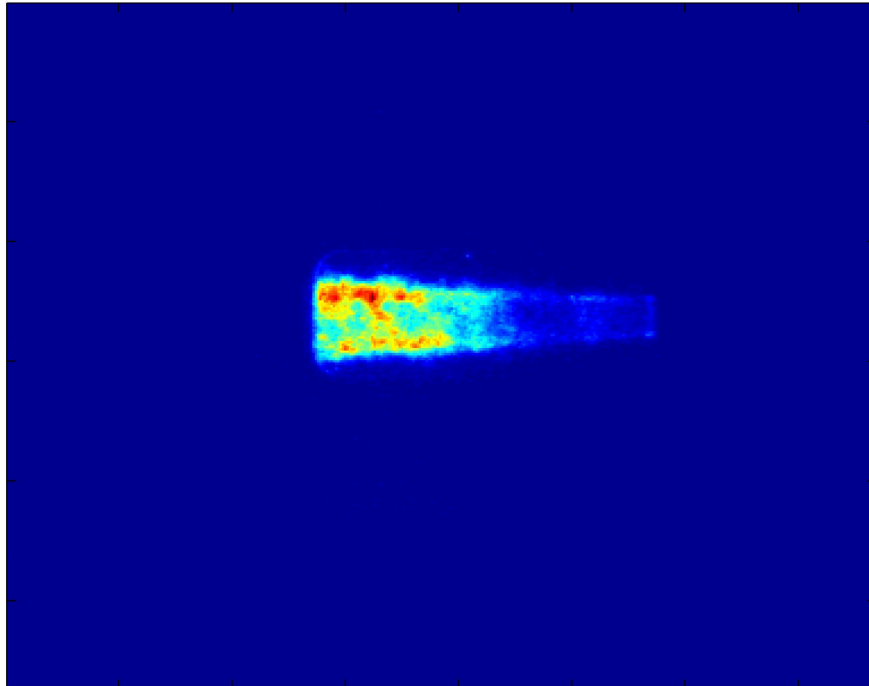


Figure 3.6: Case *methane/oxygen*, 20 bar, *ROF* 2.2, First Instantaneous Image

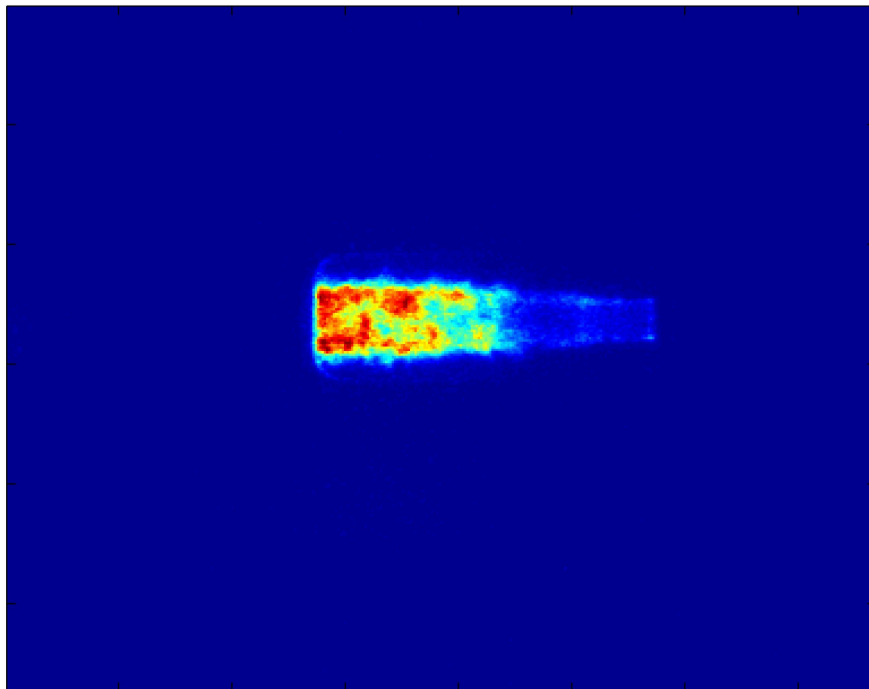


Figure 3.7: Case *methane/oxygen*, 20 bar, *ROF* 2.2, Second Instantaneous Image

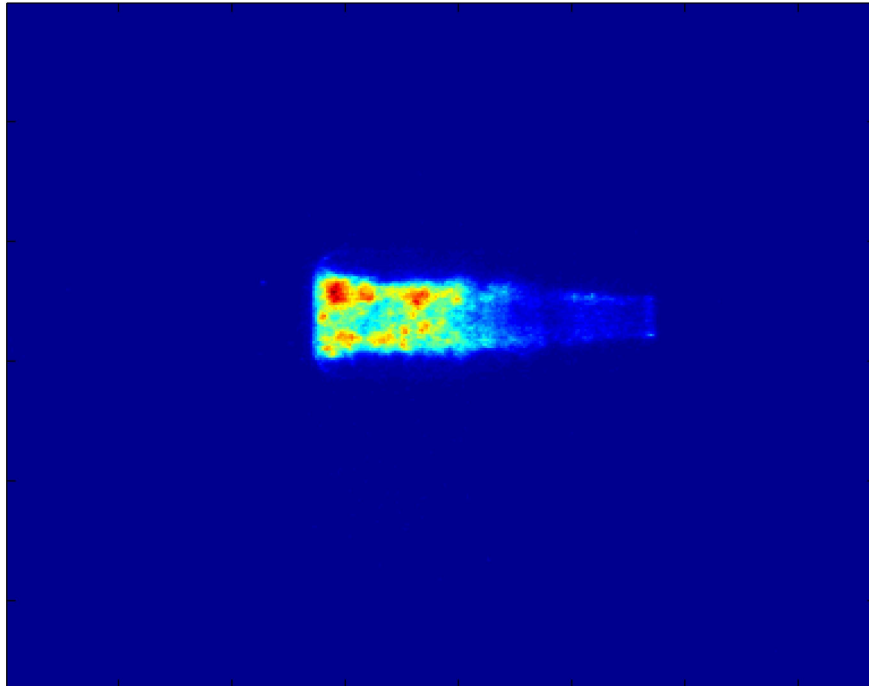


Figure 3.8: Case *methane/oxygen*, 20 bar, *ROF* 2.2, Third Instantaneous Image

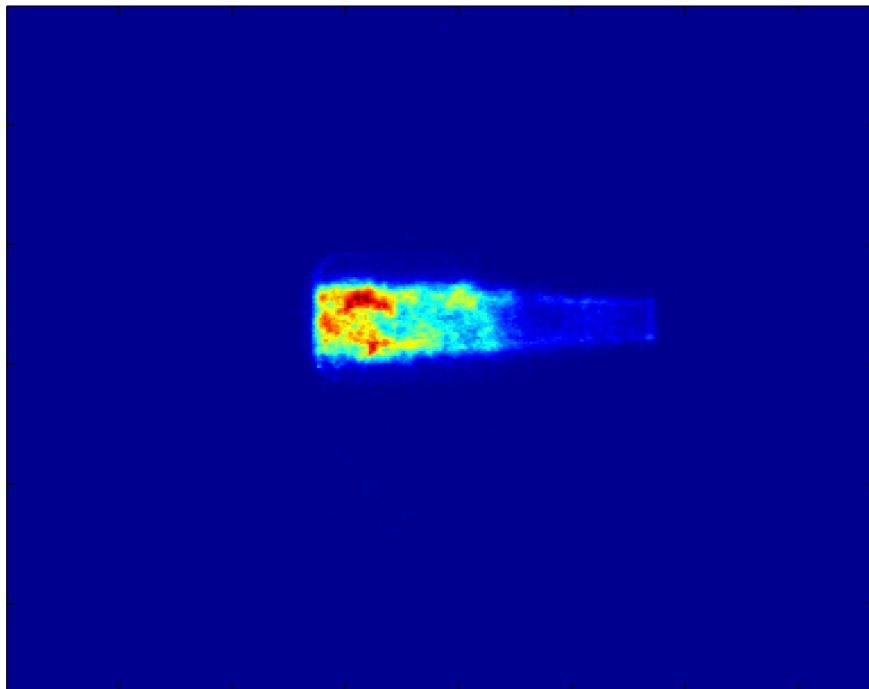


Figure 3.9: Case *methane/oxygen*, 20 bar, *ROF* 2.2, Fourth Instantaneous Image

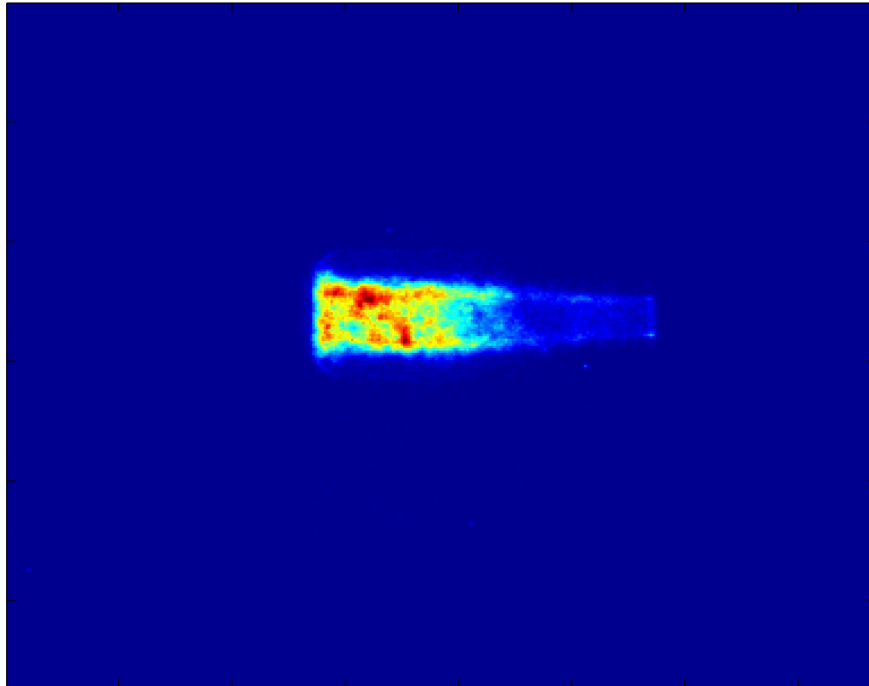


Figure 3.10: Case *methane/oxygen*, 20 bar, *ROF* 2.2, Fifth Instantaneous Image

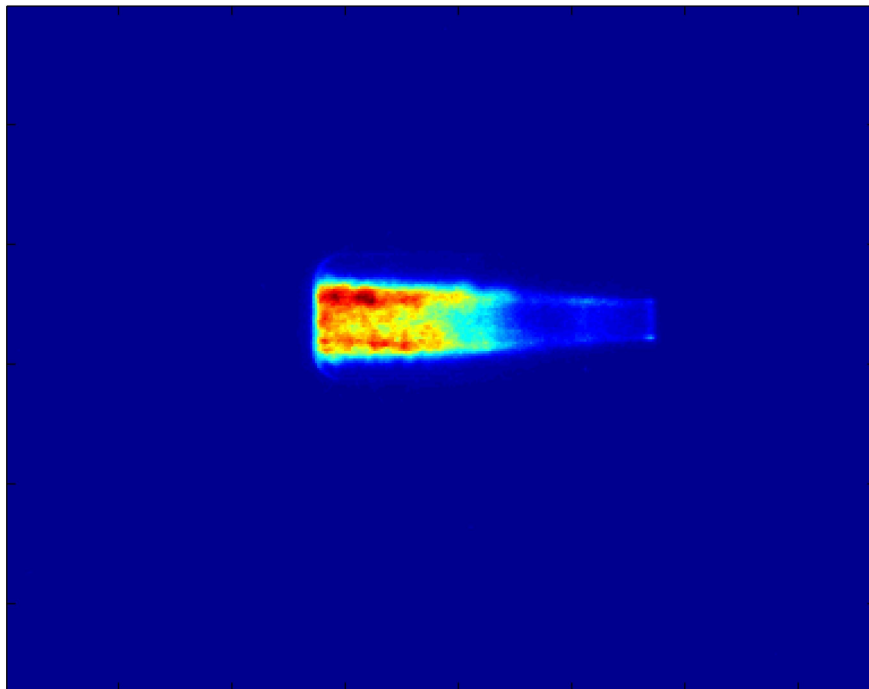


Figure 3.11: Case *methane/oxygen*, 20 bar, *ROF* 2.2, Average Image

3.3.2 Image Framing

The image captured by the camera (Figure 3.12) contains not only the optical window of combustion chamber, but also the external part of hardware. To facilitate the extraction of experimental data, only the image of the area of interest is considered.

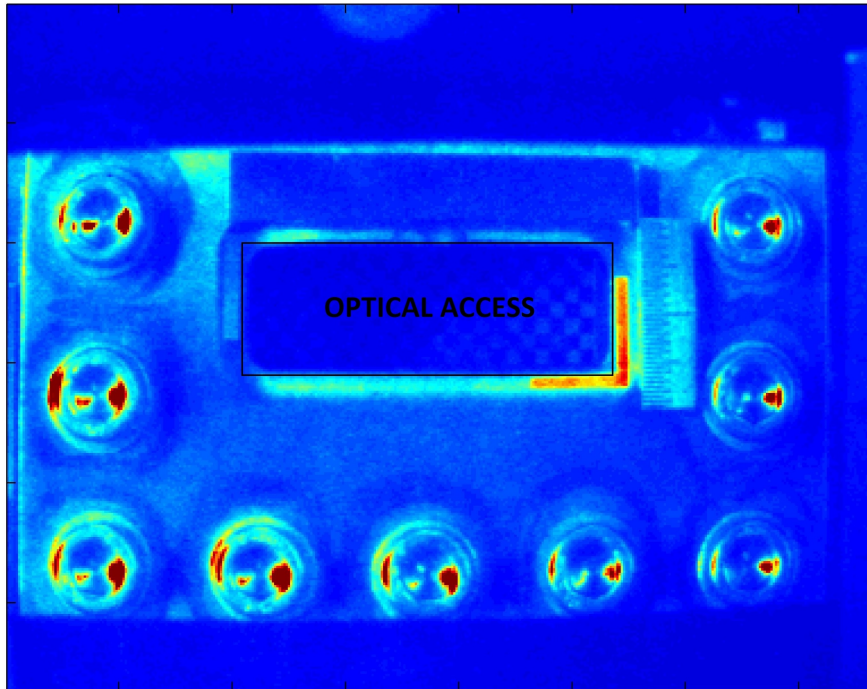


Figure 3.12: Image Captured by ICCD Camera

The optical access has $40 \text{ mm} \times 12 \text{ mm}$ dimensions. To cut this part from the whole captured image, pixels of the image are considered. As mentioned in the previous paragraph, every captured image has a 286×384 resolution which represents the number of all pixels presents in the image (Figures 3.12). In mathematical terms, the optical access is a submatrix of the matrix associated to entire image. This submatrix is extracted by selecting the optical access area in the image (Figure 3.13)

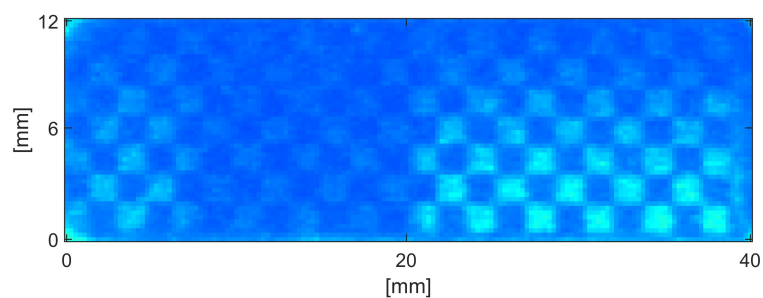


Figure 3.13: Image Framed

The case of the flame generated by the combustion process between methane and oxygen with 20 *bar* pressure and 2.2 *ROF* is considered for a result representation.

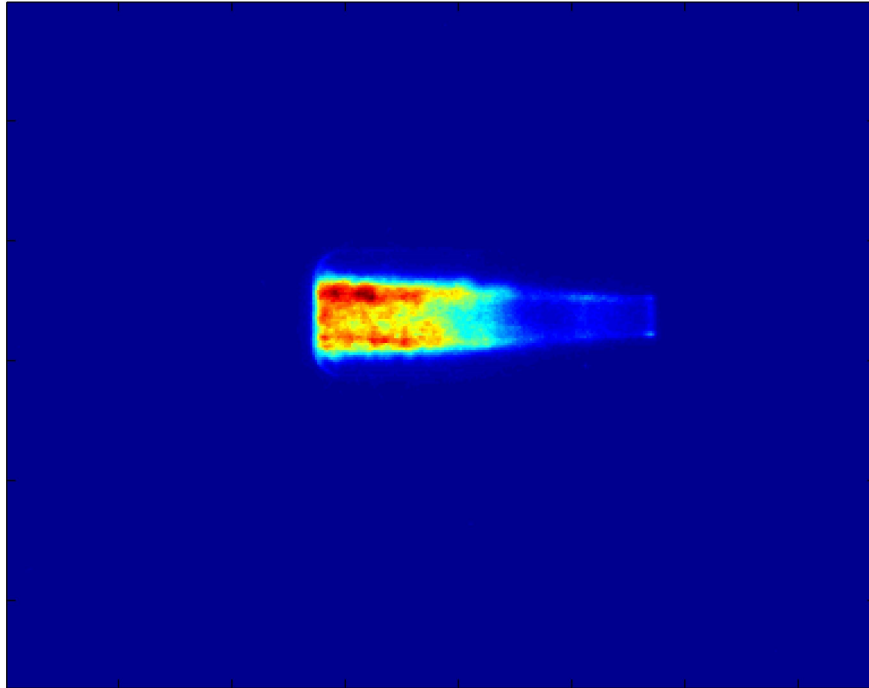


Figure 3.14: Case *methane/oxygen*, 20 *bar*, *ROF* 2.2, Average of the Entire Image

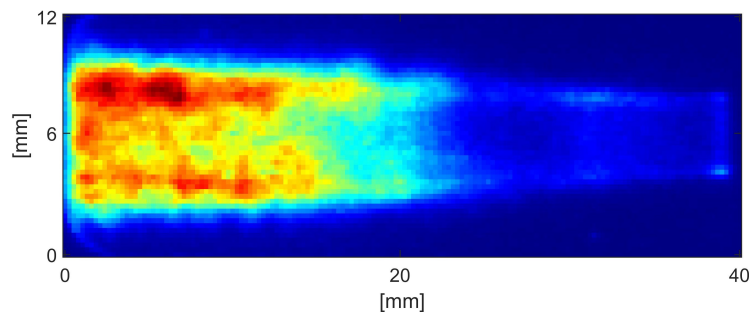


Figure 3.15: Case *methane/oxygen*, 20 *bar*, *ROF* 2.2, Image Framed

There is not a single image framing which is exactly identical to all cases; between one case and another the calibration before the test itself may be different from the previous one. Hence, this procedure is applied for each test individually.

However, the purpose of image windowed resizing is to eliminate the influence of the external hardware because it could lead to complications of the data analysis. In this way it is possible to obtain only the flame emission, avoiding reflections of light due to metallic material present in the hardware.

3.4 Workflow of MATLAB code

Although shading correction is part of the image pre-processing, brightness correction is applied after the image framing for simplicity.

The MATLAB code sequence is as follows:

1. Average Image
2. Angle Correction
3. Image Resizing
4. Shading Correction (Negligible)

Furthermore, in order to compare images with different pressure and ROF , the code normalizes the emission intensity of each case with respect to the maximum emission intensity obtained by considering all cases of different pressure and ROFs.

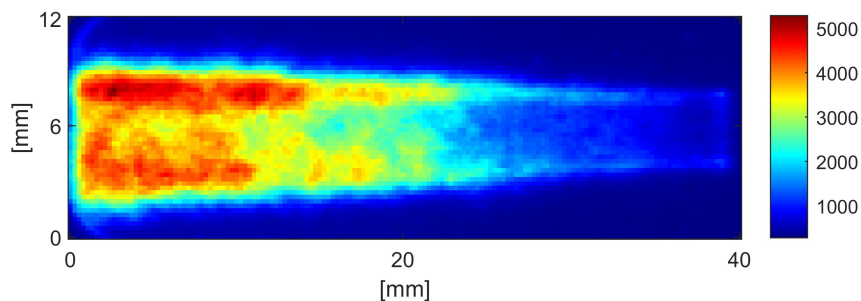


Figure 3.16: Emission Intensities

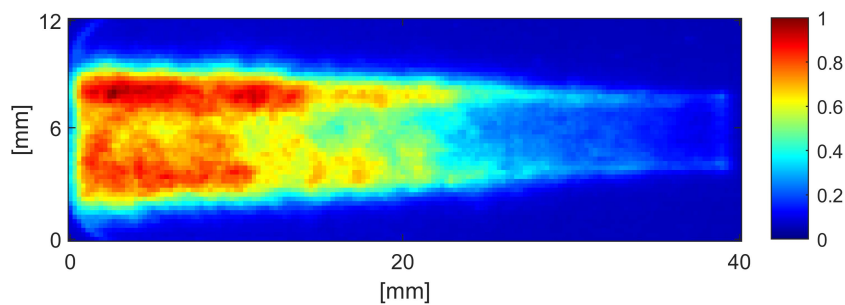


Figure 3.17: Emission Intensities Normalized

The reason why the colors of the image between Figure 3.16 and Figure 3.17 are not changed is due to the fact that this is the case in which the maximum value of emission intensity was considered (pressure 20 bar, *ROF* 2.6). The example was reported only for the purpose to show the normalization in the image processing, this is a process in which the range of pixel intensity values is changed, without modifyinh the proportionality between the intensity of one pixel and another.

All digital image processing steps will be applied to all test campaign cases and results will be shown in the next chapter.

Chapter 4

Test Results

4.1 Rocket Performance Results

4.1.1 Assumptions

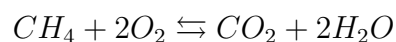
In the analysis of the current test campaign performance some assumptions have been considered.

4.1.1.1 Assumptions on the fluid

Homogeneous fluid In the case of solid propellants, the oxidant and the fuel are already mixed. In the current case there are no solid propellants, therefore, a proper injection of the propellants is necessary to ensure that the fluid is homogeneous. It is difficult to have a good mixing when liquid or gaseous propellants are used in a rocket.

Perfect gas γ is constant, particularly it does not depend on temperature. Furthermore, the perfect gas law is used for the density calculation.

Chemical equilibrium in combustion chamber The chemical reaction in the combustion chamber for this study case is:



For the calculation of the outlet gas velocity from the nozzle, the molar mass of gases produced by reaction is needed. It is assumed that the chemical equilibrium is reached and, therefore, there are no other intermediate chemical species produced. Another value

that one needs for the calculation of outlet velocity is the temperature reached in the combustion chamber. Data were plotted in the graph in the next page by using the software *NASA CEA2* in order to evaluate this temperature with respect to *ROF*:

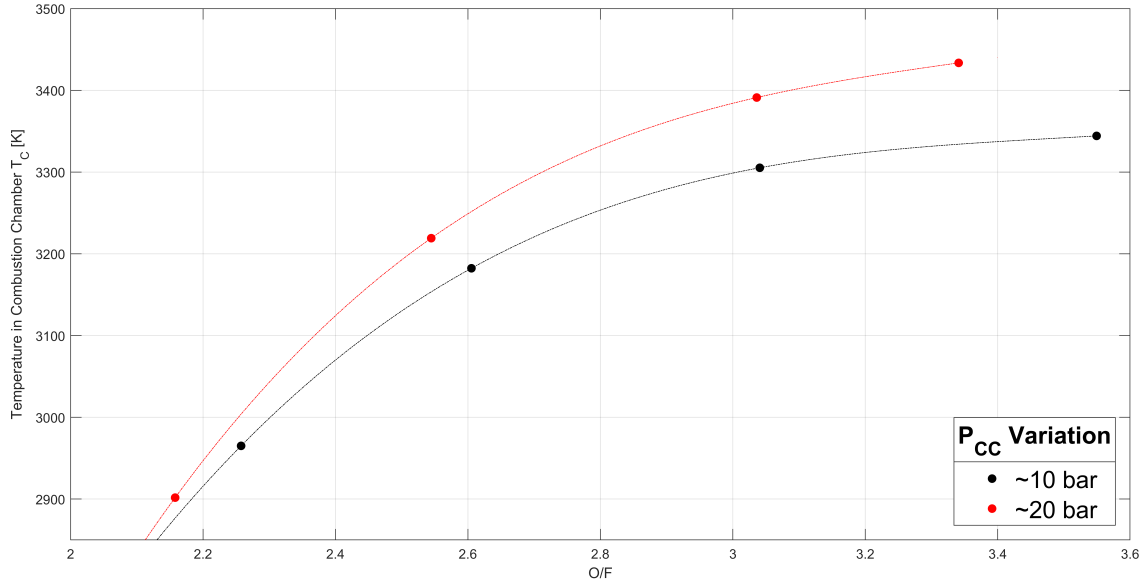


Figure 4.1: Combustion Chamber Temperature for Oxygen/Methane

Shifting equilibrium in the nozzle During the gases exit, different chemical equilibrium composition is considered in each section of the nozzle. In this case part of energy lost in dissociation is recovered.

4.1.1.2 Assumptions concerning transformation

Adiabatic transformation In reality there is a non-negligible thermal exchange: about 2% of available chemical energy is dispersed; this 2% of lost energy, however, has a small effect on performances. This assumption is, therefore, more than reasonable.

Absence of the effects of boundary layer In reality the boundary layer occupies a space, creates friction and also it affects heat exchanges.

4.1.2 Performance Indices Overview

It is possible to define some quantities which are characteristic for the rocket engine. They are useful to characterize the performance of a rocket, to compare theoretical and experimental results and, moreover, they can be used to interpret test results.

4.1.2.1 The thrust coefficient

The most important performance parameter of rocket engine is the thrust. If the diverting part of nozzle did not contribute to the thrust, the thrust delivered by the rocket engine in vacuum, F_0 , would be

$$F_0 = P_c A_t$$

If the diverting part of nozzle is present, the force generated for the pressure difference is optimized[19]. By making the ratio between the thrust F and the force F_0 , the thrust coefficient is obtained,

$$C_F = \frac{F}{F_0} = \frac{F}{P_c A_t} = \frac{\dot{m} u_e + A_e (P_e - P_0)}{P_c A_t}$$

which represents the ability of nozzle to amplify the thrust.

The exit velocity from the nozzle, u_e , can be obtained from the balance equation of the total enthalpy,

$$h_e^o = h_c^o$$

Neglecting the flow velocity inside the combustion chamber, therefore, it is possible to write:

$$u_e = \sqrt{\frac{2\gamma}{\gamma-1} T_c \frac{R}{M} \left(1 - \frac{P_e^{\frac{\gamma-1}{\gamma}}}{P_c^{\frac{\gamma-1}{\gamma}}}\right)}$$

Subsequently, by expressing the mass flow as a dimensionless mass flow and by introducing the area ratio $\epsilon = \frac{A_e}{A_t}$, C_F is expressed as:

$$C_F = \Gamma \sqrt{\frac{2\gamma}{\gamma-1} T_c \frac{R}{M} \left(1 - \frac{P_e^{\frac{\gamma-1}{\gamma}}}{P_c^{\frac{\gamma-1}{\gamma}}}\right)} + \epsilon \left(\frac{P_e}{P_c} - \frac{P_0}{P_c}\right)$$

C_F depends on γ , $\frac{P_e}{P_c}$, ϵ , $\frac{P_0}{P_c}$; however, the geometric ratio $\epsilon = f(\gamma, \frac{P_e}{P_c})$, therefore, independent parameters are only three:

$$C_F = f\left(\gamma, \epsilon, \frac{P_0}{P_c}\right)$$

Hence, the thrust coefficient depends on the chemistry, the shape of the nozzle and the altitude (in a vacuum $P_0 = 0$)[19]. Furthermore, the effect of γ is weak compared to the other two parameters, hence, it is assumed constant.

4.1.2.2 The characteristic velocity

The characteristic velocity is defined as $c^* = \frac{P_c A_t}{\dot{m}}$. It is essentially independent of nozzle characteristics and it is related to the efficiency of the combustion[19] which is assumed equal to 1 for the calculation of the load points of the current test campaign.

It is important to observe how this quantity is inversely linked to the consumption required to maintain the pressure P_c at a certain level, hence it is useful to have a high value of c^* . By replacing the expression of the mass flow with the dimensionless mass flow, another formulation of the characteristic velocity is obtained:

$$c^* = \frac{\sqrt{\frac{R}{M} T_c}}{\Gamma}$$

This parameter is, therefore, a function of γ , temperature T_c and molar mass M .

4.1.2.3 The effective exhaust velocity

Multiplying the thrust coefficient with the characteristic velocity, the effective exhaust velocity is obtained, indeed

$$C_F c^* = \frac{F}{\dot{m}} = u_e + \frac{A_e(P_e - P_0)}{\dot{m}} = c$$

It represents the ability to amplify the thrust with the nozzle related to consumption to maintain the constant pressure inside the combustion chamber[19].

From the formulation it is possible to understand that the effective exhaust velocity depends on atmospheric pressure and therefore is not constant during a rocket's ascent.

4.1.2.4 Total and specific impulse

A rocket engine, which during a time interval, t_b , employs a thrust, $F(t)$, delivers a total impulse

$$I_t = \int_0^{t_b} F(t) dt.$$

The propellant mass which was needed for this is M_p and hence, the impulse per unit weight of the propellant, the *specific impulse* I_{sp} is

$$I_{sp} = \frac{\int_0^{t_b} F(t) dt}{M_p g_0} = \frac{\int_0^{t_b} F(t) dt}{\int_0^{t_b} g_0 m(t) dt}$$

Considering the average values of the total impulse and the mass of the propellant, the formulation of the specific impulse can be written as

$$I_{sp} = \frac{\tilde{I}_t}{g_0 \tilde{M}_p}$$

Considering the constant thrust or a time interval so small that it is possible to consider the constant thrust, the specific impulse can be expressed as

$$I_{sp} = \frac{c}{g_0}$$

This quantity shows how much impulse can be obtained from a unit weight of propellant, and as one tries to keep weights as low as possible in rocket technology, it is evident that a high specific impulse is desirable[19]. In addition, the specific impulse may also be interpreted as the time during which a propellant can deliver a force which equals the propellants' initial weight.

4.1.2.5 The volumetric specific impulse

The effective exhaust velocity basically represents the amount of propellant that one must use to have a certain level of thrust but it does not say how much volume this propellant occupies. It may be interesting to calculate the volume of tanks containing the propellant in order to have a certain boost per unit of time.

Usually not just a single propellant is used, but mixtures; the density must therefore take into account both the oxidant and the fuel.

The *bulk density* is expressed as

$$\rho = \frac{\rho_O \rho_F (1 + ROF)}{ROF \rho_F + \rho_O}$$

Therefore, the volumetric specific impulse is defined as

$$I_\rho = I_{sp} \rho$$

For the design of rocket this parameter is very important because it takes in account mainly the size of tanks, hence the structural mass of rocket: more structural mass one has, higher is the fuel consumption and less payload one can bring on board.

4.1.3 Combustion Chamber Processes Overview

The injection process is only the first in a series of processes that lead to combustion of the propellants. The injectors geometry has a dominant role in the injection velocities of the propellants, which in turn control the aerodynamic forces that first break up and consecutively atomize the liquid oxygen jet to form a spray of small droplets. After spray formation, the small droplets will start to vaporize, and the oxygen gas will then mix with the fuel to a combustible mixture to allow the chemical reaction to take place. Atomization is the process following injection and it can be divided into two main sub-processes. Primary breakup is controlled by the velocity difference between the liquid core and the annular jet. Aerodynamic shear forces, due to the velocity difference, cause the liquid jet to become unstable, and start tearing off large segments of liquid. These so-called ligaments are then subject not only to aerodynamic forces, but internal hydrodynamic forces in the liquid play a larger role as well. The combination of these forces results in the secondary breakup of the ligaments to form the droplets in the fully developed spray[20]. Therefore, atomization characterizing dimensionless numbers such as the velocity ratio VR and the momentum flux ratio J take into account the relative motion of the two fluids. Both the velocity ratio and the momentum flux ratio are based on propellant temperatures and pressure at injection conditions. These two parameters can be written as follows:

$$VR = \frac{u_{fuel}}{u_{ox}} \quad (4.1)$$

$$J = \frac{(\rho u^2)_{fuel}}{(\rho u^2)_{ox}} \quad (4.2)$$

After injection, the liquid starts to vaporize, but not until the small droplets are formed, vaporization becomes the dominant process and this processes depends from the size of the droplets. A large droplet can evaporate quicker due to its large surface, which in turn accelerates the heating of the droplet, while if a droplet is small, it will heat up quicker but will therefore also shift the equilibrium of the droplet such that evaporation accelerates[20]. Subsequently, after the vaporization, the propellants can start to mix. The mixing process is also improved when the convective motion carries newly formed gas into the mixing zone. When a mixture develops where a chemical reaction can be sustained, the local chemical reaction will then combine with the other regions to build a flame. When in the combustion chamber the propellants are sufficiently mixed and the temperature reaches a certain value, they will chemically react. If enough mixing takes place due to injection/atomization and mass flow is sustained, enough reactions will take place to build a flame. The ignition process is usually guaranteed by a spark that initiates the creation

of a flame. The volume of the combustion chamber will contain a heterogeneous mixture of liquid propellants, mixed but un-burnt gases and hot combustion products. With this heterogeneity obviously comes a nonuniform distribution of temperature (hence speed of sound), pressure and other properties. It is important to underline that the combustion process is not stationary. It depends on injection, atomization, vaporization and mixing. Some of these processes are more stochastic than others, thus combustion is, at least partially, a stochastic process as well[20].

4.1.4 Results

The graphs below show the results obtained from the methane/oxygen test campaign. Experimental data were acquired using thermocouples and pressure transducers located along the combustion chamber axis. Subsequently, through a MATLAB code, these data were used for the calculation of performance parameters.

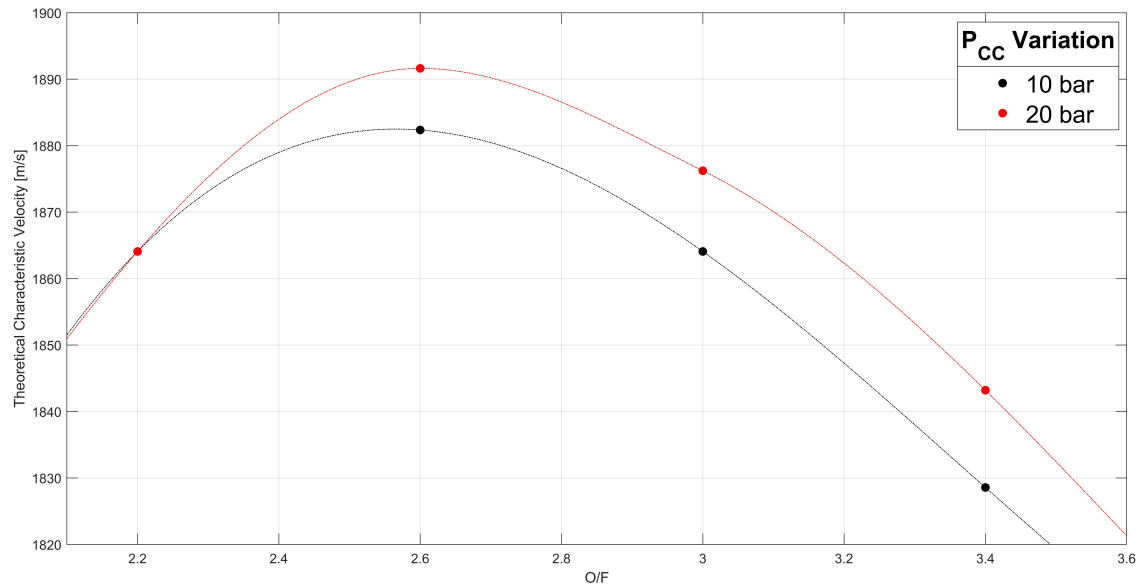


Figure 4.2: Theoretical Characteristic Velocity

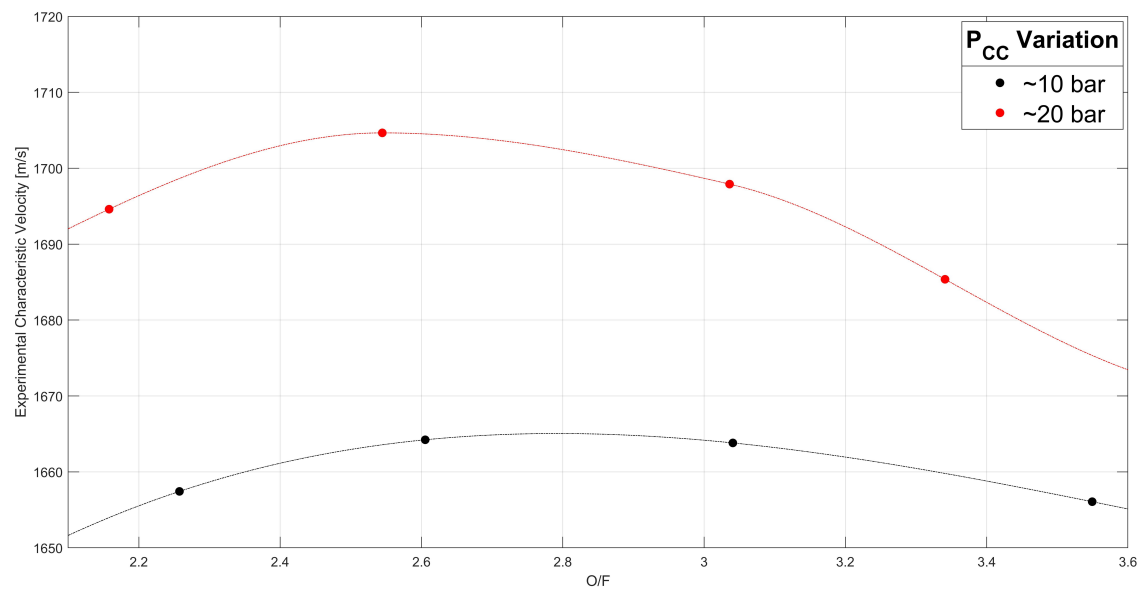


Figure 4.3: Experimental Characteristic Velocity

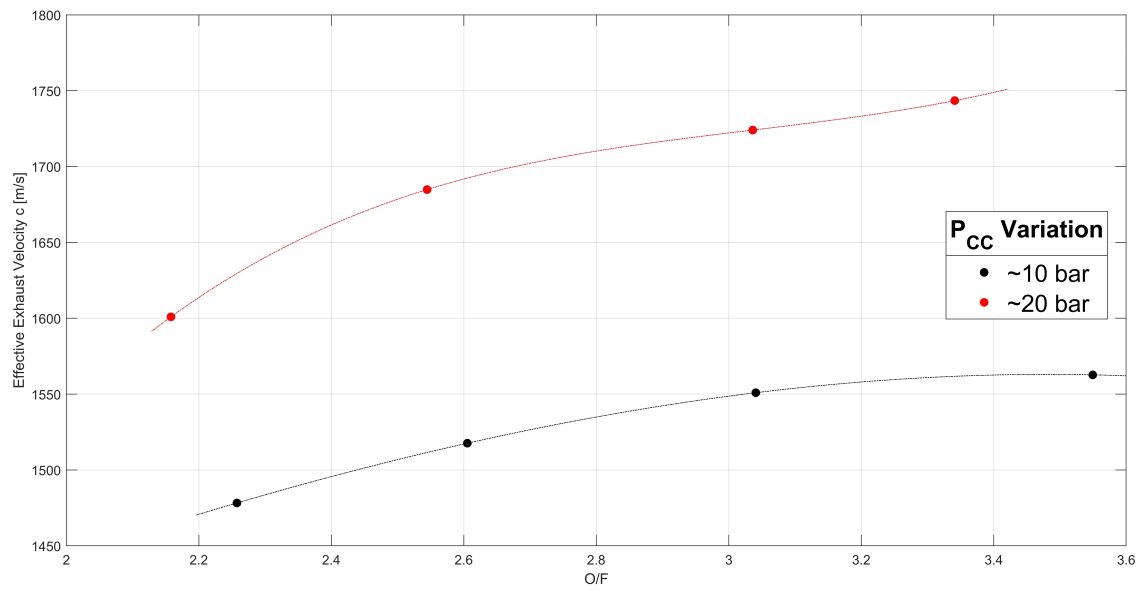


Figure 4.4: Experimental Exhaust Velocity c

Since the nozzle is adapted, the effective exhaust velocity is equal to the exit velocity from the nozzle. The maximum of this velocity obtained in the current test campaign was reached for $ROF = 3.4$ value (Figure 4.4), and hence for the highest combustion temperature reached in both P_c cases.

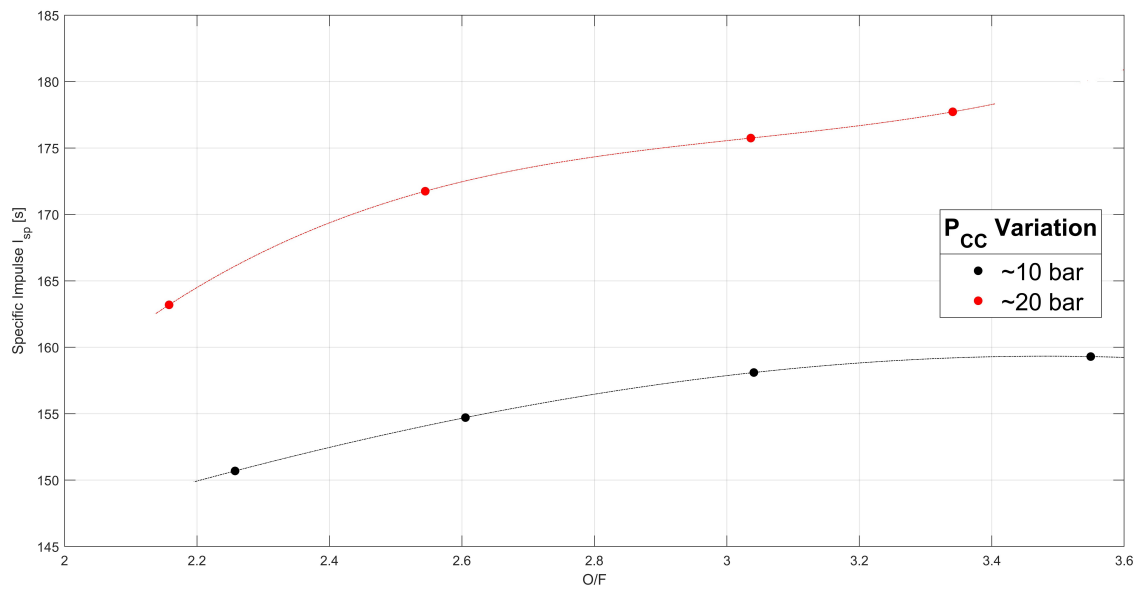


Figure 4.5: Experimental Specific Impulse I_{sp}

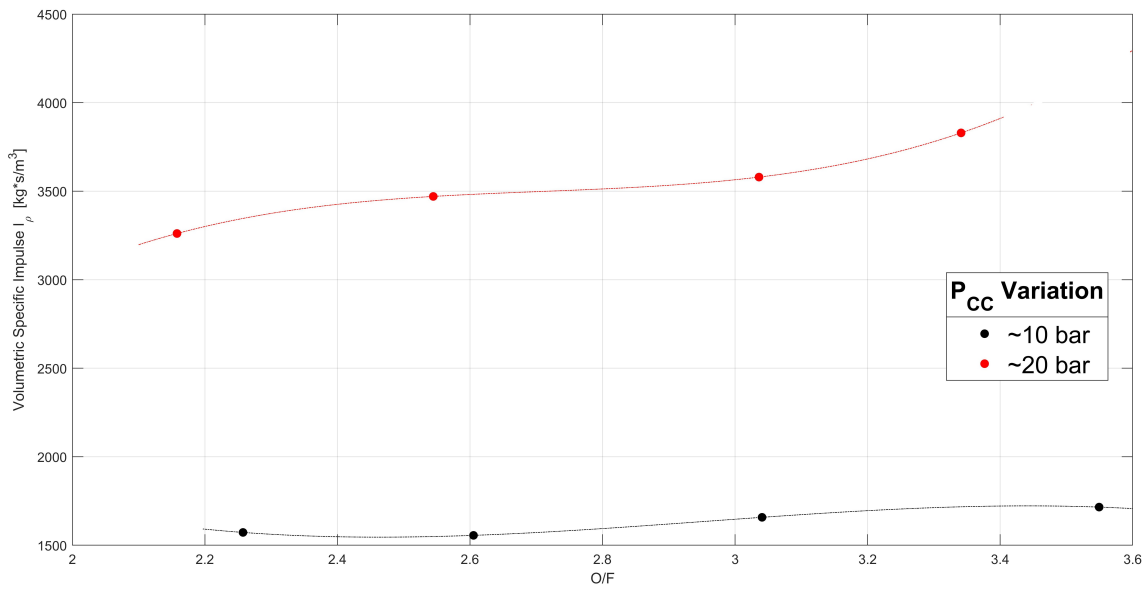


Figure 4.6: Experimental Volumetric Specific Impulse I_ρ

The ratio of oxygen density ($1.429 \frac{kg}{m^3}$) and methane density ($0.656 \frac{kg}{m^3}$), such as $\frac{\rho_{O_2}}{\rho_{CH_4}} = 2.168$, underlines the importance of the weight of the tanks: it is not only important the mass of propellant consumed, but also the volume to contain this propellant. Hence, if one uses more oxygen the volume used decreases. The maximum of the volumetric specific impulse obtained in the current test campaign is for $ROF = 3.4$ (Figure 4.6).

If one considers the ratio of oxygen density and hydrogen density ($0,0899 \frac{kg}{m^3}$), such as $\frac{\rho_{O_2}}{\rho_{H_2}} = 15.895$, the importance of the weight of tanks becomes more relevant, indeed, for the hydrogen/oxygen, one has a different I_ρ trend. The graph below shows I_ρ and c trend:

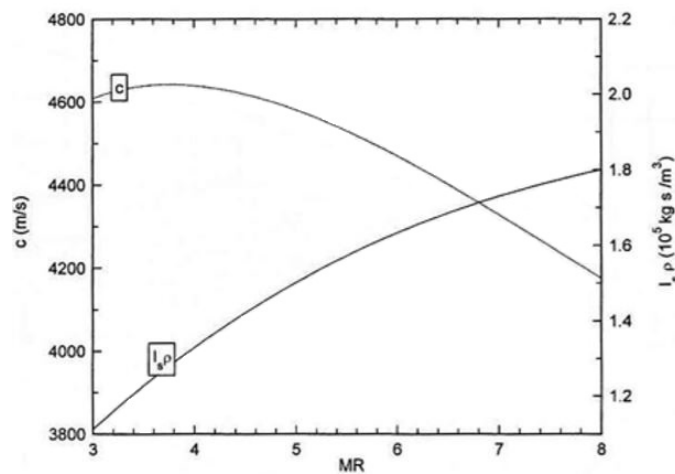


Figure 4.7: Volumetric Specific Impulse I_ρ and Exhaust Velocity c for Hydrogen/Oxygen

In most cases the mass to be transported in flight is:

$$M_{TOTAL} = M_{PROPULSOR} + M_{PROPELLANT} + M_{TANK}$$

One needs to minimize the sum of masses in order to transport more payload mass. Hence, in the case of hydrogen/oxygen, one could reduce c by accepting to consume more fuel in order to reduce considerably the mass of tanks. The same graph is shown below but for methane/oxygen case of current test campaign,

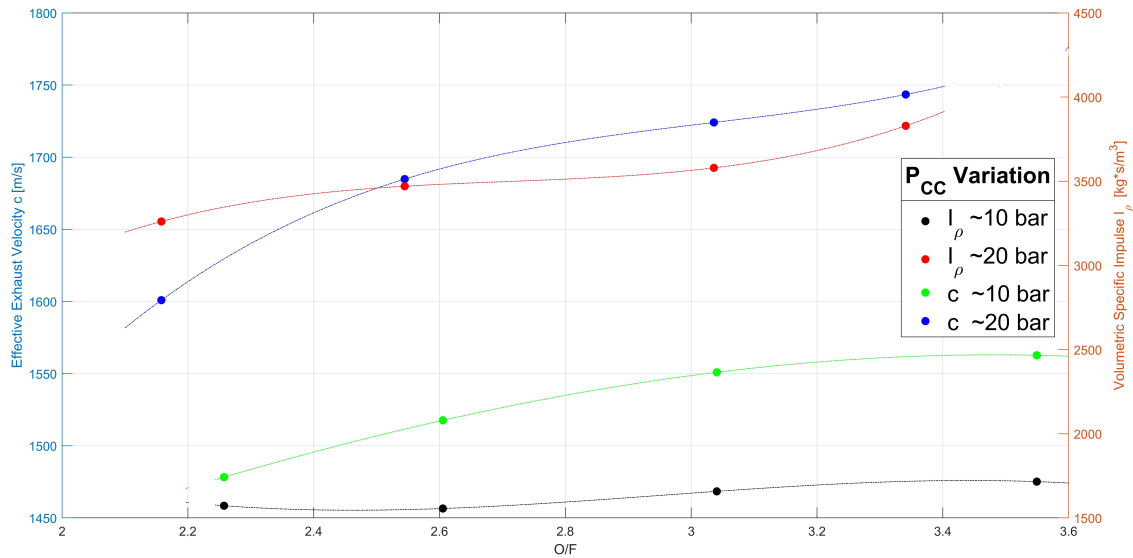


Figure 4.8: Volumetric Specific Impulse I_{ρ} and Exhaust Velocity c for Methane/Oxygen

It is possible to note that the maximum of exhaust velocity corresponds to the maximum of volumetric specific impulse, for 10 *bar* and 20 *bar*. Hence, increasing *ROF*, not only performances grow up, but the volume of tanks that one has to be transported in flight is reduced. This could be one of advantages of propellants combination methane/oxygen. Concerning the theoretical characteristic velocity (Figure 4.2), it is obtained considering the nominal values of pressure in combustion chamber and mass flow rates supplied by *NASA CEA2* software, while the experimental characteristic velocity (Figure 4.3) is obtained considering the measured of pressure in the combustion chamber and mass flow rates detected during the test campaign. Both velocities show a similar trend, whose maximum of the function is reached at $ROF = 2.6$. If one makes the ratio between the experimental characteristic velocity and the theoretical characteristic velocity, the combustion efficiency is obtained

$$\eta_C = \frac{c_{exp}^*}{c_{theo}^*}$$

The combustion efficiency for chemical rockets can be seen also as the ratio of real and ideal heat of reaction per unit of propellant and it is a measure of the source efficiency for creating energy. Its value is high, approximately from 94% to 99%, hence, the combustion is essentially complete. Furthermore, in liquid propellant rocket thrust chambers, this coefficient depends on injection method and mixing quality and it increases with combustion temperature growth. The next figure shows the trend of combustion efficiency when the ROF varies, for 10 *bar* and 20 *bar* pressure cases

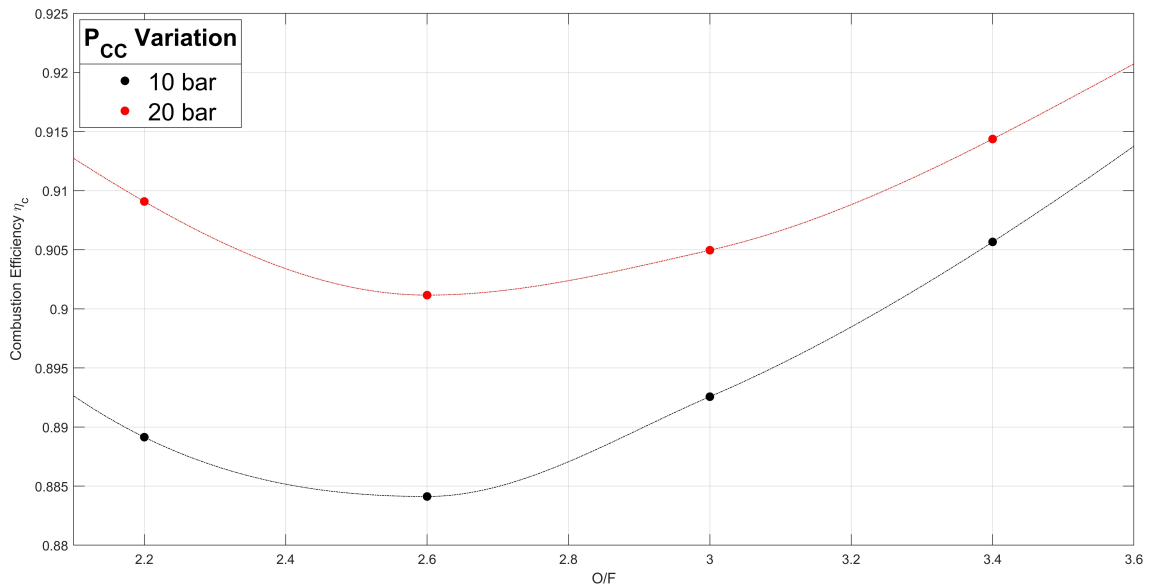


Figure 4.9: Combustion efficiency η_c

As mentioned before, the combustion efficiency increases with combustion temperature growth. Indeed, η_c trends, for 10 *bar* and 20 *bar*, are similar but with different level and this result is due to the fact that in the second case, 20 *bar*, since the pressure in the combustion chamber is higher, the temperature is higher and, therefore, the combustion efficiency is greater. Furthermore, the combustion efficiency grows up when mixture ratio increases. This growth leads to a higher combustion temperature due to the fact it is near the stoichiometric condition (4). Finally, for I_{sp} trend (Figure 4.5) the maximum value is reached for high mixture ratio, near the stoichiometric condition.

Since the same injector is used for all cases, the O/F ratio prescribes a velocity ratio and the Figure 4.10 shows how VR changes:

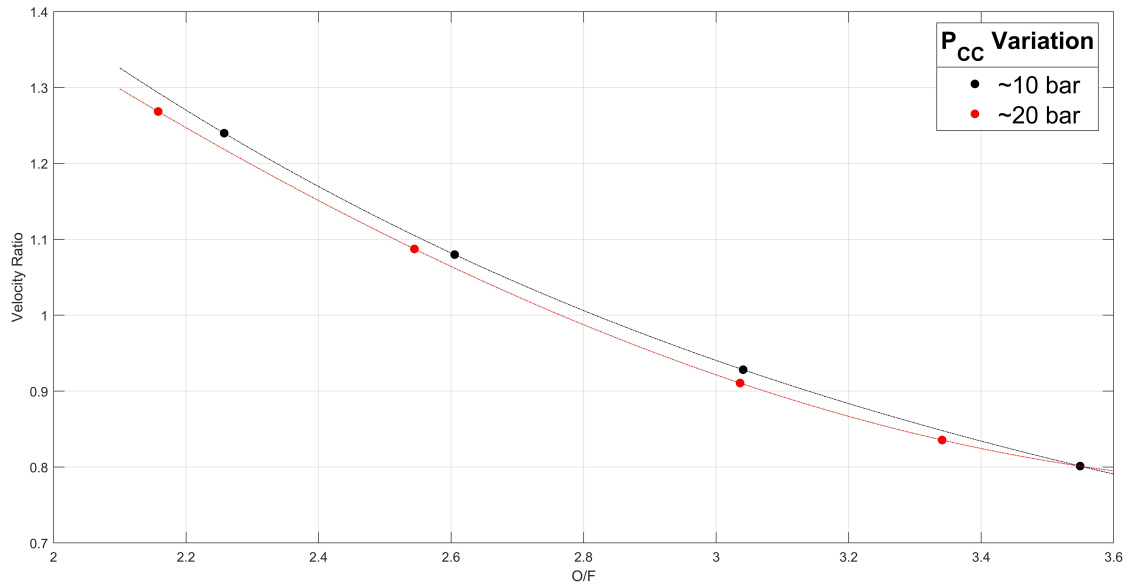


Figure 4.10: Velocity ratio VR

When the velocity ratio is high, it means that the difference between the mass flow rate of methane and oxygen is high. For this reason, the shear forces at propellant flows interface increase and they allow mixing to be more efficient. Indeed, for $ROF \simeq 2.2$, the combustion efficiency is higher because the velocity ratio is higher. In opposition, when $ROF \simeq 2.6$ and $ROF \simeq 3.0$ are obtained, the combustion efficiency is lower because the velocity ratio is lower. It is very useful to observe that, for $ROF \simeq 3.0$, the combustion efficiency is a little bit higher than $ROF \simeq 2.6$ case, even if the velocity ratio is lower. One could say the same for $ROF \simeq 3.4$. The answer to these results is that after a certain ROF value, the combustion efficiency trend is more influenced by temperature in the combustion chamber (ROF value is more close to the stoichiometric ratio) than by velocity ratio.

The next figure (4.11) shows the trend of moment flux ratio with different ROF .

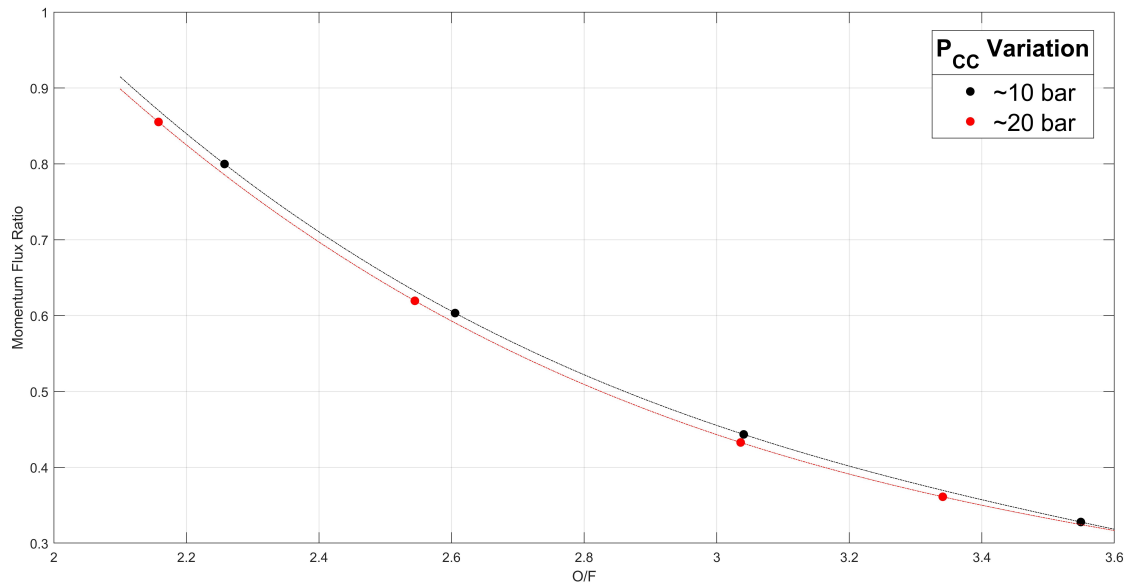


Figure 4.11: Momentum flux ratio J

From the graph it is possible to note that the momentum flux ratio trend is similar to the velocity ratio and, as the velocity ratio, also the momentum flux ratio is based on propellant temperatures and pressure at injection conditions.

The reason why VR and J have the same trend is that they are strongly related to each other within the corresponding operating conditions through the injection area ratio AR and the mixture ratio ROF [21]:

$$\frac{VR}{J} = AR \cdot ROF$$

However, in current test campaign the AR was constant, hence VR and J depend only on ROF .

4.2 Image Processing Results

In the current paragraph the results obtained from the image processing will be shown. It is useful to remember that the color scale was normalized with the maximum emission intensity captured by the ICCD camera (5289). This maximum value was reached in the $P_c = 20 \text{ bar}$ and $ROF 2.6$ case, as shown in Figure 4.12:

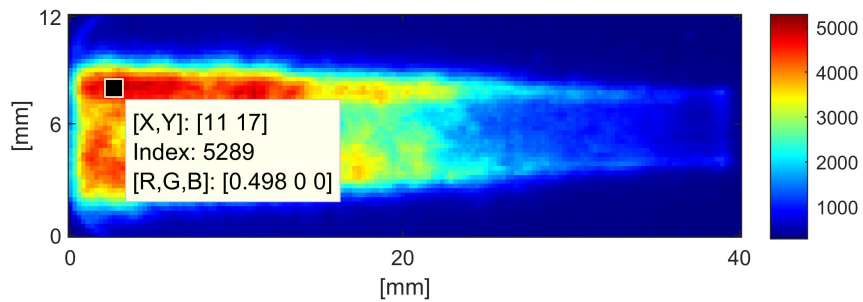


Figure 4.12: Maximum pixel intensity value captured by ICCD camera

To understand how the flame emission change with the variation of pressure and mixture ratio in combustion chamber, the mean emission intensity along axial direction will be shown.

In the following pictures it is useful to specify that the coaxial injector is placed on the right, hence, propellants are injected from right to left.

$P_{CC} = 10 \text{ bar}$, ROF variation:

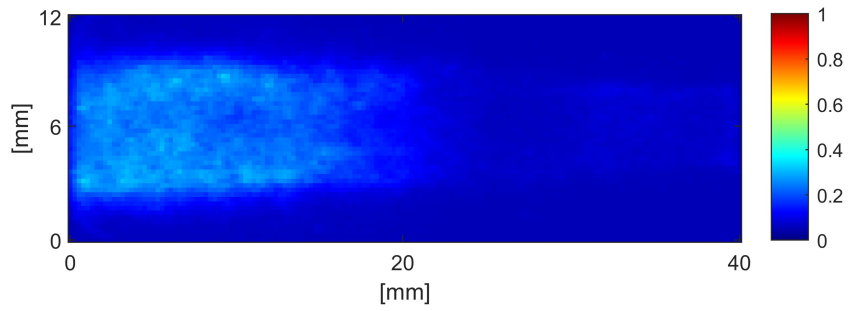


Figure 4.13: Case 10 bar, ROF 2.2

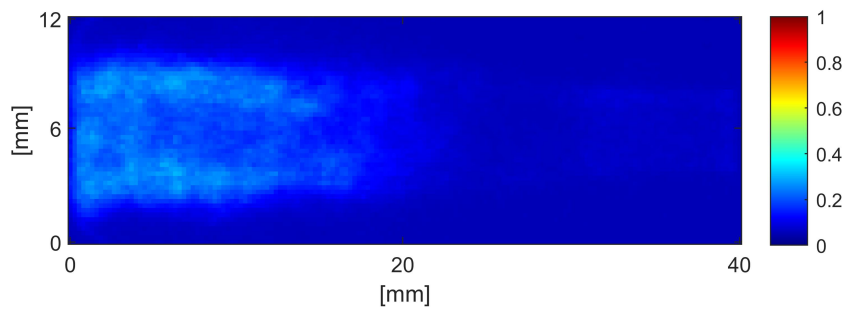


Figure 4.14: Case 10 bar, ROF 2.6

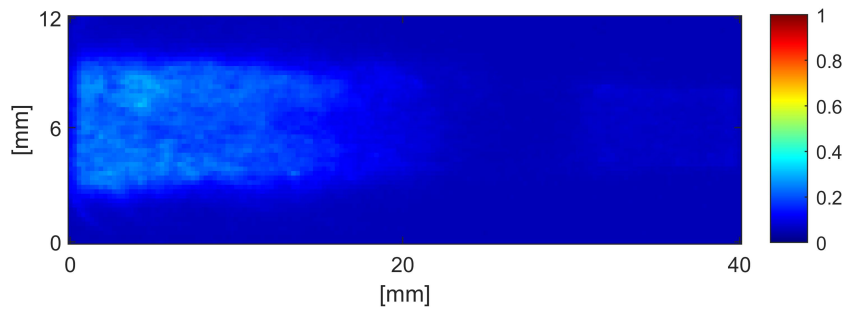


Figure 4.15: Case 10 bar, ROF 3.0

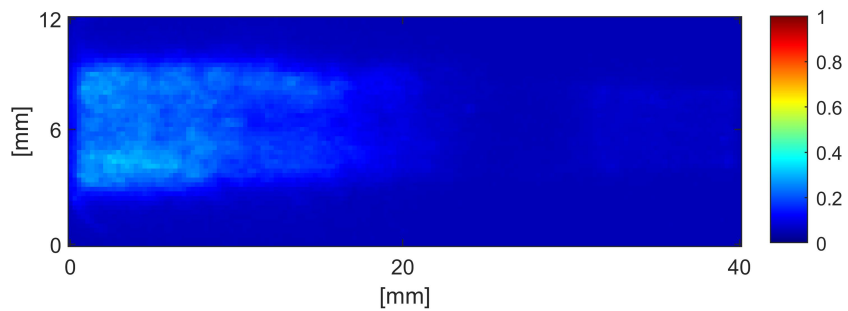


Figure 4.16: Case 10 bar, ROF 3.4

$P_{CC} = 20 \text{ bar}$, ROF variation:

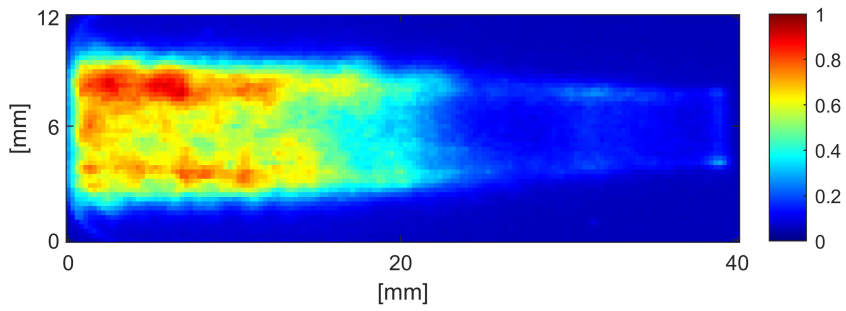


Figure 4.17: Case 20 bar, ROF 2.2

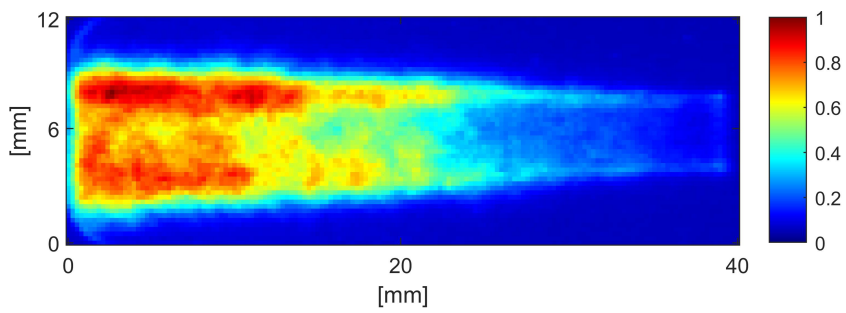


Figure 4.18: Case 20 bar, ROF 2.6

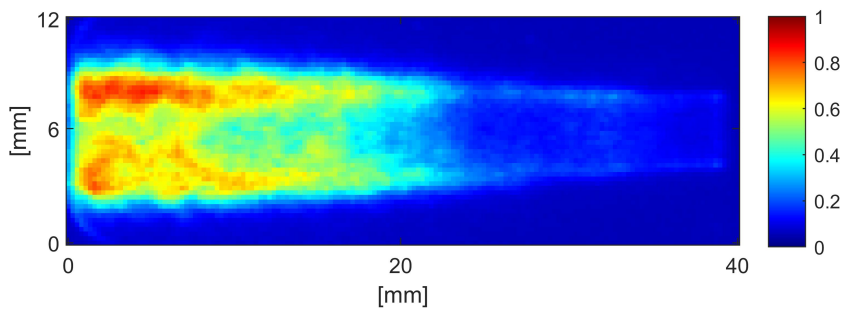


Figure 4.19: Case 20 bar, ROF 3.0

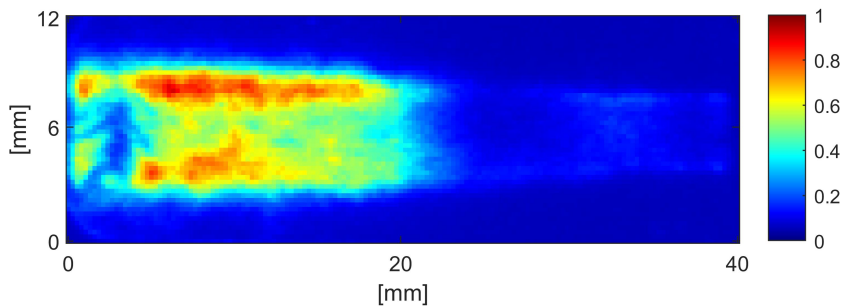


Figure 4.20: Case 20 bar, ROF 3.4

If one considers that the ROF is constant, an increase of the chamber pressure, from 10 to 20 bar, comes along with an increase of momentum flux ratio, which in turn increases the OH^* emission intensity. Indeed, the next graphs show how the emission increases with the combustion chamber pressure

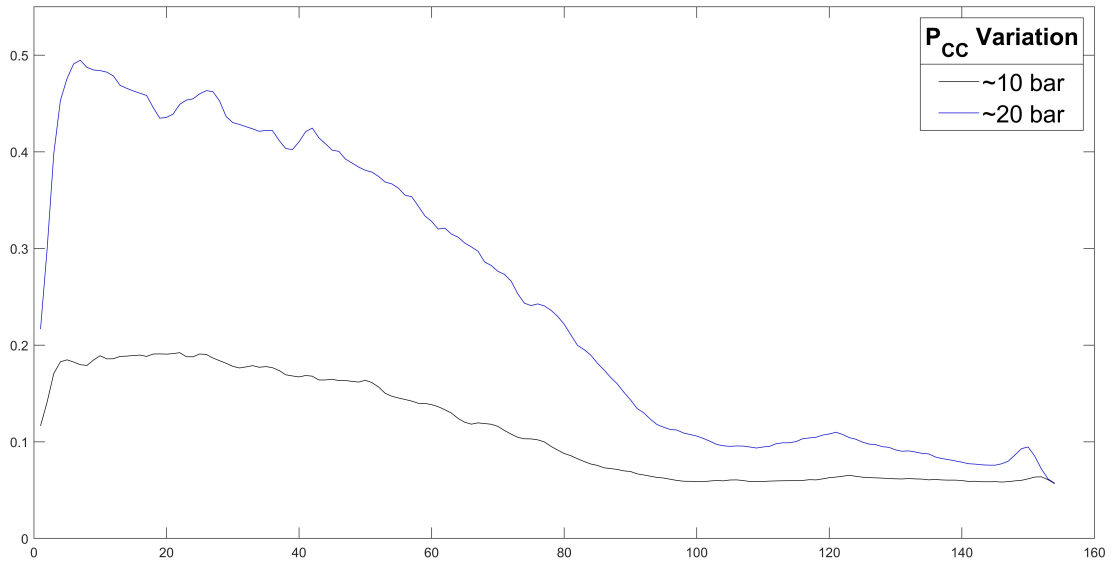


Figure 4.21: Mean Emission Intensity along axial direction as a function of P_{CC} for ROF 2.2

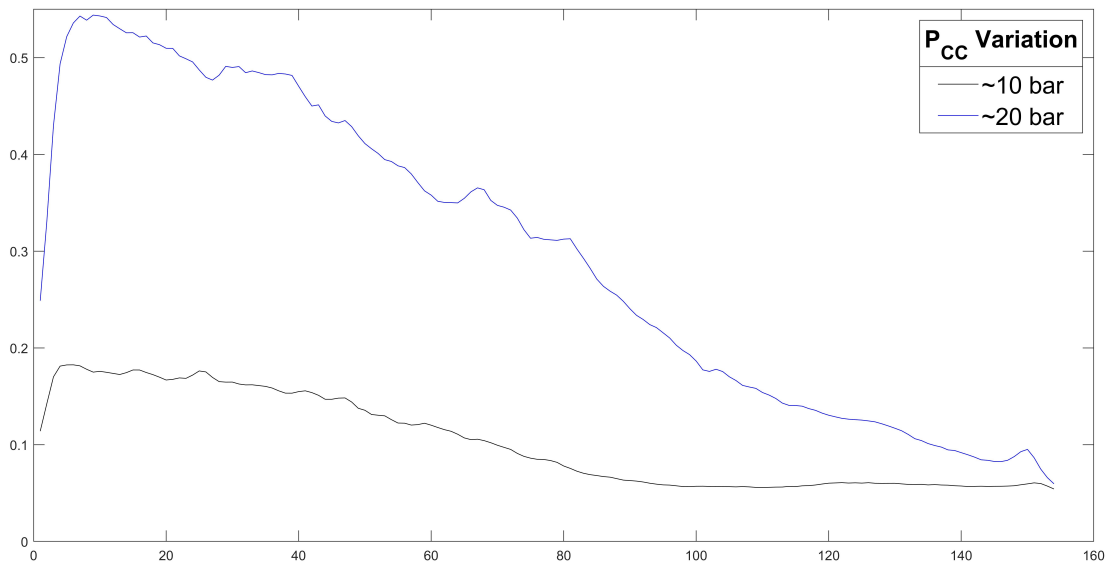


Figure 4.22: Mean Emission Intensity along axial direction as a function of P_{CC} for ROF 2.6

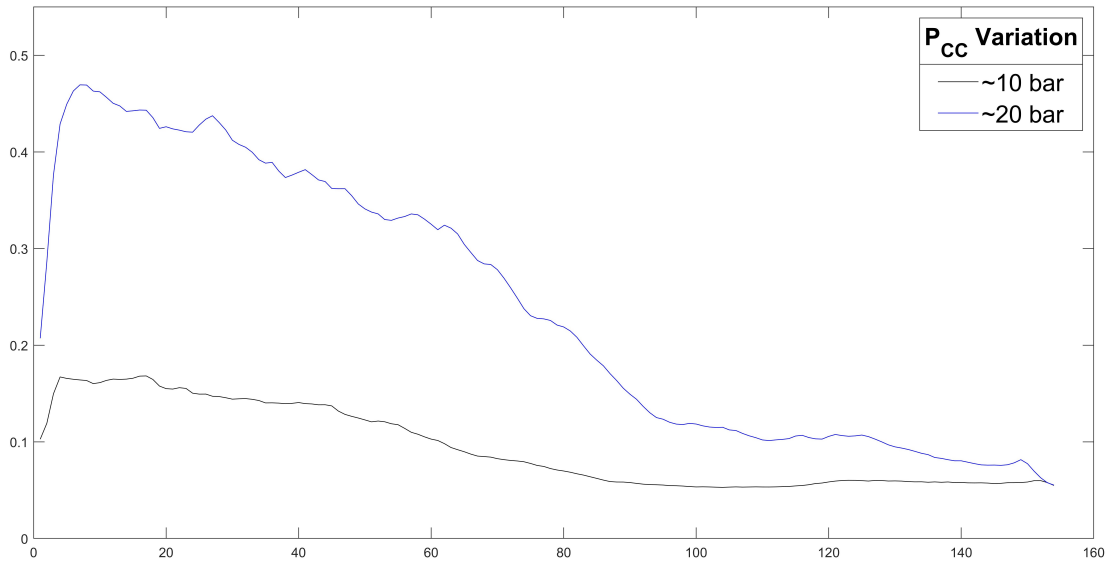


Figure 4.23: Mean Emission Intensity along axial direction as a function of P_{CC} for ROF 3.0

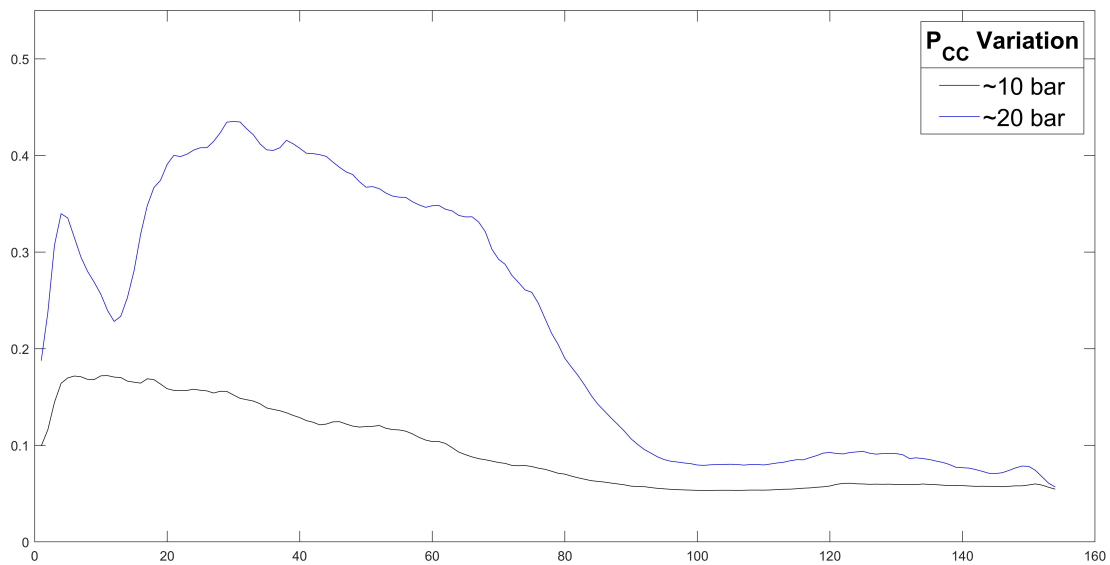


Figure 4.24: Mean Emission Intensity along axial direction as a function of P_{CC} for ROF 3.4

It is evident that the relative emission intensity strongly relates to the combustion chamber pressure: one can note that from 10 to 20 *bar* the OH^* emission is increased by about $\sim 60\%$ for all ROF cases.

On the other hand, if the pressure in combustion chamber is constant, one can observe that the highest value of VR and J is present for the lowest ROF value. It means that the difference of methane and oxygen gaseous velocity is the highest ($VR > 1$), the shear forces are higher and, hence, the propellants are better mixed. Therefore, for $P_C = 10$ *bar*,

the OH^* emission intensity is the highest for $ROF = 2.2$ (Figure 4.25). One can expected the same for the $P_C = 20 \text{ bar}$ case but experimentally, from the graph in Figure 4.26, the OH^* emission intensity is not the highest for $ROF = 2.2$. This is due to the fact that the test $P_C = 20 \text{ bar}$ with $ROF = 2.2$ was done with too much soot on the optical window which has reduced the OH^* emission intensity. It would be useful to repeat the 20 bar test campaign in order to confirm this hypothesis.

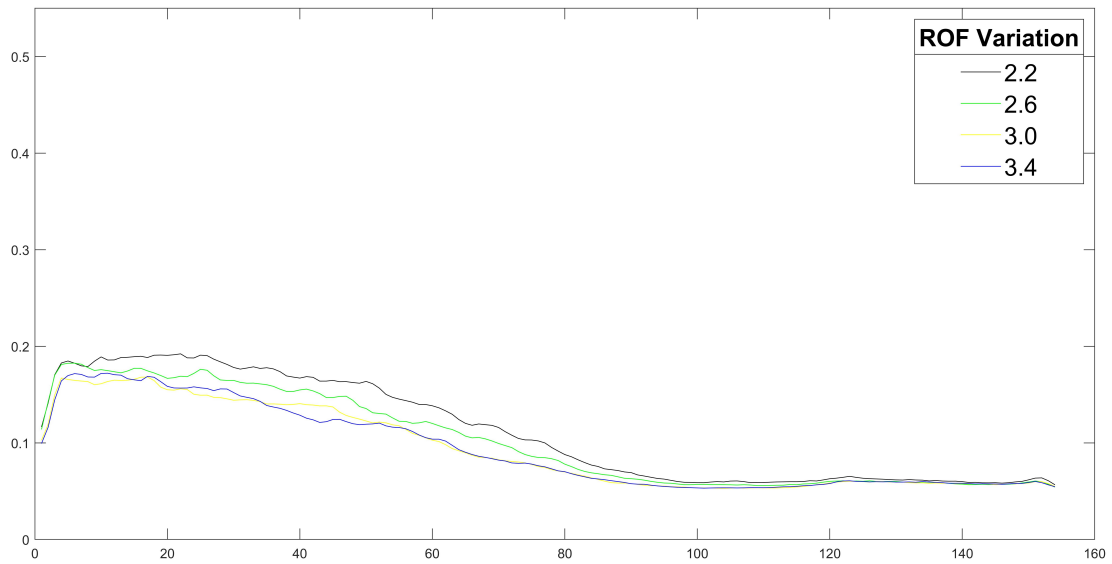


Figure 4.25: Mean Emission Intensity along axial direction as a function for ROF 2.2, 2.6, 3.0 and 3.4 at 10 bar

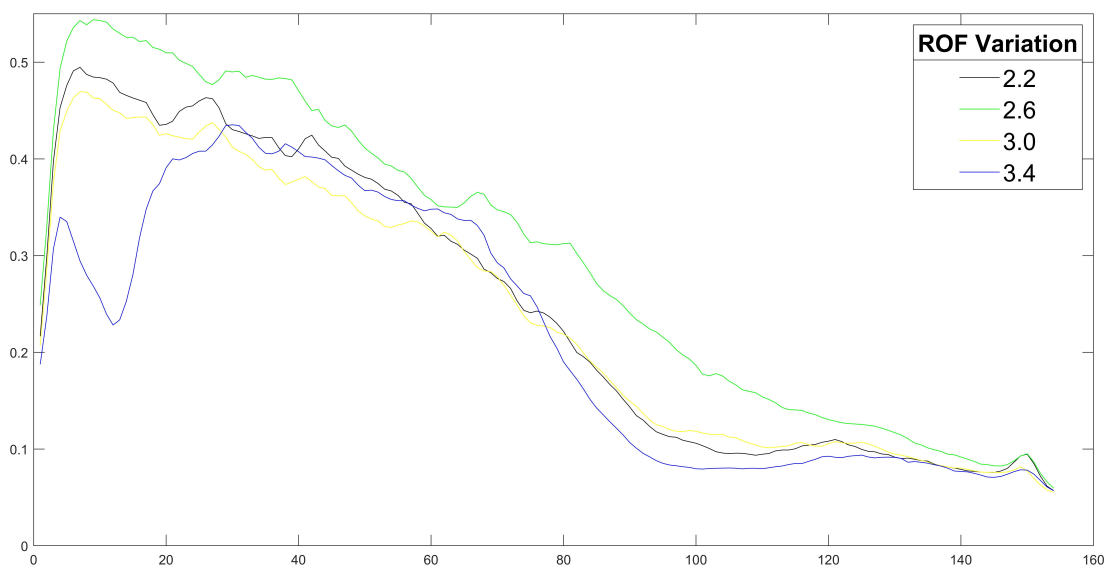
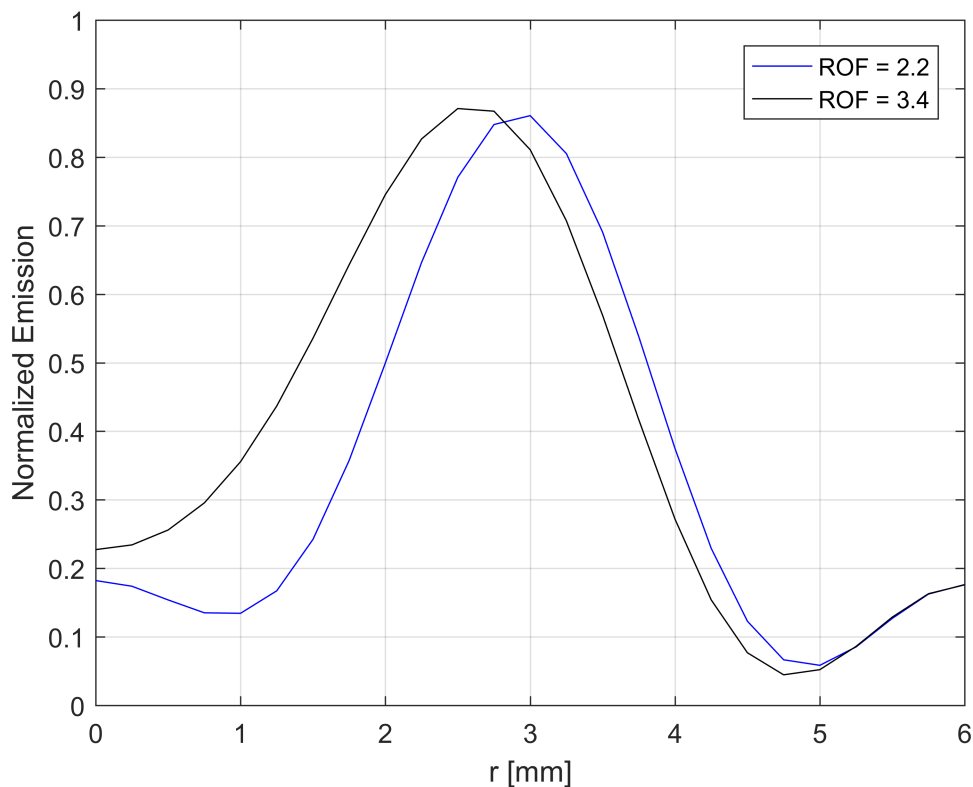


Figure 4.26: Mean Emission Intensity along axial direction as a function for ROF 2.2, 2.6, 3.0 and 3.4 at 20 bar

Furthermore, from the image processing results it is interesting to note how the width of flame changes with VR variation. For VR s greater than one, the gaseous methane velocity is higher than the gaseous oxygen velocity: in this case the shear forces tend to increase the spreading angle because the annular CH_4 jet is pulled outward by the slower GO_2 jet, thereby decreasing the distance of the flame front from the wall. For $ROF = 2.2$ the gaseous methane velocity is the fastest and hence the width of the flame is the highest and it tends to decrease by increasing the ROF . From the value of ROF for which VR s is less than one, it means that the velocity of the gaseous oxygen is greater than the velocity of the gaseous methane. This implies that the annular CH_4 jet is pulled inward by the faster GO_2 jet due to shear forces, thereby increasing the distance of the flame front from the wall and reducing the spreading angle of the flame[22]. It is interesting to visualize the change of width of the flame considering the radial profile of the flame at the same axial distance (30 mm from the injector) for minimum and maximum ROF at 20 bar pressure in combustion chamber :

Figure 4.27: Radial Profile of Flame at 20 bar [23]



r is the radius of the flame in which 0 corresponds to the center of the flame. Therefore 6 mm is the distance between the center of the flame and the combustion chamber wall. For $r = 6$ mm one has a certain value of flame emission due to the fact that the metallic material of combustion chamber has reflected the light of the flame and, hence, the MATLAB code has considered emissions which, in reality, are fictitious.

Chapter 5

Conclusions

On the current test campaign a study on performance and emission imaging was carried out. Performance parameters were calculated from experimental thermodynamic data obtained in the test facility by standard measurement techniques (termocouples and pressure sensors), while flame images were acquired by an ICCD camera, in order to illustrate the flame general structure and the emission changes by velocity and momentum flux ratio variations. The tests were carried out at 10 *bar* and 20 *bar* combustion chamber pressure and mixture ratio ranging from 2.2 to 3.4, with 0.4 steps. It has been observed that a 150s – 160s specific impulse has been achieved for $P_C = 10$ *bar* tests, while, for $P_C = 20$ *bar* tests, 162s – 178s values have been reached. Hence, specific impulse showed to increase with pressure and mixture ratio growth. It is important to underline that the maximum effective exhaust velocity and, therefore, the maximum specific impulse, do not coincide with characteristic velocity maximum ($ROF = 2.6$ for both 10 *bar* and 20 *bar* P_C cases), hence, to reach higher specific impulse values, it is needed to consume more propellant because of characteristic velocity inverse proportionality to consumption. Furthermore, unlike the hydrogen and oxygen combustion case, for methane and oxygen combustion it is shown that, when effective exhaust velocity increases, specific volumetric impulse increases too, which means an advantage in terms of tank mass to be carried in flight.

Concerning emission imaging, it is remarkable that the best mixing is reached at $P_C = 20$ *bar* and $ROF = 2.6$ case, because of maximum intensity reached. In reality, at $ROF = 2.2$ and $P_C = 20$ *bar*, the velocity ratio has shown to be greater than velocity ratio at $ROF = 2.6$ and $P_C = 20$ *bar*, even if an higher emission for $ROF = 2.2$ case was expected, due to higher shear forces generated between propellant flows (maximum VR). This discrepancy could be justified to soot accumulation, which decreased the flame light emissions captured by camera in $ROF = 2.2$ and $P_C = 20$ *bar* case. It is advisable to

conduct further methane/oxygen test campaigns in order to verify that for $ROF = 2.2$ and $P_C = 20 \text{ bar}$ case the maximum emission value would be reached. If this behavior would be not confirmed, a more in-depth analysis of this case has to be carried out to better understand this dynamic phenomenon.

Chapter 6

Appendix

6.1 Appendix A

6.1.1 Performance Matlab code

```
1 %%%%%%%%%%% DATA %%%%%%%%%%%
  %%
3 %%%%%%%%%%% 10-22 %%%%%%%%%%%
  Pcc_theo=10;
  %theoretical combustion chamber pressure [bar]
5 ROF=2.2575;
  %nominal mixture ratio [-]
  mdotTot_theo= 0.0309;
  %theoretical total mass flow rate [kg/s]
7 mdotMe= (0.009918336911325 + 0.010033597832988 + 0.010035377626094)/3;
  %experimental methane mass flow rate [kg/s]
  mdotOx= (0.022311793843427+ 0.022645093474795 +0.022655616376730)/3;
  %experimental oxygen mass flow rate [kg/s]
9 mdotTot= (0.033436202098143+ 0.033876030127975+ 0.033889451822665)/3;
  %experimental total mass flow rate [kg/s]
  Pcc= 9.706860149217768;
  %experimental combustion chamber pressure [bar]
11 T_Ox3= (2.829731992179227e+02+ 2.751602430518293e+02)/2;
  %experimental oxygen injection temperature [K]
  T_Me3= (2.741555398095723e+02+ 2.635379915396342e+02)/2;
  %experimental methane injection temperature [K]
13 P_Ox4= (13.833442977003413 +13.781926414969718)/2;
  %experimental oxygen injection pressure [bar]
```

```

P_Me4= (12.249085761856591 +12.323650066561433)/2;
%experimental methane injection pressure [bar]
15 P_amb=0.97;
%experimental environment pressure [atm]
Tcc=2965.08;
%theoretical combustion chamber temperature [K]
17 %%
%10-26 %
19 Pcc_theo=10;
ROF=2.6053;
21 mdotTot_theo= 0.0306;
mdotMe= (0.008452508694651 +0.008539155727106+ 0.008546045907938)/3;
23 mdotOx= (0.021941845848706+ 0.022273561562953+ 0.022264779905566)/3;
mdotTot= (0.031515207018272 +0.031923477252041 +0.031922585025178)/3;
25 Pcc= 9.184189020970276;
T_Ox3= (2.832356967969697e+02 +2.752635917895278e+02)/2;
27 T_Me3= (2.754952613858586e+02+ 2.655636108018480e+02)/2;
P_Ox4= (13.445263595145104+ 13.298106089085529)/2;
29 P_Me4= (11.249894664803147+ 11.307874156439714)/2;
P_amb=0.9700000000000000;
31 Tcc=3182.31;
%%
%10-30 %
33 Pcc_theo=10;
ROF=3.0407;
35 mdotTot_theo= 0.0309;
mdotMe= (0.007688206612076 + 0.007800048462051 + 0.007788332426517)/3;
37 mdotOx= (0.023474482955778+ 0.023709554331788 +0.023681006794964)/3;
mdotTot= (0.032110731273185+ 0.032454610557059 +0.032415169314136)/3;
39 Pcc= 9.337816571552423;
T_Ox3= (2.817397390816327e+02 +2.740823801781377e+02)/2;
41 T_Me3= (2.748642808581633e+02+ 2.664322845060728e+02)/2;
P_Ox4= (13.981382668862862+ 13.857177712422427)/2;
43 P_Me4= (11.151207864529535 +11.098046821396150)/2;
P_amb=0.9700000000000000;
45 Tcc=3305.23;
%%
%10-34 %
49 Pcc_theo=10;

```

```

ROF=3.5493;
51 mdotTot_theo= 0.0315;
   mdotMe= (0.006937807505857+ 0.007065075731118+ 0.007059832046122)/3;
53 mdotOx= (0.024736291943609+ 0.025050855271662+ 0.025056087922223)/3;
   mdotTot= (0.032522449103791+ 0.032963287698881 +0.032961362077281)/3;
55 Pcc= 9.434916252900930;
   T_Ox3= (2.824700479665315e+02+ 2.746746821643002e+02)/2;
57 T_Me3= (2.777902427129818e+02+ 2.688677252322516e+02)/2;
   P_Ox4= (14.438539421531520+ 14.336003463209586)/2;
59 P_Me4= (10.920868235637135 +10.888782131914091)/2;
   P_amb=0.9700000000000000;
61 Tcc=3344.25;
   %%
63 %%%%%%%%%%% 20-22 %%%%%%%%%%%
   Pcc_theo=20;
65 ROF=2.1579;
   mdotTot_theo= 0.0618;
67 mdotMe= (0.019628237532383 +0.019529376420234 +0.019514436343088)/3;
   mdotOx= (0.042334244199237+ 0.042115207891235+ 0.042109501716017)/3;
69 mdotTot= (0.063985116644829 +0.063661573496869 +0.063641488145557)/3;
   Pcc= 18.759117233750370;
71 T_Ox3= (2.895484186238585e+02 +2.754822424870106e+02)/2;
   T_Me3= (2.752460953629341e+02+ 2.574973671774515e+02)/2;
73 P_Ox4= (26.131877734673687+ 25.906710847819298)/2;
   P_Me4= (23.551315140121037 +23.503199545332787)/2;
75 P_amb=0.9600000000000000;
   Tcc=2901.74;
77 %%
   %%%%%%%%%%% 20-26 %%%%%%%%%%%
79 Pcc_theo=20;
   ROF=2.5456;
81 mdotTot_theo= 0.0609;
   mdotMe= (0.017113473728345+ 0.017237802689586+ 0.017242877700121)/3;
83 mdotOx= (0.044057480678237 +0.043781373324095 +0.043875643282098)/3;
   mdotTot= (0.063009023062766 +0.062844534647088 +0.062945354955257)/3;
85 Pcc= 18.624860902751767;
   T_Ox3= (2.894208646355422e+02 +2.753879222801636e+02)/2;
87 T_Me3= (2.788634333524096e+02 +2.614434681114520e+02)/2;
   P_Ox4= (26.313025293567330+ 26.144226241236495)/2;

```

```

89 P_Me4= (22.063260943856267+ 22.441525126119560)/2;
   P_amb=0.9600000000000000;
91 Tcc=3219.12;
   %%
93 %%%%%%%%%%% 20-30 %%%%%%%%%%%
   Pcc_theo=20;
95 ROF=3.0361;
   mdotTot_theo= 0.0614;
97 mdotMe= (0.014745100465281 +0.014959630420899 +0.014951372850301)/3;
   mdotOx= (0.045834543919257 +0.045438199741679 +0.045393033901348)/3;
99 mdotTot= (0.062340524211185 +0.062146946388153+ 0.062092642628709)/3;
   Pcc= 18.333086092406948;
101 T_Ox3= (2.897975729607759e+02+ 2.748961885226319e+02)/2;
   T_Me3= (2.791651095239751e+02+ 2.631994642565518e+02)/2;
103 P_Ox4= (26.914881203141213+ 26.480101257277720)/2;
   P_Me4= (21.195871936909654+ 21.372222499247968)/2;
105 P_amb=0.9700000000000000;
   Tcc=3391.16;
107 %%
   %%%%%%%%%%% 20-34 %%%%%%%%%%%
109 Pcc_theo=20;
   ROF=3.3410;
111 mdotTot_theo= 0.0625;
   mdotMe= (0.014506828885724 +0.014700970960041+ 0.014711343932151)/3;
113 mdotOx= (0.049499404115645+ 0.049119098051995+ 0.049148784281453)/3;
   mdotTot= (0.065558355228645 +0.065361770334694+ 0.065402402839475)/3;
115 Pcc= 19.147933320529360;
   T_Ox3= (2.904725237571462e+02+ 2.726093902500702e+02)/2;
117 T_Me3= (2.821816417059032e+02 +2.633638148693958e+02)/2;
   P_Ox4= (28.224825185989285+ 27.908562873543556)/2;
119 P_Me4= (21.439507009320680+ 21.940430668589240)/2;
   P_amb=0.9700000000000000;
121 Tcc=3433.56;
   %%
123 %%%%%%%%%%% Calculation of the molecular weight of the products %%%%%%%%%%%

125 %%% CH4 + 2O2 = CO2 + 2H2O %%%

```

```

127 M_Me= 0.01604;
    %methane molar mass          [kg/mol]
M_CO2=0.044;
    %carbon dioxide molar mass   [kg/mol]
129 M_H2O=0.018;
    %water molar mass            [kg/mol]
M_Ox= 0.015999;
    %atomic oxygen molar mass    [kg/mol]
131 n_moli_Me=mdotMe/M_Me;
    %methane moles number        [mol]
n_moli_Ox=mdotOx/M_Ox;
    %oxygen moles number         [mol]
133 X_CH4= n_moli_Me/(n_moli_Me+n_moli_Ox);
    %methane molar fraction      [-]
Massa_CO2= n_moli_Me*M_CO2;
    %carbon dioxide molecular mass [kg]
135 Massa_H2O= n_moli_Me*M_H2O/2;
    %water molecular mass        [kg]
X_CO2= Massa_CO2/(Massa_CO2+Massa_H2O);
    %carbon dioxide molar fraction [-]
137 X_H2O= Massa_H2O/(Massa_CO2+Massa_H2O);
    %water molar fraction        [-]
M_Prodotti= X_CO2*M_CO2 + X_H2O*M_H2O;
    %products molar mass         [kg/mol]
139
    %%%%%%%%%%%%%%%%%%%%%%%%%%%%%%%%%%%%%%%%%%%%%%%%%%%%%%%%%%%%%%%%%%%%%%%%% PERFORMANCE %%%%%%%%%%%%%%%%%%%%%%%%%%%%%%%%%%%%%%%%%%%%%%%%%%%%%%%%%%%%%%%%%%%%%%%%%
141
P_amb_theo=1;
    %theoretical environment pressure [atm]
143 A_e= 9.336000000000000e-05;
    %nozzle outlet section area     [m^2]
A_t=0.0000576;
    %nozzle throat section area     [m^2]
145 A_Ox= 1.256637061435917e-05;
    %oxygen injector section area   [m^2]
A_Me= 8.639379797371931e-06;
    %methane injector section area  [m^2]
147 R = 8.314;
    %gas constant                   [J/(mol*K)]

```

```

ROF_theo=[2.2 2.6 3.0 3.4];
%nominal mixture ratio          [-]
149 ROF_10bar=[2.2575,2.6053,3.0407,3.5493];
%test mixture ratio at 10 bar   [-]
ROF_20bar=[2.1579,2.5446,3.0361,3.3410];
%test mixture ratio at 20 bar   [-]
151 rho_Ox= (Pcc*100000*M_Ox*2)/(R*T_Ox3);
%experimental oxygen density     [kg/m^3]
rho_Me= (Pcc*100000*M_Me)/(R*T_Me3);
%experimental methane density    [kg/m^3]
153 u_Ox= mdotOx/(rho_Ox*A_Ox);
%oxygen flow velocity           [m/s]
u_Me= mdotMe/(rho_Me*A_Me);
%methane flow velocity          [m/s]
155 VR= u_Me/u_Ox
%velocity ratio                 [-]
J= (rho_Me*u_Me^2)/(rho_Ox*u_Ox^2)
%momentum flux ratio           [-]
157 rho_b= (rho_Ox*rho_Me*(1+ROF))./(ROF*rho_Me + rho_Ox);
%bulk density                   [kg/m^3]
F_0=100000*Pcc*A_t
%thrust delivered by rocket engine in vacuum [N]
159 gam=1.33;
%ratio of specific heats
u_e=sqrt((2*gam/(gam-1))*(Tcc*R/M_Prodotti)...
%nozzle outlet velocity         [m/s]
161 * (1-(P_amb^((gam-1)/gam))/Pcc^((gam-1)/gam)));
F=mdotTot*u_e;
163 C_F= F/F_0;
%thrust coefficient             [-]
c_star= Pcc*100000*A_t/mdotTot;
%experimental characteristic velocity [m/s]
165 c_star_theo= Pcc_theo*100000*A_t/mdotTot_theo;
%theoretical characteristic velocity [m/s]
c=c_star*C_F;
%effective exhaust velocity     [m/s]
167 g0=9.81;
%gravity acceleration           [m/s^3]

```

```

I_sp=c/g0;
%specific impulse
169 eta_c=c_star/c_star_theo;
%combustion efficiency [-]
I_rho=I_sp*rho_b;
%volumetric specific impulse [kg*s/m^3]
171

173 %%%%%%%%%% RESULTS %%%%%%%%%%
VR_array_10bar= [1.239804074998331 1.079834971333798...
175 0.928180546417791 0.801226359351051];
VR_array_20bar= [1.268324174458063 1.087305928370625...
177 0.910636688726975 0.835565883565994];
J_10bar= [0.799817463410271 0.603357072554773...
179 0.443452398283404 0.327977711683424];
J_20bar= [0.855255659172165 0.619506648349726...
181 0.432806219013902 0.361229793961061 ];

183 c_star_10bar= [1.657428381306666e+03 1.664226865422715e+03...
1.663813362627100e+03 1.656070668460574e+03 ];
185 c_star_20bar= [1.694603130740381e+03 1.704658103462819e+03...
1.697907253864668e+03 1.685370958038277e+03 ];
187 c_star_theo_10bar=[1.864077669902913e+03 1.882352941176471e+03...
1.864077669902913e+03 1.828571428571428e+03];
189 c_star_theo_20bar= [1.864077669902913e+03 1.891625615763546e+03...
1.876221498371335e+03 1.843200000000000e+03];
191

Isp_10bar=[1.506873659931736e+02 1.547032651356525e+02...
193 1.580957705223955e+02 1.592963511201651e+02];
Isp_20bar=[1.631920048085737e+02 1.717444949093211e+02...
195 1.757454279507612e+02 1.777224129662519e+02];

197 c_10bar= Isp_10bar*g0;
c_20bar= Isp_20bar*g0;
199 C_F_10bar= c_10bar./c_star_10bar;
C_F_20bar= c_20bar./c_star_20bar;
201 eta_c_10bar= c_star_10bar./c_star_theo_10bar;
eta_c_20bar= c_star_20bar./c_star_theo_20bar;
203

```

```

bulk_density_10bar=[10.434248450486573 10.056530385743947...
205     10.485241448637744 10.768885906494400];
bulk_density_20bar=[19.981576048380045 20.205937892538316...
207     20.367485248263010 21.545798610545198];

209 I_rho_10bar= bulk_density_10bar.*Isp_10bar;
I_rho_20bar= bulk_density_20bar.*Isp_20bar;

211
    %%%%%%%%% INTERPOLATION OF DATA AND PLOT %%%%%%%%%
213
    p1=polyfit (ROF_10bar,VR_array_10bar,3);
215 p2=polyfit (ROF_20bar,VR_array_20bar,3);
    p3=polyfit (ROF_10bar,J_10bar,3);
217 p4=polyfit (ROF_20bar,J_20bar,3);
    p5=polyfit (ROF_10bar,c_star_10bar,3);
219 p7=polyfit (ROF_theo,c_star_theo_10bar,3);
    p11=polyfit (ROF_10bar,Isp_10bar,3);
221 p12=polyfit (ROF_20bar,Isp_20bar,3);
    p13=polyfit (ROF_10bar,c_10bar,3);
223 p14=polyfit (ROF_20bar,c_20bar,3);
    p15=polyfit (ROF_10bar,C_F_10bar,3);
225 p16=polyfit (ROF_20bar,C_F_20bar,3);
    p17=polyfit (ROF_10bar,I_rho_10bar,3);
227 p18=polyfit (ROF_20bar,I_rho_20bar,3);
    ROF_fit=2.1:0.01:3.6;
229 y1=polyval (p1,ROF_fit);
    y2=polyval (p2,ROF_fit);
231 y3=polyval (p3,ROF_fit);
    y4=polyval (p4,ROF_fit);
233 y5=polyval (p5,ROF_fit);
    y7=polyval (p7,ROF_fit);
235 y6 = interp1 (ROF_20bar,c_star_20bar,ROF_fit,'pchip');
    y8= interp1 (ROF_theo,c_star_theo_20bar,ROF_fit,'pchip');
237 y9= interp1 (ROF_theo,eta_c_10bar,ROF_fit,'pchip');
    y10= interp1 (ROF_theo,eta_c_20bar,ROF_fit,'pchip');
239 y11=polyval (p11,ROF_fit);
    y12=polyval (p12,ROF_fit);
241 y13=polyval (p13,ROF_fit);
    y14=polyval (p14,ROF_fit);

```

```

243 y15=polyval(p15,ROF_fit);
    y16=polyval(p16,ROF_fit);
245 y17=polyval(p17,ROF_fit);
    y18=polyval(p18,ROF_fit);
247
    figure(1)
249 plot(ROF_10bar,VR_array_10bar,'k.','MarkerSize',22)
    hold on
251 plot(ROF_20bar,VR_array_20bar,'r.','MarkerSize',22)
    plot(ROF_fit,y1,'k-.')
253 plot(ROF_fit,y2,'r-.')
    xlabel('O/F')
255 ylabel('Velocity_Ratio')
    grid on
257 lgd = legend('10_bar','20_bar');
    title(lgd,'P_{CC}_Variation')
259
    figure(2)
261 plot(ROF_10bar,J_10bar,'k.','MarkerSize',22)
    hold on
263 plot(ROF_20bar,J_20bar,'r.','MarkerSize',22)
    plot(ROF_fit,y3,'k-.')
265 plot(ROF_fit,y4,'r-.')
    xlabel('O/F')
267 ylabel('Momentum_Flux_Ratio')
    grid on
269 lgd = legend('10_bar','20_bar');
    title(lgd,'P_{CC}_Variation')
271
    figure(3)
273 plot(ROF_10bar,c_star_10bar,'k.','MarkerSize',22)
    hold on
275 plot(ROF_20bar,c_star_20bar,'r.','MarkerSize',22)
    plot(ROF_fit,y5,'k-.')
277 plot(ROF_fit,y6,'r-.')
    xlabel('O/F')
279 ylabel('Experimental_Characteristic_Velocity_[m/s]')
    grid on
281 axis([2.1 3.6 1650 1720])

```

```

lgd = legend('10_bar','20_bar');
283 title(lgd,'P_{CC}_Variation')

285 figure(4)
plot(ROF_theo,c_star_theo_10bar,'k.','MarkerSize',22)
287 hold on
plot(ROF_theo,c_star_theo_20bar,'r.','MarkerSize',22)
289 plot(ROF_fit,y7,'k-.')
plot(ROF_fit,y8,'r-.')
291 xlabel('O/F')
ylabel('Theoretical_Characteristic_Velocity_[m/s]')
293 grid on
axis([2.1 3.6 1820 1900])
295 lgd = legend('10_bar','20_bar');
title(lgd,'P_{CC}_Variation')

297
figure(5)
299 plot(ROF_theo,eta_c_10bar,'k.','MarkerSize',22)
hold on
301 plot(ROF_theo,eta_c_20bar,'r.','MarkerSize',22)
plot(ROF_fit,y9,'k-.')
303 plot(ROF_fit,y10,'r-.')
xlabel('O/F')
305 ylabel('Combustion_Efficiency_\eta_c')
grid on
307 axis([2.1 3.6 0.88 0.925])
lgd = legend('10_bar','20_bar');
309 title(lgd,'P_{CC}_Variation')

311 figure(6)
plot(ROF_10bar,Isp_10bar,'k.','MarkerSize',22)
313 hold on
plot(ROF_20bar,Isp_20bar,'r.','MarkerSize',22)
315 plot(ROF_fit,y11,'k-.')
plot(ROF_fit,y12,'r-.')
317 xlabel('O/F')
ylabel('Specific_Impulse_I_{sp}_[s]')
319 grid on
lgd = legend('~10_bar','~20_bar');

```

```

321 title(lgd,'P_{CC}_Variation')

323
figure(7)
325 plot(ROF_10bar,c_10bar,'k.','MarkerSize',22)
hold on
327 plot(ROF_20bar,c_20bar,'r.','MarkerSize',22)
plot(ROF_fit,y13,'k-.')
329 plot(ROF_fit,y14,'r-.')
xlabel('O/F')
331 ylabel('Effective_Exhaust_Velocity_c_[m/s]')
grid on
333 lgd = legend('~10_bar','~20_bar');
title(lgd,'P_{CC}_Variation')

335
figure(8)
337 plot(ROF_10bar,C_F_10bar,'k.','MarkerSize',22)
hold on
339 plot(ROF_20bar,C_F_20bar,'r.','MarkerSize',22)
plot(ROF_fit,y15,'k-.')
341 plot(ROF_fit,y16,'r-.')
xlabel('O/F')
343 ylabel('Thrust_Coefficient_C_F')
grid on
345 lgd = legend('~10_bar','~20_bar');
title(lgd,'P_{CC}_Variation')

347
figure(9)
349 plot(ROF_10bar,I_rho_10bar,'k.','MarkerSize',22)
hold on
351 plot(ROF_20bar,I_rho_20bar,'r.','MarkerSize',22)
plot(ROF_fit,y17,'k-.')
353 plot(ROF_fit,y18,'r-.')
xlabel('O/F')
355 ylabel('Volumetric_Specific_Impulse_I_{\rho}_[kg*s/m^3]')
grid on
357 lgd = legend('~10_bar','~20_bar');
title(lgd,'P_{CC}_Variation')

359

```

```

figure(10)
361 yyaxis right
    h1=plot(ROF_10bar,I_rho_10bar,'k.','MarkerSize',22);
363 hold on
    h2=plot(ROF_20bar,I_rho_20bar,'r.','MarkerSize',22);
365 plot(ROF_fit,y17,'k-.')
    plot(ROF_fit,y18,'r-.')
367 xlabel('O/F')
    ylabel('Volumetric_Specific_Impulse_I_{\rho}_{\rho}[kg*s/m^3]')
369
    yyaxis left
371 h3=plot(ROF_10bar,c_10bar,'g.','MarkerSize',22);
    hold on
373 h4=plot(ROF_20bar,c_20bar,'b.','MarkerSize',22);
    plot(ROF_fit,y13,'g-.')
375 plot(ROF_fit,y14,'b-.')
    xlabel('O/F')
377 ylabel('Effective_Exhaust_Velocity_c_{c}[m/s]')
    grid on
379 lgd = legend([h1 h2 h3 h4],...
    'I_{\rho}_{\rho}~10_bar','I_{\rho}_{\rho}~20_bar','c_{c}~10_bar','c_{c}~20_bar');
381 title(lgd,'P_{CC}_Variation')

```

6.1.2 Emission Imaging Matlab code

```

1  %%%%%%%%%%%%%%%%%%%%%%%%%%%%%%%%%%%%%%%%% OH Emission %%%%%%%%%%%%%%%%%%%%%%%%%%%%%%%%%%%%%%%%%
   %%
3  %%%%%%%%%%%%%%%%%%%%%%%%%%%%%%%%%%%%%%%%% Directory Flame METHANE %%%%%%%%%%%%%%%%%%%%%%%%%%%%%%%%%%%%%%%%%

5  TXTDir=...

7  %%%%%%%%%%%%%%%%%%%%%%%%%%%%%%%%%%%%%%%%% Directory Calibration METHANE %%%%%%%%%%%%%%%%%%%%%%%%%%%%%%%%%%%%%%%%%

9  %TXTDir=...

11 %%
   %%%%%%%%%%%%%%%%%%%%%%%%%%%%%%%%%%%%%%%%% IMPORT IMAGE (*.txt) AND PROCESS IMAGE %%%%%%%%%%%%%%%%%%%%%%%%%%%%%%%%%%%%%%%%%
13
   FileSystemPath= dir(fullfile(TXTDir,'*.txt'));
15 [tmp ind]=sort({FileSystemPath.date});
   FileSystemPath=FileSystemPath(ind);
17 cd(TXTDir)
   %%
19 %%%%%%%%%%%%%%%%%%%%%%%%%%%%%%%%%%%%%%%%% EVAL.TIME AND AVERAGE IMAGE%%%%%%%%%%%%%%%%%%%%%%%%%%%%%%%%%%%%%%%%
   %%
21 %%%%%%%%% CALIBRATION %%%%%%%%%

23 %NUMBER OF FILE *.TXT IN THE FOLDER
   %NC=10;
25 %FILE *.TXT WHERE THE AVERAGE STARTS
   %MC=5;
27 %%
   %%%%%%%%% METHANE %%%%%%%%%

29
   %NUMBER OF FILE *.TXT IN THE FOLDER
31 NCH4=40; %tcw-10-22-30-10-2
   %NCH4=40; %tcw-10-26-30-10-1
33 %NCH4=70; %tcw-10-30-30-10-6
   %NCH4=70; %tcw-10-34-30-10-8
35 %NCH4=70; %tcw-20-22-30-10-1
   %NCH4=70; %tcw-20-26-30-10-1
37 %NCH4=70; %tcw-20-30-30-10-5

```

```

%NCH4=70; %tcw-20-34-30-10-13
39
%FILE *.TXT WHERE THE AVERAGE STARTS
41 MCH4=20; %tcw-10-22-30-10-2
    %MCH4=22; %tcw-10-26-30-10-1
43 %MCH4=25; %tcw-10-30-30-10-6
    %MCH4=25; %tcw-10-34-30-10-8
45 %MCH4=20; %tcw-20-22-30-10-1
    %MCH4=20; %tcw-20-26-30-10-1
47 %MCH4=20; %tcw-20-30-30-10-5
    %MCH4=20; %tcw-20-34-30-10-13
49
%%
51 %%%%%%%%% METHANE %%%%%%%%%

53 %eval_frac = abs(MC/NC -1)*(length(FileSystemPath)); %FOR CALIBRATION

55 eval_frac = abs(MCH4/NCH4 -1)*(length(FileSystemPath)); %FOR TESTS

57 %%
    eval_time=length(FileSystemPath)-eval_frac;
    %evaluation time
59 eval_time=round(eval_time);

61 %%
    eval_window=2;
    %FOR METHANE IS 2, FOR CALIBRATION IS 4

63
    %%

65
for i=eval_time-eval_window:eval_time+eval_window
67 A(i-(eval_time-eval_window - 1)) = importdata(FileSystemPath(i).name);
    B(:, :, i-(eval_time-eval_window - 1))=A(i-(eval_time-eval_window - 1)).data;
69
end

71 [m,n,t]=size(B);
    sum = 0;
73 % Average calculation explained in chapter 3
for u=1:m

```

```

75   for j=1:n
       for k=1:t
77       sum=sum + B(u, j, k);
       end
79       v(u, j)=sum/t;
       sum =0;
81   end
end
83
85 %%
%%%%%%%%%%%%%%%%%%%%%%%%%%%%%%%%%%%%%%%%%%%%%%%%%%%%%%%%%%%%%%%%%%%%%%%%%%%% CREATE IMAGE %%%%%%%%%%%%%%%%%%%%%%%%%%%%%%%%%%%%%%%%%%%%%%%%%%%%%%%%%%%%%%%%%%%%%%%%%%%
87
figure(1)
89
IMAGE=imagesc(v);
91 %title(sprintf('VIRGIN IMAGE'))
% colorbar;
93 colormap(jet)
% limits=[250 5228];
95 % limits=[250 5723]; %MAXIMUM BRIGHTNESS OF HYDROGEN TCW-20-60...
%limits=[0 4000];
97 %caxis(limits)
saveas(figure(1), 'AverageImageNotRotated.fig')
99 saveas(figure(1), 'AverageImageNotRotated.bmp')
%%
101 %%%%%%%%%%%%%%%%%%%%%%%%%%%%%%%%%%%%%%%%%%%%%%%%%%%%%%%%%%%%%%%%%%%%%%%%%%% CREATE IMAGE ROTATED METHANE %%%%%%%%%%%%%%%%%%%%%%%%%%%%%%%%%%%%%%%%%%%%%%%%%%%%%%%%%%%%%%%%%%%%%%%%%%%
figure(2)
103
v1 = imrotate(v,0); %FOR ALL TESTS
105 imagesc(v1)
colorbar;
107 colormap(jet(256))
%limits=[250 5228]; %LIMIT OF METHANE
109 %limits=[250 5723]; %LIMIT OF HYDROGEN
%caxis(limits)
111 %title(sprintf('ROTATED IMAGE WITH UNIFIED COLOR SCALE'))
saveas(figure(2), 'AverageImageRotated.fig')
113 saveas(figure(2), 'AverageImageRotated.bmp')

```

```

115 %%
117 %%%%%%%%% RESIZING FROM ROTATED IMAGE %%%%%%%%%

119 %v2=v1(104:153,110:263); % tcw-10-22-30-10-2
    %v2=v1(104:153,110:263); % tcw-10-26-30-10-1
121 %v2=v1(110:159,114:267); % tcw-10-30-30-10-6
    %v2=v1(110:159,122:275); % tcw-10-34-30-10-8
123 v2=v1(107:156,136:289); % tcw-20-22-30-10-1
    %v2=v1(106:155,85:238); % tcw-20-26-30-10-1
125 %v2=v1(107:156,136:289); % tcw-20-30-30-10-5
    %v2=v1(104:153,123:276); % tcw-20-34-30-10-13
127
    %v2=v2/5289.4; %for methane
129
figure(3)
131 %v2=v2/5289.4;
    IMAGE=imagesc(v2);
133 colormap(jet(256))
    %limits=[250 5228]; %LIMIT OF METHANE
135 %limits=[250 5723]; %LIMIT OF HYDROGEN
    %limits=[0 1];
137 colorbar;
    %limits=[0 1500];
139 %caxis(limits)

141 xticks([1 77 154])
    xticklabels({'0','20','40'})
143 yticks([1 25 50])
    yticklabels({'12','6','0'})
145 xlabel(' [mm]')
    ylabel(' [mm]')
147 %set(gca,'xDir','reverse');
    %title(sprintf('CUTTED IMAGE WITH UNIFIED COLOR AND NORMALIZED SCALE'))
149 % figure(2)
    % IMAGE=imagesc(v);
151 % colorbar;
    % colormap(jet)

```

```
153 % limits=[250 5228];  
    % % limits=[0 2000];  
155 % caxis(limits)  
  
157 saveas(figure(3),'AverageWindowed.fig')  
    saveas(figure(3),'AverageWindowed.bmp')  
159  
    %%%%%%%%%%%%%%%%%%%%%%%%%%%%%%%%%%%%%%%%%% Brightness %%%%%%%%%%%%%%%%%%%%%%%%%%%%%%%%%%%%%%%%%%  
161 figure(4)  
    plot(mean(v2))  
163 title(sprintf('Brightness'));  
    saveas(figure(4),[TXDir '\Brightness'],'fig')  
165 saveas(figure(4),[TXDir '\Brightness'],'png')
```

6.2 Appendix B

6.2.1 Data Tables

Table 6.1: Hardware Input Data

Symbol	Value	Unit of Measure	Description
A_e	$9.336 \cdot 10^{-5}$	$[m^2]$	Nozzle Outlet Section Area
A_t	$5.760 \cdot 10^{-5}$	$[m^2]$	Nozzle Throat Section Area
A_{GO_2}	$1.256 \cdot 10^{-5}$	$[m^2]$	Oxygen Injector Section Area
A_{GH_4}	$8.639 \cdot 10^{-6}$	$[m^2]$	Methane Injector Section Area

Table 6.2: Thermodynamic and Chemical Input Data

Symbol	Value	Unit of Measure	Description
R	8.314	$[\frac{J}{mol \cdot K}]$	Perfect Gas Constant
γ	1.33	$[-]$	Ratio of Specific Heats
M_{CH_4}	$1.604 \cdot 10^{-2}$	$[\frac{kg}{mol}]$	Methane Molar Mass
M_{O_2}	$3.200 \cdot 10^{-2}$	$[\frac{kg}{mol}]$	Oxygen Molar Mass
M_{CO_2}	$4.400 \cdot 10^{-2}$	$[\frac{kg}{mol}]$	Carbon Dioxide Molar Mass
M_{H_2O}	$1.180 \cdot 10^{-2}$	$[\frac{kg}{mol}]$	Water Molar Mass

Table 6.3: $P_C = 9.707 \text{ bar}$. $ROF = 2.257$

Symbol	Value	Unit of Measure	Description
\dot{m}_{GCH_4}	$1.000 \cdot 10^{-2}$	$\left[\frac{kg}{s}\right]$	Methane Mass Flow Rate
\dot{m}_{GO_2}	$2.250 \cdot 10^{-2}$	$\left[\frac{kg}{s}\right]$	Oxygen Mass Flow Rate
\dot{m}_{TOT}	$3.370 \cdot 10^{-2}$	$\left[\frac{kg}{s}\right]$	Total Mass Flow Rate
P_e	$9.700 \cdot 10^{-1}$	$[atm]$	Ambient Pressure
P_{GCH_4}	$1.228 \cdot 10^1$	$[bar]$	Methane Injection Pressure
P_{GO_2}	$1.380 \cdot 10^1$	$[bar]$	Oxygen Injection Pressure
T_{GCH_4}	$2.688 \cdot 10^2$	$[K]$	Methane Injection Temperature
T_{GO_2}	$2.790 \cdot 10^2$	$[K]$	Oxygen Injection Temperature
T_C	$2.965 \cdot 10^3$	$[K]$	Combustion Chamber Temperature
n_{CH_4}	$6.232 \cdot 10^{-1}$	$[mol]$	Methane Moles Number
n_{O_2}	$1.408 \cdot 10^0$	$[mol]$	Oxygen Moles Number
X_{CH_4}	$3.067 \cdot 10^{-1}$	$[-]$	Methane Molar Fraction
X_{CO_2}	$8.302 \cdot 10^{-1}$	$[-]$	Carbon Dioxide Molar Fraction
X_{H_2O}	$1.698 \cdot 10^{-1}$	$[-]$	Water Molar Fraction
m_{CO_2}	$2.740 \cdot 10^{-2}$	$[kg]$	Carbon Dioxide Molecular Mass
m_{H_2O}	$5.600 \cdot 10^{-3}$	$[kg]$	Water Molecular Mass
M_{PR}	$3.960 \cdot 10^{-2}$	$\left[\frac{kg}{mol}\right]$	Products Molar Mass
ρ_{GCH_4}	$6.966 \cdot 10^0$	$\left[\frac{kg}{m^3}\right]$	Methane Density
ρ_{GO_2}	$1.338 \cdot 10^1$	$\left[\frac{kg}{m^3}\right]$	Oxygen Density
ρ_{BULK}	$1.043 \cdot 10^1$	$\left[\frac{kg}{m^3}\right]$	Bulk Density
u_{GCH_4}	$1.660 \cdot 10^2$	$\left[\frac{m}{s}\right]$	Methane Flow Velocity
u_{GO_2}	$1.339 \cdot 10^2$	$\left[\frac{m}{s}\right]$	Oxygen Flow Velocity
u_e	$1.478 \cdot 10^3$	$\left[\frac{m}{s}\right]$	Nozzle Outlet Velocity
VR	$1.239 \cdot 10^0$	$[-]$	Velocity Ratio
J	$7.998 \cdot 10^{-1}$	$[-]$	Momentum Flux Ratio
F_0	$5.591 \cdot 10^1$	$[N]$	Thrust in Vacuum. No Nozzle Contribution
F	$4.986 \cdot 10^1$	$[N]$	Thrust
C_F	$8.919 \cdot 10^{-1}$	$[-]$	Thrust Coefficient
c^*	$1.657 \cdot 10^3$	$\left[\frac{m}{s}\right]$	Characteristic Velocity
c	$1.478 \cdot 10^3$	$\left[\frac{m}{s}\right]$	Effective Exhaust Velocity
I_{sp}	$1.506 \cdot 10^2$	$[s]$	Specific Impulse
I_ρ	$1.578 \cdot 10^3$	$\left[\frac{kg \cdot s}{m^3}\right]$	Volumetric Specific Impulse
η_c	$8.891 \cdot 10^{-1}$	$[-]$	Combustion Efficiency

Table 6.4: $P_C = 9.184 \text{ bar}$. $ROF = 2.605$

Symbol	Value	Unit of Measure	Description
\dot{m}_{GCH_4}	$8.500 \cdot 10^{-2}$	$[\frac{kg}{s}]$	Methane Mass Flow Rate
\dot{m}_{GO_2}	$2.200 \cdot 10^{-2}$	$[\frac{kg}{s}]$	Oxygen Mass Flow Rate
\dot{m}_{TOT}	$3.180 \cdot 10^{-2}$	$[\frac{kg}{s}]$	Total Mass Flow Rate
P_e	$9.700 \cdot 10^{-1}$	$[atm]$	Ambient Pressure
P_{GCH_4}	$1.127 \cdot 10^1$	$[bar]$	Methane Injection Pressure
P_{GO_2}	$1.337 \cdot 10^1$	$[bar]$	Oxygen Injection Pressure
T_{GCH_4}	$2.705 \cdot 10^2$	$[K]$	Methane Injection Temperature
T_{GO_2}	$2.792 \cdot 10^2$	$[K]$	Oxygen Injection Temperature
T_C	$3.182 \cdot 10^3$	$[K]$	Combustion Chamber Temperature
n_{CH_4}	$5.307 \cdot 10^{-1}$	$[mol]$	Methane Moles Number
n_{O_2}	$1.385 \cdot 10^0$	$[mol]$	Oxygen Moles Number
X_{CH_4}	$2.770 \cdot 10^{-1}$	$[-]$	Methane Molar Fraction
X_{CO_2}	$8.302 \cdot 10^{-1}$	$[-]$	Carbon Dioxide Molar Fraction
X_{H_2O}	$1.698 \cdot 10^{-1}$	$[-]$	Water Molar Fraction
m_{CO_2}	$2.340 \cdot 10^{-2}$	$[kg]$	Carbon Dioxide Molecular Mass
m_{H_2O}	$4.800 \cdot 10^{-3}$	$[kg]$	Water Molecular Mass
M_{PR}	$3.960 \cdot 10^{-2}$	$[\frac{kg}{mol}]$	Products Molar Mass
ρ_{GCH_4}	$6.549 \cdot 10^0$	$[\frac{kg}{m^3}]$	Methane Density
ρ_{GO_2}	$1.265 \cdot 10^1$	$[\frac{kg}{m^3}]$	Oxygen Density
ρ_{BULK}	$1.005 \cdot 10^1$	$[\frac{kg}{m^3}]$	Bulk Density
u_{GCH_4}	$1.504 \cdot 10^2$	$[\frac{m}{s}]$	Methane Flow Velocity
u_{GO_2}	$1.393 \cdot 10^2$	$[\frac{m}{s}]$	Oxygen Flow Velocity
u_e	$1.517 \cdot 10^3$	$[\frac{m}{s}]$	Nozzle Outlet Velocity
VR	$1.079 \cdot 10^0$	$[-]$	Velocity Ratio
J	$6.034 \cdot 10^{-1}$	$[-]$	Momentum Flux Ratio
F_0	$5.290 \cdot 10^1$	$[N]$	Thrust in Vacuum. No Nozzle Contribution
F	$4.824 \cdot 10^1$	$[N]$	Thrust
C_F	$9.119 \cdot 10^{-1}$	$[-]$	Thrust Coefficient
c^*	$1.664 \cdot 10^3$	$[\frac{m}{s}]$	Characteristic Velocity
c	$1.517 \cdot 10^3$	$[\frac{m}{s}]$	Effective Exhaust Velocity
I_{sp}	$1.547 \cdot 10^2$	$[s]$	Specific Impulse
I_ρ	$1.555 \cdot 10^3$	$[\frac{kg \cdot s}{m^3}]$	Volumetric Specific Impulse
η_c	$8.841 \cdot 10^{-1}$	$[-]$	Combustion Efficiency

Table 6.5: $P_C = 9.337 \text{ bar}$. $ROF = 3.040$

Symbol	Value	Unit of Measure	Description
\dot{m}_{GCH_4}	$7.800 \cdot 10^{-3}$	$\left[\frac{kg}{s}\right]$	Methane Mass Flow Rate
\dot{m}_{GO_2}	$2.360 \cdot 10^{-2}$	$\left[\frac{kg}{s}\right]$	Oxygen Mass Flow Rate
\dot{m}_{TOT}	$3.230 \cdot 10^{-2}$	$\left[\frac{kg}{s}\right]$	Total Mass Flow Rate
P_e	$9.700 \cdot 10^{-1}$	$[atm]$	Ambient Pressure
P_{GCH_4}	$1.112 \cdot 10^1$	$[bar]$	Methane Injection Pressure
P_{GO_2}	$1.391 \cdot 10^1$	$[bar]$	Oxygen Injection Pressure
T_{GCH_4}	$2.706 \cdot 10^2$	$[K]$	Methane Injection Temperature
T_{GO_2}	$2.779 \cdot 10^2$	$[K]$	Oxygen Injection Temperature
T_C	$3.305 \cdot 10^3$	$[K]$	Combustion Chamber Temperature
n_{CH_4}	$4.837 \cdot 10^{-1}$	$[mol]$	Methane Moles Number
n_{O_2}	$1.476 \cdot 10^0$	$[mol]$	Oxygen Moles Number
X_{CH_4}	$2.468 \cdot 10^{-1}$	$[-]$	Methane Molar Fraction
X_{CO_2}	$8.302 \cdot 10^{-1}$	$[-]$	Carbon Dioxide Molar Fraction
X_{H_2O}	$1.698 \cdot 10^{-1}$	$[-]$	Water Molar Fraction
m_{CO_2}	$2.130 \cdot 10^{-2}$	$[kg]$	Carbon Dioxide Molecular Mass
m_{H_2O}	$4.400 \cdot 10^{-3}$	$[kg]$	Water Molecular Mass
M_{PR}	$3.960 \cdot 10^{-2}$	$\left[\frac{kg}{mol}\right]$	Products Molar Mass
ρ_{GCH_4}	$6.656 \cdot 10^0$	$\left[\frac{kg}{m^3}\right]$	Methane Density
ρ_{GO_2}	$1.293 \cdot 10^1$	$\left[\frac{kg}{m^3}\right]$	Oxygen Density
ρ_{BULK}	$1.048 \cdot 10^1$	$\left[\frac{kg}{m^3}\right]$	Bulk Density
u_{GCH_4}	$1.349 \cdot 10^2$	$\left[\frac{m}{s}\right]$	Methane Flow Velocity
u_{GO_2}	$1.453 \cdot 10^2$	$\left[\frac{m}{s}\right]$	Oxygen Flow Velocity
u_e	$1.550 \cdot 10^3$	$\left[\frac{m}{s}\right]$	Nozzle Outlet Velocity
VR	$9.282 \cdot 10^{-1}$	$[-]$	Velocity Ratio
J	$4.435 \cdot 10^{-1}$	$[-]$	Momentum Flux Ratio
F_0	$5.378 \cdot 10^1$	$[N]$	Thrust in Vacuum. No Nozzle Contribution
F	$5.013 \cdot 10^1$	$[N]$	Thrust
C_F	$9.321 \cdot 10^{-1}$	$[-]$	Thrust Coefficient
c^*	$1.663 \cdot 10^3$	$\left[\frac{m}{s}\right]$	Characteristic Velocity
c	$1.550 \cdot 10^3$	$\left[\frac{m}{s}\right]$	Effective Exhaust Velocity
I_{sp}	$1.580 \cdot 10^2$	$[s]$	Specific Impulse
I_ρ	$1.657 \cdot 10^3$	$\left[\frac{kg \cdot s}{m^3}\right]$	Volumetric Specific Impulse
η_c	$8.926 \cdot 10^{-1}$	$[-]$	Combustion Efficiency

Table 6.6: $P_C = 9.434 \text{ bar}$. $ROF = 3.549$

Symbol	Value	Unit of Measure	Description
\dot{m}_{GCH_4}	$7.000 \cdot 10^{-3}$	$[\frac{kg}{s}]$	Methane Mass Flow Rate
\dot{m}_{GO_2}	$2.490 \cdot 10^{-2}$	$[\frac{kg}{s}]$	Oxygen Mass Flow Rate
\dot{m}_{TOT}	$3.280 \cdot 10^{-2}$	$[\frac{kg}{s}]$	Total Mass Flow Rate
P_e	$9.700 \cdot 10^{-1}$	$[atm]$	Ambient Pressure
P_{GCH_4}	$1.090 \cdot 10^1$	$[bar]$	Methane Injection Pressure
P_{GO_2}	$1.438 \cdot 10^1$	$[bar]$	Oxygen Injection Pressure
T_{GCH_4}	$2.733 \cdot 10^2$	$[K]$	Methane Injection Temperature
T_{GO_2}	$2.785 \cdot 10^2$	$[K]$	Oxygen Injection Temperature
T_C	$3.344 \cdot 10^3$	$[K]$	Combustion Chamber Temperature
n_{CH_4}	$4.377 \cdot 10^{-1}$	$[mol]$	Methane Moles Number
n_{O_2}	$1.559 \cdot 10^0$	$[mol]$	Oxygen Moles Number
X_{CH_4}	$2.192 \cdot 10^{-1}$	$[-]$	Methane Molar Fraction
X_{CO_2}	$8.302 \cdot 10^{-1}$	$[-]$	Carbon Dioxide Molar Fraction
X_{H_2O}	$1.698 \cdot 10^{-1}$	$[-]$	Water Molar Fraction
m_{CO_2}	$1.930 \cdot 10^{-2}$	$[kg]$	Carbon Dioxide Molecular Mass
m_{H_2O}	$3.900 \cdot 10^{-3}$	$[kg]$	Water Molecular Mass
M_{PR}	$3.960 \cdot 10^{-2}$	$[\frac{kg}{mol}]$	Products Molar Mass
ρ_{GCH_4}	$6.659 \cdot 10^0$	$[\frac{kg}{m^3}]$	Methane Density
ρ_{GO_2}	$1.303 \cdot 10^1$	$[\frac{kg}{m^3}]$	Oxygen Density
ρ_{BULK}	$1.076 \cdot 10^1$	$[\frac{kg}{m^3}]$	Bulk Density
u_{GCH_4}	$1.220 \cdot 10^2$	$[\frac{m}{s}]$	Methane Flow Velocity
u_{GO_2}	$1.523 \cdot 10^2$	$[\frac{m}{s}]$	Oxygen Flow Velocity
u_e	$1.562 \cdot 10^3$	$[\frac{m}{s}]$	Nozzle Outlet Velocity
VR	$8.012 \cdot 10^{-1}$	$[-]$	Velocity Ratio
J	$3.280 \cdot 10^{-1}$	$[-]$	Momentum Flux Ratio
F_0	$5.434 \cdot 10^1$	$[N]$	Thrust in Vacuum. No Nozzle Contribution
F	$5.128 \cdot 10^1$	$[N]$	Thrust
C_F	$9.436 \cdot 10^{-1}$	$[-]$	Thrust Coefficient
c^*	$1.656 \cdot 10^3$	$[\frac{m}{s}]$	Characteristic Velocity
c	$1.562 \cdot 10^3$	$[\frac{m}{s}]$	Effective Exhaust Velocity
I_{sp}	$1.592 \cdot 10^2$	$[s]$	Specific Impulse
I_ρ	$1.715 \cdot 10^3$	$[\frac{kg \cdot s}{m^3}]$	Volumetric Specific Impulse
η_c	$9.057 \cdot 10^{-1}$	$[-]$	Combustion Efficiency

Table 6.7: $P_C = 18.759 \text{ bar}$. $ROF = 2.158$

Symbol	Value	Unit of Measure	Description
\dot{m}_{GCH_4}	$1.960 \cdot 10^{-2}$	$\left[\frac{kg}{s}\right]$	Methane Mass Flow Rate
\dot{m}_{GO_2}	$4.220 \cdot 10^{-2}$	$\left[\frac{kg}{s}\right]$	Oxygen Mass Flow Rate
\dot{m}_{TOT}	$6.380 \cdot 10^{-2}$	$\left[\frac{kg}{s}\right]$	Total Mass Flow Rate
P_e	$9.600 \cdot 10^{-1}$	$[atm]$	Ambient Pressure
P_{GCH_4}	$2.352 \cdot 10^1$	$[bar]$	Methane Injection Pressure
P_{GO_2}	$2.601 \cdot 10^1$	$[bar]$	Oxygen Injection Pressure
T_{GCH_4}	$2.663 \cdot 10^2$	$[K]$	Methane Injection Temperature
T_{GO_2}	$2.825 \cdot 10^2$	$[K]$	Oxygen Injection Temperature
T_C	$2.901 \cdot 10^3$	$[K]$	Combustion Chamber Temperature
n_{CH_4}	$1.219 \cdot 10^0$	$[mol]$	Methane Moles Number
n_{O_2}	$2.636 \cdot 10^0$	$[mol]$	Oxygen Moles Number
X_{CH_4}	$3.162 \cdot 10^{-1}$	$[-]$	Methane Molar Fraction
X_{CO_2}	$8.302 \cdot 10^{-1}$	$[-]$	Carbon Dioxide Molar Fraction
X_{H_2O}	$1.698 \cdot 10^{-1}$	$[-]$	Water Molar Fraction
m_{CO_2}	$5.360 \cdot 10^{-2}$	$[kg]$	Carbon Dioxide Molecular Mass
m_{H_2O}	$1.100 \cdot 10^{-2}$	$[kg]$	Water Molecular Mass
M_{PR}	$3.960 \cdot 10^{-2}$	$\left[\frac{kg}{mol}\right]$	Products Molar Mass
ρ_{GCH_4}	$1.358 \cdot 10^1$	$\left[\frac{kg}{m^3}\right]$	Methane Density
ρ_{GO_2}	$2.555 \cdot 10^1$	$\left[\frac{kg}{m^3}\right]$	Oxygen Density
ρ_{BULK}	$1.998 \cdot 10^1$	$\left[\frac{kg}{m^3}\right]$	Bulk Density
u_{GCH_4}	$1.666 \cdot 10^2$	$\left[\frac{m}{s}\right]$	Methane Flow Velocity
u_{GO_2}	$1.313 \cdot 10^2$	$\left[\frac{m}{s}\right]$	Oxygen Flow Velocity
u_e	$1.600 \cdot 10^3$	$\left[\frac{m}{s}\right]$	Nozzle Outlet Velocity
VR	$1.268 \cdot 10^0$	$[-]$	Velocity Ratio
J	$8.553 \cdot 10^{-1}$	$[-]$	Momentum Flux Ratio
F_0	$1.080 \cdot 10^2$	$[N]$	Thrust in Vacuum. No Nozzle Contribution
F	$1.020 \cdot 10^2$	$[N]$	Thrust
C_F	$9.447 \cdot 10^{-1}$	$[-]$	Thrust Coefficient
c^*	$1.694 \cdot 10^3$	$\left[\frac{m}{s}\right]$	Characteristic Velocity
c	$1.600 \cdot 10^3$	$\left[\frac{m}{s}\right]$	Effective Exhaust Velocity
I_{sp}	$1.631 \cdot 10^2$	$[s]$	Specific Impulse
I_ρ	$3.260 \cdot 10^3$	$\left[\frac{kg \cdot s}{m^3}\right]$	Volumetric Specific Impulse
η_c	$9.091 \cdot 10^{-1}$	$[-]$	Combustion Efficiency

Table 6.8: $P_C = 18.624 \text{ bar}$. $ROF = 2.545$

Symbol	Value	Unit of Measure	Description
\dot{m}_{GCH_4}	$1.720 \cdot 10^{-2}$	$\left[\frac{kg}{s}\right]$	Methane Mass Flow Rate
\dot{m}_{GO_2}	$4.390 \cdot 10^{-2}$	$\left[\frac{kg}{s}\right]$	Oxygen Mass Flow Rate
\dot{m}_{TOT}	$6.290 \cdot 10^{-2}$	$\left[\frac{kg}{s}\right]$	Total Mass Flow Rate
P_e	$9.600 \cdot 10^{-1}$	$[atm]$	Ambient Pressure
P_{GCH_4}	$2.225 \cdot 10^1$	$[bar]$	Methane Injection Pressure
P_{GO_2}	$2.622 \cdot 10^1$	$[bar]$	Oxygen Injection Pressure
T_{GCH_4}	$2.701 \cdot 10^2$	$[K]$	Methane Injection Temperature
T_{GO_2}	$2.824 \cdot 10^2$	$[K]$	Oxygen Injection Temperature
T_C	$3.219 \cdot 10^3$	$[K]$	Combustion Chamber Temperature
n_{CH_4}	$1.072 \cdot 10^0$	$[mol]$	Methane Moles Number
n_{O_2}	$2.744 \cdot 10^0$	$[mol]$	Oxygen Moles Number
X_{CH_4}	$2.809 \cdot 10^{-1}$	$[-]$	Methane Molar Fraction
X_{CO_2}	$8.302 \cdot 10^{-1}$	$[-]$	Carbon Dioxide Molar Fraction
X_{H_2O}	$1.698 \cdot 10^{-1}$	$[-]$	Water Molar Fraction
m_{CO_2}	$4.720 \cdot 10^{-2}$	$[kg]$	Carbon Dioxide Molecular Mass
m_{H_2O}	$9.600 \cdot 10^{-3}$	$[kg]$	Water Molecular Mass
M_{PR}	$3.960 \cdot 10^{-2}$	$\left[\frac{kg}{mol}\right]$	Products Molar Mass
ρ_{GCH_4}	$1.330 \cdot 10^1$	$\left[\frac{kg}{m^3}\right]$	Methane Density
ρ_{GO_2}	$2.538 \cdot 10^1$	$\left[\frac{kg}{m^3}\right]$	Oxygen Density
ρ_{BULK}	$2.020 \cdot 10^1$	$\left[\frac{kg}{m^3}\right]$	Bulk Density
u_{GCH_4}	$1.496 \cdot 10^2$	$\left[\frac{m}{s}\right]$	Methane Flow Velocity
u_{GO_2}	$1.376 \cdot 10^2$	$\left[\frac{m}{s}\right]$	Oxygen Flow Velocity
u_e	$1.684 \cdot 10^3$	$\left[\frac{m}{s}\right]$	Nozzle Outlet Velocity
VR	$1.087 \cdot 10^{0-1}$	$[-]$	Velocity Ratio
J	$6.195 \cdot 10^{-1}$	$[-]$	Momentum Flux Ratio
F_0	$1.072 \cdot 10^2$	$[N]$	Thrust in Vacuum. No Nozzle Contribution
F	$1.060 \cdot 10^2$	$[N]$	Thrust
C_F	$9.8841 \cdot 10^{-1}$	$[-]$	Thrust Coefficient
c^*	$1.704 \cdot 10^3$	$\left[\frac{m}{s}\right]$	Characteristic Velocity
c	$1.684 \cdot 10^3$	$\left[\frac{m}{s}\right]$	Effective Exhaust Velocity
I_{sp}	$1.717 \cdot 10^2$	$[s]$	Specific Impulse
I_ρ	$3.470 \cdot 10^3$	$\left[\frac{kg \cdot s}{m^3}\right]$	Volumetric Specific Impulse
η_c	$9.012 \cdot 10^{-1}$	$[-]$	Combustion Efficiency

Table 6.9: $P_C = 18.333 \text{ bar}$. $ROF = 3.036$

Symbol	Value	Unit of Measure	Description
\dot{m}_{GCH_4}	$1.490 \cdot 10^{-2}$	$\left[\frac{kg}{s}\right]$	Methane Mass Flow Rate
\dot{m}_{GO_2}	$4.560 \cdot 10^{-2}$	$\left[\frac{kg}{s}\right]$	Oxygen Mass Flow Rate
\dot{m}_{TOT}	$6.220 \cdot 10^{-2}$	$\left[\frac{kg}{s}\right]$	Total Mass Flow Rate
P_e	$9.700 \cdot 10^{-1}$	$[atm]$	Ambient Pressure
P_{GCH_4}	$2.128 \cdot 10^1$	$[bar]$	Methane Injection Pressure
P_{GO_2}	$2.669 \cdot 10^1$	$[bar]$	Oxygen Injection Pressure
T_{GCH_4}	$2.711 \cdot 10^2$	$[K]$	Methane Injection Temperature
T_{GO_2}	$2.823 \cdot 10^2$	$[K]$	Oxygen Injection Temperature
T_C	$3.391 \cdot 10^3$	$[K]$	Combustion Chamber Temperature
n_{CH_4}	$9.280 \cdot 10^{-1}$	$[mol]$	Methane Moles Number
n_{O_2}	$2.847 \cdot 10^0$	$[mol]$	Oxygen Moles Number
X_{CH_4}	$2.458 \cdot 10^{-1}$	$[-]$	Methane Molar Fraction
X_{CO_2}	$8.302 \cdot 10^{-1}$	$[-]$	Carbon Dioxide Molar Fraction
X_{H_2O}	$1.698 \cdot 10^{-1}$	$[-]$	Water Molar Fraction
m_{CO_2}	$4.080 \cdot 10^{-2}$	$[kg]$	Carbon Dioxide Molecular Mass
m_{H_2O}	$8.400 \cdot 10^{-3}$	$[kg]$	Water Molecular Mass
M_{PR}	$3.960 \cdot 10^{-2}$	$\left[\frac{kg}{mol}\right]$	Products Molar Mass
ρ_{GCH_4}	$1.304 \cdot 10^1$	$\left[\frac{kg}{m^3}\right]$	Methane Density
ρ_{GO_2}	$2.499 \cdot 10^1$	$\left[\frac{kg}{m^3}\right]$	Oxygen Density
ρ_{BULK}	$2.036 \cdot 10^1$	$\left[\frac{kg}{m^3}\right]$	Bulk Density
u_{GCH_4}	$1.321 \cdot 10^2$	$\left[\frac{m}{s}\right]$	Methane Flow Velocity
u_{GO_2}	$1.450 \cdot 10^2$	$\left[\frac{m}{s}\right]$	Oxygen Flow Velocity
u_e	$1.724 \cdot 10^3$	$\left[\frac{m}{s}\right]$	Nozzle Outlet Velocity
VR	$9.106 \cdot 10^{-1}$	$[-]$	Velocity Ratio
J	$4.328 \cdot 10^{-1}$	$[-]$	Momentum Flux Ratio
F_0	$1.055 \cdot 10^2$	$[N]$	Thrust in Vacuum. No Nozzle Contribution
F	$1.072 \cdot 10^2$	$[N]$	Thrust
C_F	$1.015 \cdot 10^0$	$[-]$	Thrust Coefficient
c^*	$1.697 \cdot 10^3$	$\left[\frac{m}{s}\right]$	Characteristic Velocity
c	$1.724 \cdot 10^3$	$\left[\frac{m}{s}\right]$	Effective Exhaust Velocity
I_{sp}	$1.757 \cdot 10^2$	$[s]$	Specific Impulse
I_ρ	$3.579 \cdot 10^3$	$\left[\frac{kg \cdot s}{m^3}\right]$	Volumetric Specific Impulse
η_c	$9.050 \cdot 10^{-1}$	$[-]$	Combustion Efficiency

Table 6.10: $P_C = 19.147 \text{ bar}$. $ROF = 3.341$

Symbol	Value	Unit of Measure	Description
\dot{m}_{GCH_4}	$1.460 \cdot 10^{-2}$	$[\frac{kg}{s}]$	Methane Mass Flow Rate
\dot{m}_{GO_2}	$4.930 \cdot 10^{-2}$	$[\frac{kg}{s}]$	Oxygen Mass Flow Rate
\dot{m}_{TOT}	$6.540 \cdot 10^{-2}$	$[\frac{kg}{s}]$	Total Mass Flow Rate
P_e	$9.700 \cdot 10^{-1}$	$[atm]$	Ambient Pressure
P_{GCH_4}	$2.169 \cdot 10^1$	$[bar]$	Methane Injection Pressure
P_{GO_2}	$2.806 \cdot 10^1$	$[bar]$	Oxygen Injection Pressure
T_{GCH_4}	$2.727 \cdot 10^2$	$[K]$	Methane Injection Temperature
T_{GO_2}	$2.815 \cdot 10^2$	$[K]$	Oxygen Injection Temperature
T_C	$3.433 \cdot 10^3$	$[K]$	Combustion Chamber Temperature
n_{CH_4}	$9.127 \cdot 10^{-1}$	$[mol]$	Methane Moles Number
n_{O_2}	$3.078 \cdot 10^0$	$[mol]$	Oxygen Moles Number
X_{CH_4}	$2.287 \cdot 10^{-1}$	$[-]$	Methane Molar Fraction
X_{CO_2}	$8.302 \cdot 10^{-1}$	$[-]$	Carbon Dioxide Molar Fraction
X_{H_2O}	$1.698 \cdot 10^{-1}$	$[-]$	Water Molar Fraction
m_{CO_2}	$4.020 \cdot 10^{-2}$	$[kg]$	Carbon Dioxide Molecular Mass
m_{H_2O}	$8.200 \cdot 10^{-3}$	$[kg]$	Water Molecular Mass
M_{PR}	$3.960 \cdot 10^{-2}$	$[\frac{kg}{mol}]$	Products Molar Mass
ρ_{GCH_4}	$1.354 \cdot 10^1$	$[\frac{kg}{m^3}]$	Methane Density
ρ_{GO_2}	$2.617 \cdot 10^1$	$[\frac{kg}{m^3}]$	Oxygen Density
ρ_{BULK}	$2.154 \cdot 10^1$	$[\frac{kg}{m^3}]$	Bulk Density
u_{GCH_4}	$1.251 \cdot 10^2$	$[\frac{m}{s}]$	Methane Flow Velocity
u_{GO_2}	$1.497 \cdot 10^2$	$[\frac{m}{s}]$	Oxygen Flow Velocity
u_e	$1.743 \cdot 10^3$	$[\frac{m}{s}]$	Nozzle Outlet Velocity
VR	$8.356 \cdot 10^{-1}$	$[-]$	Velocity Ratio
J	$3.612 \cdot 10^{-1}$	$[-]$	Momentum Flux Ratio
F_0	$1.102 \cdot 10^2$	$[N]$	Thrust in Vacuum. No Nozzle Contribution
F	$1.140 \cdot 10^2$	$[N]$	Thrust
C_F	$1.034 \cdot 10^0$	$[-]$	Thrust Coefficient
c^*	$1.685 \cdot 10^3$	$[\frac{m}{s}]$	Characteristic Velocity
c	$1.743 \cdot 10^3$	$[\frac{m}{s}]$	Effective Exhaust Velocity
I_{sp}	$1.777 \cdot 10^2$	$[s]$	Specific Impulse
I_ρ	$3.829 \cdot 10^3$	$[\frac{kg \cdot s}{m^3}]$	Volumetric Specific Impulse
η_c	$9.144 \cdot 10^{-1}$	$[-]$	Combustion Efficiency

Bibliography

- [1] www.nasa.gov.
- [2] D Haeseler, V Bombelli, P Vuillermoz, R Lo, T Marée, and F Caramelli. Green propellant propulsion concepts for space transportation and technology development needs. In *ESA Special Publication*, volume 557, 2004.
- [3] TSI Incorporated. *Advanced combustion diagnostics*. 2013.
- [4] www.andor.com.
- [5] www.artium.com.
- [6] Luiz Gilberto Barreta, Claudio Jose da Rocha, Dermeval Carinhana Jr, Maria Esther, Antonio Carlos de Oliveira Sbampato, and Alberto Monteiro dos Santos. Emission spectroscopy of ch radical to determine the temperature of ethanol flame. *CEP*, 12228:840, 2003.
- [7] Martin Rolf Werner Lauer. *Determination of the heat release distribution in turbulent flames by chemiluminescence imaging*. PhD thesis, Technische Universität München, 2011.
- [8] Jozef Jarosinski and Bernard Veyssiere. *Combustion phenomena: Selected mechanisms of flame formation, propagation and extinction*. CRC press, 2009.
- [9] Dario Alviso, Miguel Mendieta, Jorge Molina, and Juan Carlos Rolón. Flame imaging reconstruction method using high resolution spectral data of oh*, ch* and c2* radicals. *International Journal of Thermal Sciences*, 121:228–236, 2017.
- [10] Jun Kojima, Yuji Ikeda, and Tsuyoshi Nakajima. Basic aspects of oh (a), ch (a), and c2 (d) chemiluminescence in the reaction zone of laminar methane–air premixed flames. *Combustion and Flame*, 140(1-2):34–45, 2005.

- [11] Teodoro Trindade, Artur Ferreira, and Edgar Fernandes. Characterization of combustion chemiluminescence: An image processing approach. *Procedia Technology*, 17:194–201, 2014.
- [12] Andreas Brockhinke, Julia Krüger, Melanie Heusing, and Michael Letzgus. Measurement and simulation of rotationally-resolved chemiluminescence spectra in flames. *Applied Physics B*, 107(3):539–549, 2012.
- [13] Thomas Fiala. *Radiation from high pressure hydrogen-oxygen flames and its use in assessing rocket combustion instability*. Verlag Dr. Hut, 2015.
- [14] Fernanda F Winter, Simona Silvestri, MC Celano, Gregor Schlieben, and O Haidn. High-speed and emission imaging of a coaxial single element gox/gch4 rocket combustion chamber. In *European Conference for Aeronautics and Space Sciences*, 2017.
- [15] Helios Quarz. www.heliosquartz.com.
- [16] S Silvestri, MP Celano, G Schlieben, C Kirchberger, and OJ Haidn. Characterization of a gox-gch4 single element combustion chamber. In *4th Space Propulsion Conference, Köln (Germany)*, 2014.
- [17] LaVision. *FlameStar 2 (F) Operation Manual*, 1998.
- [18] Milan Sonka, Vaclav Hlavac, and Roger Boyle. Image pre-processing. In *Image Processing, Analysis and Machine Vision*, pages 56–111. Springer, 1993.
- [19] O.Biblarz G.P.Sutton. *Rocket Propulsion Elements*. JOHN WILEY and SONS, INC, 2001.
- [20] Mark Sliphorst. *High frequency combustion instabilities of LOx/CH₄ spray flames in rocket engine combustion chambers*. PhD thesis, TU Delft, Delft University of Technology, 2011.
- [21] Johannes Lux and Oskar Haidn. Flame stabilization in high-pressure liquid oxygen/methane rocket engine combustion. *Journal of Propulsion and Power*, 25(1):15–23, 2009.
- [22] Nikolaos Perakis, Maria Palma Celano, and Oskar J Haidn. Heat flux and temperature evaluation in a rectangular multi-element gox/gch4 combustion chamber using an inverse heat conduction method. In *7th European Conference for Aerospace Sciences*, 2017.

- [23] Antonio D'Amato. Development of an Abel transform algorithm for combustion characterization and data analysis, 2017-2018.